UNIVERSITY OF BERGEN

Department of Physics and Technology

MASTER'S THESIS IN OCEAN TECHNOLOGY

Experimental investigation of multirotor wind turbine wakes

Morten Skoland

June 2022

Abstract

With the increasing need for more renewable energy, offshore wind energy has been identified as a critical contributor to help with this increasing demand. However, conventional single rotor wind turbines face challenges in tackling the increased power generation required by each unit, with high costs for installation and maintenance of floating offshore installations. As a result, multirotor wind turbine concepts have emerged as a promising alternative to single rotor wind turbines. This thesis investigates the wake development for several different multirotor setups to contribute to the understanding and viability of multirotors. The effect of inter-rotor spacing, the number of rotors, yawing, additional support structure, and different inflow conditions on the wake development is explored. The wake developments are investigated utilizing porous discs in a towing tank. The wake velocity components have been measured with an Acoustic Doppler Velocimeter.

It was found that a multirotor wake has lower initial velocity deficits in the near wake and a lower turbulence level than a single rotor. Further downstream, however, the wake of multirotors recovers slower than the single rotor, which has lower velocity deficits in the far wake. An increase in the disc spacing in the multirotor system is found to decrease the initial velocity deficit and turbulence produced in the wake. However, compared to the setup's increased total diameter, a larger disc spacing showed a faster wake recovery in the far wake. Furthermore, it was found that an increase in the number of discs results in a lower velocity deficit and turbulence level in the near wake. However, it led to a higher velocity deficit in the far wake. These measurements showed the wake-generated turbulence's importance on the downstream wake recovery. Exposing a multirotor setup to turbulent inflow, different yaw configurations, and an additional support structure showed no disadvantages regarding the wake development for the multirotor.

In conclusion, the wake of multirotors is shown to be strongly dependent on a number of design parameters. The study highlighted the complex interplay of flow entrainment and turbulence production at different locations in the wake and its effects on wake recovery in different downstream regions of the wake. Previous work on power production shows positive signs for different aspects of multirotor setups. Further work should therefore optimize multirotor system designs for the wake development and power production together and in a wind farm context.

Acknowledgment

Many people have been involved for this master thesis' to reach its final form and thereby conclude my years at the University of Bergen.

Firstly, I will like to address my greatest gratitude to my supervisor Jan Bartl at the Western University of Applied Sciences (HVL), for a fantastic job supervising me during the last year. He provided everything a master's student could ask for. He always took the time to discuss results and relevant topics, share his experience, and help out in MarinLab. With his enthusiasm and great personality, it was always a joy. I would also like to thank my supervisor from UiB, Arne S. Kristoffersen, for proofreading and feedback on the thesis appearance and making sure all formal requirements were fulfilled. A thanks also goes out to all the lab engineers at HVL, especially to MarinLab engineer Robert Larsson for support and guidance during the creation of the experimental setups.

Finally, I would like to thank master students Mikkel and Sindre for their great help and company at MarinLab. A special thanks go to master student Idunn Koi, my fellow multirotor soldier, for great discussions, company, and collaboration during the measurement campaign. I would like to thank Aurora and Juni for the many hours spent together working on our theses, exchanging experiences, and helping each other. Lastly, I would like to express big gratitude to all my fellow students during my time at Ocean Technology. Thanks to all the fantastic people I have gotten to know, making the years in Bergen perfect.

Contents

List of Figures

List of Tables

xiv

List of abbreviations

ABL Atmospheric boundary layer

ADCP Acoustic Doppler current profiler

ADV Acoustic Doppler Velocimeter

GHG Greenhouse gas(es)

LES Large eddy simulation

MR Multirotor

MRS Multirotor system

RANS Reynolds-averaged Navier-Stokes

SR Single rotor

TI Turbulence intensity

tke Turbulence Kinetic Energy

Chapter 1

Introduction

The world faces the pressing challenge of limiting global warming to 1.5 - 2 °C above pre-industrial levels by 2050, a goal set by the Paris Agreement in 2015 [1]. The global temperature is already at 1.1 °C above the pre-industrial levels [1], and it has never been more urgent to lower emissions of greenhouse gases (GHG). The energy sector is responsible for 73.2 % of GHG emissions, and electricity and heat generation and the transportation sector are major contributors [2]. These emissions are caused by the use of fossil energy sources. These sectors have opportunities of replacing fossil energy sources with renewable energy sources. In 2019, 84.3 % of global energy came from fossil fuels, and 11.4 % from renewable energy sources [3]. Of the renewable energy sources, solar and wind were responsible for 1.1 % and 2.2 %, respectively [3].

While renewable energy sources should replace fossil energy sources, global energy consumption is increasing. EIA estimated the world's energy consumption to increase by 50 % from 2018 to 2050 due to an increase in global population and standard of living in the coming decades [4]. To reduce GHG emissions, limit global warming, and produce enough energy, increasing the energy production from renewable energy sources like wind, hydro and solar will be crucial. Solar and wind energy have gained attention recently as the energy sources with the best outlook for future electricity generation due to their growth potential compared to other sources like hydropower, and as they are both already established technologies where the levelized cost of energy has reduced in the past years.

Humans have utilized the kinetic energy of the wind for centuries, from the movement of ships to creating a rotating axis for the grinding of corn. Today, electricity is created with wind

turbines through the kinetic energy in the winds. Development of wind turbine projects is increasing rapidly, and from 2010 to 2020, increased the installed global capacity of wind turbines by 283 % from 191 GW to 733 GW [5]. Wind turbines will play an important role in the transition to renewable energy; however, there are obstacles facing the wind energy industry. Wind turbine farms take up large areas, and with protests from local stakeholders, the available development areas onshore are limited. Wind turbine farms also compete with the increasing global population as more houses need to be built and more food produced, and therefor compete for the available land. To tackle these obstacles, the world looks towards our vast oceans for offshore wind. Offshore wind can be split into two categories; bottom fixed and floating. Bottom fixed has been used for decades, while floating wind is an emerging technology. The advantages bottom fixed has over floating wind are cost and technology gap, while its disadvantage is limited suitable areas with water depths suitable for bottom fixed and stakeholder conflicts.

Despite these challenges, companies are now competing for new licensed areas for floating wind, wanting to prove their new technology concepts. The main stakeholders for offshore wind are oil and gas fields, fisheries, wildlife, and shipping. The advantages of floating wind are the flexible placement opportunities to avoid conflict of interest. However, offshore wind turbines were responsible for just 4.6 %, or 34 GW, of the global installed capacity of wind energy in 2020 [5]. The higher cost for offshore wind turbines than onshore wind has been a critical reason for the low offshore wind development. Nevertheless, as the technology gap is decreasing and governments push for offshore wind, will offshore wind most likely be a possible option, and the interest is increasing rapidly. Advantages of offshore wind turbines are stronger and more consistent winds, minor protests from the public, and possible installation near big cities. Furthermore, as many big cities and populated areas are located close to the shore, power transportation can be more efficient, and offshore wind will not use the available land area where the city could expand. All of this leads to the estimate that the installed offshore wind capacity will increase to approximately 1,000 GW in 2050 with 5 % to 15 % covered by floating wind [6].

1.1 Single rotor wind turbines

A wind turbine's power capacity mainly depends on the rotor diameter or the rotor's swept area. With time this has led to an increase in turbine size to maximize the energy production from each turbine, and today the rotor diameter for wind turbines is up to around 200 meters. However, the large swept area leads to high manufacturing and installation costs and complicated shipment and maintenance of such large turbines. Furthermore, politicians and the industry are pushing to take wind turbines from onshore to offshore, excelling the need to tackle these challenges. These challenges are even more significant for offshore floating wind turbines, as the vast structure will be placed on a floating foundation while handling waves, currents, and wind forces. The high mass of the turbine will cause several cost increases down the assembly chain, and the rotor's mass is the main reason. The mass of a turbine blade is shown by Jamieson et al. [7] to increase exponentially with the length of the rotor blade. The swept area increase with the rotor diameter square and the rotor mass increase cubically with the diameter [7], illustrated in Figure 1.1 with a cube representing one rotor.
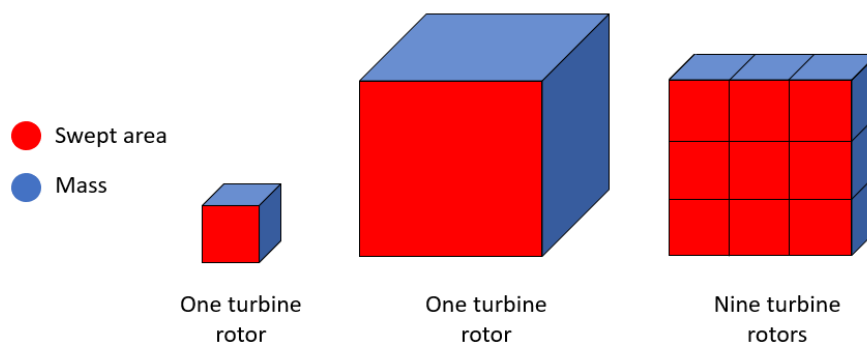
Figure 1.1: *With turbine rotors illustrated with cubes the mass of one turbine rotor scales cubically when increasing the swept area. Adding several turbine rotors achieving the same swept area show 1/3 of the mass. Adapted from [7].*

1.2 Multirotor wind turbines

Today, research on multirotor wind turbine systems mainly consists of computational simulations and one full-scale model of a four-rotor multirotor. Published research indicates that a multirotor wind turbine, compared to a single rotor turbine, would have less weight, less total aggregated aerodynamic loads, cost reductions, a faster recovering wake [7, 8, 9] and higher annual power production due to rotor interaction, called the multirotor effect [10].

Henceforth, a single rotor will be referred to as SR and a multirotor as MR. MR wind turbines enable to increase the rated power of a turbine system without increasing the rotor diameter [7, 10] hence reducing the weight per installed capacity. Smaller rotor blades also enable mass production of rotor blades and parts, driving the production cost down, as well as easier maintenance, installation, and transportation, compared to an equivalent SR [8]. Jameson and Branney [8] presented a relationship for the cost of an MR related to an equivalent rated SR as $\frac{1}{\sqrt{n}}$, where n is the number of rotors in the MR system. The weight advantage for an MR is clearly illustrated in Figure 1.1 with an SR wind turbine mass represented as the full cube. With nine smaller cubes representing each rotor in an MR system, the same swept area is achieved with 1/3 of the weight. Another advantage of MR systems is a possible higher operational time. For example, if one of four rotors with a combined rated capacity of 20 MW fails, it would only reduce the capacity to $\approx \frac{3}{4}$ of the rated capacity. If an SR with the same rated capacity fails, no energy will be produced.

Despite these potential advantages, MR wind turbines have not been vastly explored, even though the idea was first presented for electricity production in 1932 [11]. There are also some disadvantages regarding MR systems; more complex tower structure and higher number of components [11] and little knowledge regarding MR turbine wakes, blockage effects, and MR turbines operating in wind farm situations. In addition, the wakes of wind turbines in general and their interaction are a complex subject, and in recent years the wind turbine industry discovered upstream blockage effects in wind turbine parks, which resulted in lower efficiency than estimated [12]. This shed light on the importance of understanding how close-standing turbines affect each other and how the upstream blockages and wakes appear and interact.

Investigations of MR wakes have yet to receive more attention, and the research is still at an early stage. In 2016, the MR wind turbine demonstrator 4R-V29 was built by Vestas Wind Energy Systems at DTUs Risø campus [10, 11], seen in Figure 1.2. Although it was decommissioned after three years, wake measurements and performance data were collected, providing the possibility to compare computational simulations of its wake with on-site measurements [11]. Van der Laan et al. [11] performed field measurements and numerical simulations of the 4R-V29 and compared the data with an equivalent SR. The measurements and computational results on the 4R-V29 showed increased energy production of up to 1.8 % and 2 %, respectively. Wake recovery was also compared between the SR and MR with RANS simulations showing a shorter wake recovery distance for the MR and lower added wake

turbulence in the far wake. The faster recovery and lower added turbulence by MR turbines could allow closer spaced wind turbines in an MR wind farm.

Figure 1.2: *The Vestas 4R-V29 multirotor wind turbine. From [11].*

Ghaisas et al. [13] performed large-eddy simulations (LES) of MR turbines with four rotors, comparing the wake of the MR with $1d$ inter-rotor spacing, where d is the diameter of one rotor, with an equivalent SR turbine. Their LES showed multirotor wakes recovering faster than single rotor turbines and with less added turbulence, which was confirmed by van der Laan et al. [11] with the MR demonstrator. The effect of inter-rotor spacing was also investigated. Their results showed no significant changes or differences when changing the rotor spacing. However, these results where investigated with unrealistically large rotor spacings [9, 10].

Bastankhah and Abkar [9] further investigated wakes behind different MR turbines with LES. They also concluded that the wake recovered faster behind an MR wind turbine than an SR turbine. Furthermore, Bastankhah and Abkar [9] investigated the effect of rotor spacing, the number of rotors, rotor size, and rotation, showcasing how these parameters affect the MR wake. The turbine-induced forces were generated using the rotating actuator-disc model.

Nishino and Willden [14] explored the efficiency of an array of tidal turbines in a wide channel, deriving mathematical models for blockage, thrust- and power coefficients for these turbines, which depended on the intra-spacing between the turbines and the channel width.

A relationship for the maximum power coefficient for an array of turbines blocking a small part of an infinite wide channel indicated a new theoretical maximum efficiency limiting value at 0.798. This maximum efficiency is higher than the maximum theoretical efficiency for a single turbine, the Betz limit. Their theoretical findings could indicate that turbines or rotors operating near each other can exceed the Betz limit, or at least a higher efficiency than stand-alone SR wind turbines could, due to blockage effects. If these theoretical findings apply to the physical world is uncertain; however, this could be beneficial for MR system (MRS) concepts.

The latest new development regarding MR wind turbine systems is Wind Catching Systems' floating Wind Catcher with over 100 rotors placed in a 300-meter-high rectangular frame [15], seen in Figure 1.3. The technology is still conceptual, but it shows one possibility with MRS. Wind Catching Systems plans to build a first onshore demo with seven rotors before moving forward with an offshore demonstrator.
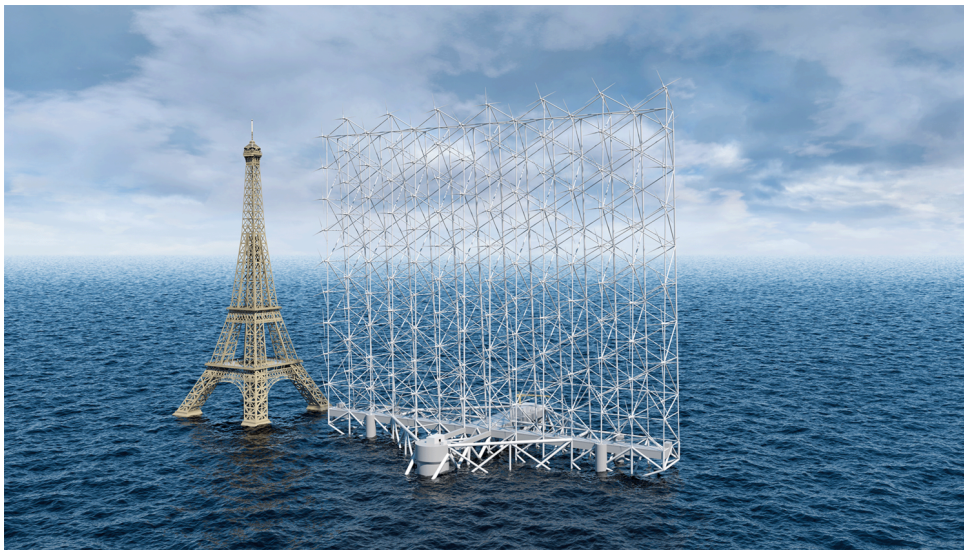
Figure 1.3: *Multirotor concept by Wind Catching Systems. Picture reproduced under kind permission from Wind Catching Systems [15].*

1.3 Aim of thesis

In this thesis, the wake behind different multirotor configurations/setups will be experimentally investigated in MarinLab (See Figure 1.4). The aim is to research the wakes of several setups with physical measurements, providing further understanding of multirotor wakes. Furthermore, the effect of rotor spacing, the number of discs, yawing, and an added support structure on the wake development will be investigated. In addition, the influence of laminar or turbulent incoming flow will be explored.

With the previous work on both multirotors and experimental investigations in MarinLab, the obtained results would hopefully provide new information on multirotor setups and methods for experimental investigations. The experimental model measurement could later be used to compare future computational fluid dynamic simulations to validate software and multirotor wake predictions.
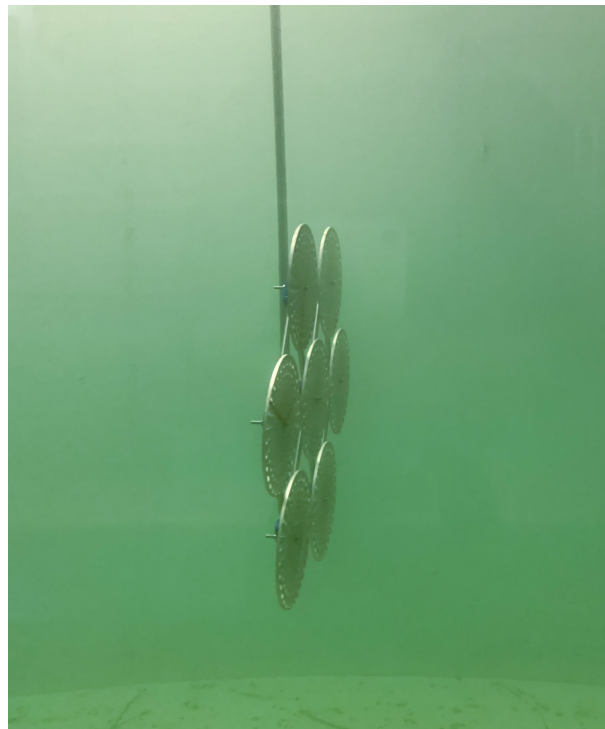
Figure 1.4: *A multirotor setup with seven actuator discs submerged in the towing tank at MarinLab.*

Chapter 2

Theory

2.1 One-dimensional momentum theory

2.1.1 Idealized single rotor

Wind turbines utilize the wind's kinetic energy, transforming it into mechanical energy that is further converted to electrical energy. The kinetic energy available in the wind depends on the wind velocity, U_o, over a given area, which for a turbine is the swept area, A. The kinetic power available over a wind turbine is given by [16]:

$$P_{wind} = \frac{1}{2}\rho_{air}AU_o^3 = \frac{E}{t} \tag{2.1}$$

where ρ_{air} is air density, E is energy and t is time. However, a wind turbine can not harvest all the available wind energy as that require the wind velocity to be reduced to zero behind the turbine, and this is not possible. This is explained by the one-dimensional momentum theory. Therefore, a power coefficient, C_p, is defined. C_p is the ratio between the wind turbine's power generation and the available energy in the wind. From the one-dimensional momentum theory a theoretical maximum power coefficient, $C_{p,max}$, called the Betz-limit exist.

For a simple examination of an SR wind turbine wake, the one-dimensional momentum theory can be utilized if the wind turbine rotor is regarded as an ideal actuator disc. Use of the ideal actuator disc model follows the following assumptions[16, 17]:

- Ideal fluid flow, meaning the flow is incompressible, has negligible viscosity, and is homogeneous.

- The flow outside the disc stream tube is not affected by other forces.

- The disc is non-rotating.

- The disc is permeable.

The one-dimensional momentum theory is derived from the conservation of mass and energy. In Figure 2.1 the streamlines over the rotor as a result of the one-dimensional momentum theory is illustrated. The velocity curve in Figure 2.1 emphasis that the wind velocity far upstream, U_0, also called the incoming velocity, slows down to the wind velocity over the rotor plane, u_d, and further decreases to a the wake velocity, u_w. The reduction is caused by the pressure drop over the rotor as seen in the pressure curve in Figure 2.1 created by the thrust force of the turbine, which also make the streamlines expand. Using the assumptions of the one-dimensional momentum theory and an ideal actuator disc, relationships between the thrust, T, and shaft power, P, can be derived by the velocities along the streamline.
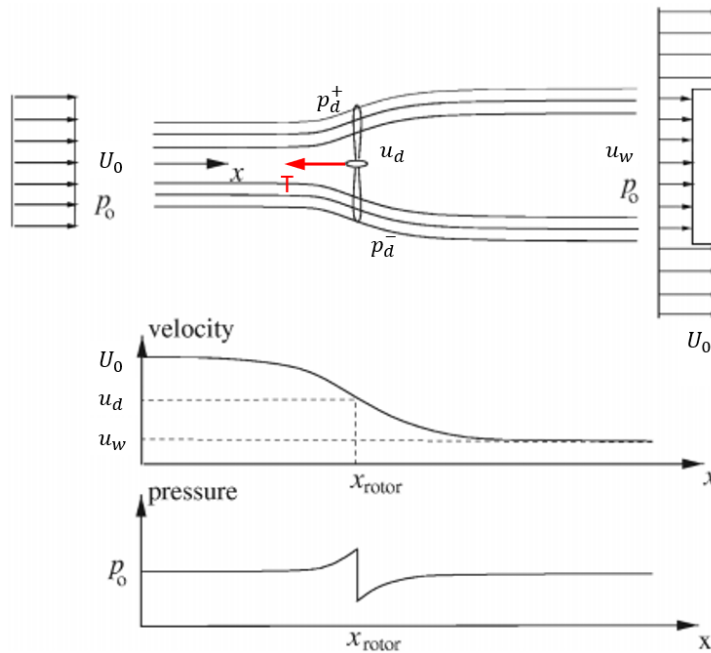
Figure 2.1: *Streamlines passing an idealized actuator or turbine affecting the up- and downstream velocity and pressure in the flow. Adapted from [16].*

The thrust caused by pressure drop over the rotor is derived from:

$$T = \Delta p A \qquad (2.2)$$

where $\Delta p = p_d^+ - p_d^-$ and is the pressure difference between just before and after the rotor. Another idealized assumption for the one-dimensional momentum theory is stationary,

incompressible, and frictionless flow. These assumptions validate Bernoulli's equation for the stream upstream, around the rotor, and downstream in the wake. From Bernoulli's equation, an expression for Δp can be derived as [16]:

$$\Delta p = 0.5\rho(U_0^2 - u_w^2) \tag{2.3}$$
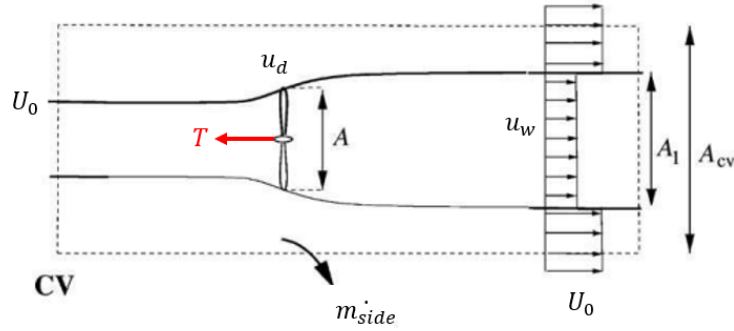
Figure 2.2: *Conservation of mass in a control volume (CV). Adapted from [16].*

With the simplified assumptions for an ideal rotor the axial momentum equation on integral form can be applied on a cylindrical control volume, seen in Figure 2.2, derives the following equation [16]:

$$\rho u_w^2 A_1 + \rho U_0^2 (A_{cv} - A_1) + \dot{m}_{side} U_0 - \rho U_0^2 A_{cv} = -T \tag{2.4}$$

$\dot{m}_{out}$ is the flow of mass out of the control volume and can be derived from the conservation of mass:

$$\dot{m}_{side} = \rho A_1 (U_0 - u_w) \tag{2.5}$$

Conservation of mass also yield a relationship between A and A_1 as:

$$\rho u_d A = \rho u_w A_1 \tag{2.6}$$

Combining these three equations T becomes:

$$T = \rho u_d A (U_0 - u_w) \tag{2.7}$$

T can then be replaced with equation 2.2 where equation 2.3 replace Δp in equation 2.2, which gives:

$$0.5\rho(U_0^2 - u_w^2) A = \rho u_d A (U_0 - u_w) \tag{2.8}$$

which solved for u_d gives:

$$u_d = 0.5(U_0 + u_w) \tag{2.9}$$

Equation 2.9 show that the wind velocity over the rotor is the mean of the initial (far upstream) wind velocity, U_0, and the wake velocity u_w. u_w is defined as the lowest velocity, or the highest velocity deficit, in the wake behind the turbine. The highest velocity deficit occurs immediately behind the turbine. Further downstream, the wake velocity will recover and ultimately achieve the initial stream velocity. The one-dimensional momentum theory does not take this fact into account.

2.1.2   Power and induction factor

As the flow is frictionless in the one-dimensional momentum theory, there is no energy loss from in to out in the stream. Therefore the ideal turbine power, P_t, is given by [16]:

$$P_t = \rho u_d A \left(\frac{1}{2} U_0^2 + \frac{p_o}{\rho} - \frac{1}{2} u_w^2 - \frac{p_o}{\rho} \right) = \frac{1}{2} \rho u_d A (U_0^2 - u_w^2) \tag{2.10}$$

The power coefficient, C_p, is used for easy comparison of different wind turbines. This dimensionless coefficient is defined as:

$$C_p = \frac{P_t}{P_{wind}} \tag{2.11}$$

By inserting equation 2.10 for P_t with with equation 2.9 for u_d, and 2.1 for P_{wind} the expression becomes[16]:

$$C_p = \frac{1}{2}(1 + b)(1 - b^2) = 4a(1 - a)^2 \tag{2.12}$$

where:

$$a = (1 - b)/2 = 1 - \frac{u_d}{U_0} \tag{2.13}$$

which is called the axial induction factor, and where:

$$b = \frac{u_w}{U_0} \tag{2.14}$$

From these relationships between a and the streamwise velocities we get the following expres-

sions:

$$u_d = (1-a)U_0 \tag{2.15}$$

$$u_w = (1-2a)U_0 \tag{2.16}$$

Similarly a thrust coefficient, C_T, can be defined as [16]:

$$C_T = \frac{T}{0.5\rho U_0^2 A} \tag{2.17}$$

which may be written as:

$$C_T = 4a(1-a) \tag{2.18}$$

2.1.3 Multirotor turbines

The one-dimensional momentum theory and the axial induction factor are based on one single disc in a stream resulting in no limitations for streamline expansion. However, when discs or turbines are placed close to each other, these theoretical models of looking at each turbine as isolated cases are not valid. In 2018, Bleeg et al. [12] discovered this when they compared estimations of power production from before the installation and actual energy production from after the installation of turbines at three wind farm sites. And the stream velocity was measured to be lower than estimated. Through *RANS* (Reynold-Averaged Navier Stokes) simulations, they concluded this occurred due to wind-farm-scale blockage. These blockage effects led to lower energy production by the front row turbines than the estimated prediction. The turbines produced less energy than if each wind turbine operated in isolation. These findings can indirectly be connected to MR wind turbines as they consist of different rotors working in the same stream. However, MR turbines' rotors are relatively closer to each other than SR turbines in a wind farm. Bleeg et al.'s findings confirm that objects in the same stream will be influenced by each other, making the one-dimensional momentum theory unfit to predict a multirotor turbine.

Nishino and Willden [14] investigated the efficiency of an array of tidal turbines partially blocking a wide channel with a new theoretical model using conservation of mass, momentum, and energy. They concluded that for a shallow channel cross-section where turbines block a small portion of the channel width, there is an optimal spacing between the turbines to maximize the efficiency of the combined array. It was suggested that local blockage increase

the efficiency as the spacing is reduced to an optimal distance, but a further reduction in the spacing decreased the efficiency. Their model also confirmed that another theoretical approximation than the one-dimensional momentum theory is needed when turbines are located close to each other.

2.2 Wake theory

2.2.1 Single rotor wake

The wake behind a wind turbine is divided into the near and far wake [18]. In Figure 2.3 the wake development of an SR wind turbine is illustrated seen from above. The near wake is defined from the region immediately after the rotor up to approximately two rotor diameters behind it. The far wake continues from the end of the near wake and further downstream. Generally, the wake development can be described with the initial wind velocity, $\bar{u}_0$ approaching the rotor and over the rotor will a velocity deficit, $\Delta\bar{u}$, occur. Further downstream in the far wake, the wake velocity, $\bar{u}$, will eventually recover.
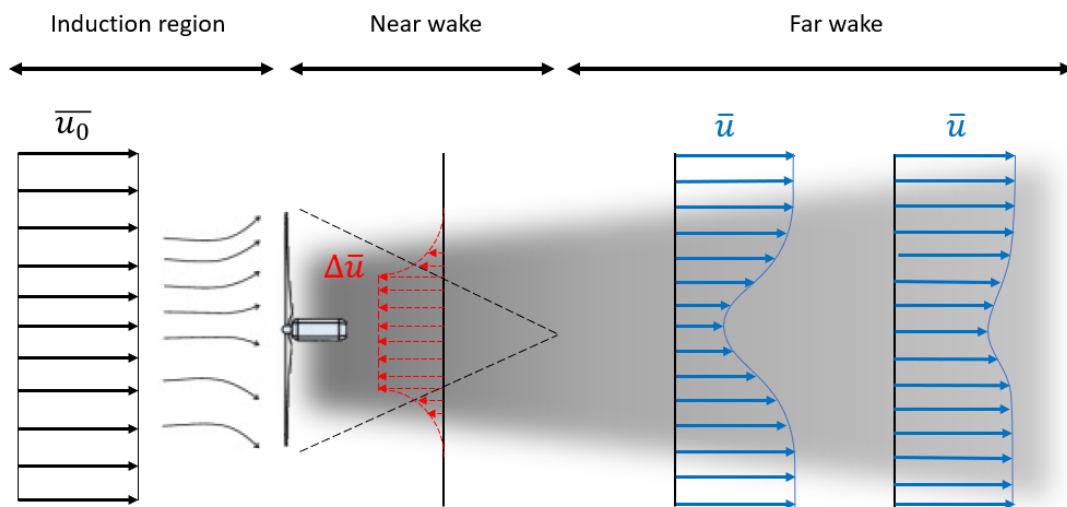
Figure 2.3: *Illustration of the wake velocity from a wind turbine in the three regions of flow; induction region, near wake and far wake. Adapted from [19].*

In the near wake, the presence of the turbine with its number of blades, the blades shape, and the tip vortices are evident and do determine the flow field appearance [18, 20]. The tip vortices at the tip of the rotor blade are caused by a pressure difference between the upper and lower sides of the blades [20]. The vortices move downstream in an expanding helical path and are highly turbulent, and play an essential role in the wake recovery and mixing

further downstream as the freestream fluids (flow outside the wake) are transported into the wake and mixed with the wake flow.

As explained by the one-dimensional momentum theory, the streamwise velocity of the fluid decreases when facing the blockage/drag set up by the turbine. Due to the pressure drop in the stream over the rotor, the lowest average velocity, $\Delta \bar{u}$, occurs just behind the turbine, as Figure 2.3 illustrates. The fluid inside and outside of the wake has different velocities, resulting in a shear layer [20]. In this shear layer, turbulent eddies are also created. The eddies from the shear layer and the vortices eventually mix the fluid particles, and the wake velocity recover.

The region beyond the near wake is defined as the far wake [19]. The actual rotor properties and movement do not play an essential part in the far wake development as the tip vortices have dissolved. What does matter in the far wake is the turbine in the flow [18]. Therefore is a porous disc suitable for far wake investigation and can be comparable with a rotating turbine [9, 21]. In the far wake, the focus is the wake model, wake interference, and wake turbulence. A downstream SR turbine can be placed 5 to 12 rotor diameters downstream [9, 22] depending on several conditions. The downstream turbine will operate in the far wake region of the upstream turbines in wind farm. Therefore, understanding the far wake is crucial for the placement of wind turbines in a wind farm. In the far wake, turbulent flow generated by the upstream turbine is evident. Higher turbulence level will lead to greater loads on downstream turbines, resulting in a shorter lifetime and higher maintenance costs. An unideal placement could significantly reduce the combined power output of a wind farm. The desired characteristic of the far wake is a low turbulent high-velocity flow for an optimal wind farm operation. For a downstream turbine to operate under good conditions are turbines often spaced by long distances. As mentioned in the introduction, research shows that MR wind turbines have a faster wake recovery, i.e., meaning the velocity and turbulence in the far wake region recover towards the initial wind conditions earlier than an SR wind turbine [8, 9].

2.2.2 Multirotor wake

From measurements [11], and computational simulations [13, 9], it is concluded that an MR create individual wakes in the near wake. The interaction of these near wakes is complicated to simulate.Oon-site measurements suggest that the rotor interaction, causing the MR effect, is beneficial for the wake recovery [11] and higher energy production. MR parameters such as

the number of rotors, inter-rotor spacing, and rotor diameter will affect the velocity deficit and turbulence in the near wake, setting the initial conditions for the wake recovery [9]. The highest velocity deficit occurs in the near wake for both SR and MR turbines but MR turbines reaches the highest velocity deficit faster [9]. As a rotating turbine creates tip vortices which move in a helical path downstream many tip vortices will be created in the near wake for MRs, these vortices are believed to early interact and dissolve. High-velocity jets through the space between the rotors in the MRS are also believed to be major contributors to the MRs having lower velocity deficit and reaching the highest velocity deficit earlier than SRs. In the near wake, the wake velocity starts gaining velocity after the wake reaches pressure equilibrium and MR turbines are suggested to reach this pressure equilibrium earlier than SR turbines [9, 13].

In the far wake region of an MR, the wake formation transition from rotor individual wakes to one uniform wake [9, 11]. The LES results by Bastankhah and Abkar indicated that when the MR wake form one uniform wake is the velocity recovery rate reduced. In the far wake the LES generally showed no difference in the velocity deficits between SR and MRs but a bit higher turbulence level for the SR. The effect of rotor spacing and the number of rotors in an MRS were also investigated with the computational model. Increased rotor spacing gave a faster wake recovery and lower velocity deficits. A higher number of rotors gave lower velocity deficits between 2D and 6D, but the rate of wake recovery in this region was lower with a higher number of rotors [9]. From 6D and downstream, the different number of rotors in an MRS did not result in different wakes [9]. At a downstream distance of 12D, the velocity deficit of an SR was similar to all the MRS, no matter the rotor spacing or number of rotors.

A topic regarding wake comparison is the definition of downstream distance. Bastankhah and Abkar define the streamwise direction as x/D, where D is the diameter of an SR [9]. The diameter of the SR is then used to define the diameter, d, of the, compared MR by

$$d = \frac{D}{\sqrt{n}} \qquad (2.19)$$

where n is the number of rotors. This relationship achieves the same swept area and is important when comparing the energy production. As an MR often have a distance between its rotors, it has a total diameter larger than the SR, called D_{tot}. Bastankhah and Abkar further use the D of an equivalent SR when comparing the downstream development of an MR with

different rotor spacing, without considering that the rotor spacing increase the total diameter of the turbine. The results can be significantly different if the wakes are compared with D or D_{tot}. The definition question has no right or wrong answer as it depends on what is investigated and if it is a direct comparison of a single MR units or in a wind farm context.

2.2.3 Turbulence

Two types of flow have been shown to exist; laminar and turbulent flow. In a laminar flow are the particles retaining their same relative position in a highly organized manner [23]. Turbulent flow is chaotic, and the particles have irregular unorganized motion [23]. Turbulence is naturally present in the ABL due to shear drag, surface drag, obstacles, and heat and moisture differences. For turbines are the condition of the incoming flow relevant. For the turbine structure, a higher turbulent flow will lead to fatigue loads, which affects a turbine's lifetime. Incoming turbulence does also affect the turbine wake development. Higher turbulence leads to higher mixing between the wake and surrounding flow and thus leads to faster wake recovery [10]. Bastankhah and Abkar [9] suggested that higher incoming turbulence might reduce the distance for an MR wake to transition from individual wakes to one single wake.

Wake turbulence consists of the inflow condition and rotor added turbulence. The rotor added turbulence is the turbulence added to the ambient inflow turbulence by the rotor. The wake turbulence can be presented as turbulent kinetic energy (tke) or turbulence intensity (TI). The turbulence is accessed over a time series with N measurement samples. The tke is given by the following equation:

$$tke = \frac{1}{2}\left(\left(\overline{u'_x}\right)^2 + \left(\overline{u'_y}\right)^2 + \left(\overline{u'_z}\right)^2\right) \quad \left[\frac{\text{m}^2}{\text{s}^2}\right] \tag{2.20}$$

where $\overline{u'_j}$ for each individual component is defined as:

$$\overline{u'_j} = \sqrt{\frac{1}{N}\sum_{i=1}^{N}(u'_i)^2} \quad \left[\frac{\text{m}}{\text{s}}\right] \tag{2.21}$$

u'_i is the measurement fluctuation from the mean velocity of the measurement series, u_{mean}, for each velocity component. Since the instantaneous values of tke can vary dramatically over a measurement series, is it helpful to use the mean to represent the overall flow better.

The TI is given by equation:

$$TI = \frac{u_{rms}}{U} \quad [-] \quad \text{or} \quad TI = \frac{u_{rms}}{U} \cdot 100 \quad [\%] \tag{2.22}$$

where u_{rms} is the root-mean-square of the velocity fluctuation of the measurement series and given by:

$$u_{rms} = \sqrt{\frac{1}{3}\left(\left(\overline{u'_x}\right)^2 + \left(\overline{u'_y}\right)^2 + \left(\overline{u'_z}\right)^2\right)} \quad \left[\frac{m}{s}\right] \tag{2.23}$$

and U:

$$U = \sqrt{U_{x,mean}^2 + U_{y,mean}^2 + U_{z,mean}^2} \quad \left[\frac{m}{s}\right] \tag{2.24}$$

where the $U_{j,mean}$ are the mean velocities of the three velocity components in the flow.

Computational models indicate that an MR generates lower added turbulence in the far wake with respect to an equivalent SR [9, 11]. Lower turbulence has also been observed for all downstream distances for an MR. However, this model used very large disc spacings [13]. The lower turbulence generated by MRs could benefit wind farm situations, leading to lower fatigue loads for downstream turbines.

2.2.4   Blockage

Blockage, or the blockage effect, is caused by objects blocking the path of the particles in a flow. The blockage leads to a reduction in velocity for particles approaching the objects. The one-dimension momentum theory describes this in Sec 2.1 for a single ideal disc. However, for a tidal turbine in a finite channel Garrett and Cummins [24] suggest that channel blockage occurs due to the channel wall boundary limiting the wake expansion, making the one-dimensional momentum theory invalid.

Bleeg et al. observed that the first array of turbines in a wind farm experienced blockage effects from the side-by-side turbines and the downstream turbines, which resulted in a decrease in the incoming velocity [12]. The side-by-side turbines evidently increase the blockage effect and lower the incoming velocity, reducing annual energy production compared to these turbines working in isolation. The annual energy production was estimated from the *wakes-only* approach where only the downstream wakes are assessed, leading to wrong energy production estimates [12]. For an array of turbines will also the middle turbines experience a lower velocity than the turbines on the edges, meaning the blockage effect is higher in the

middle of an array [12]. These effects were confirmed by Bjørnsen [25] with an experimental investigation of an array of three porous discs with varying disc spacing.

A link between the one-dimensional momentum theory, channel blockage, and blockage for an array of turbines is presented in Figure 2.4. For an array of turbines, the side turbines have a wider wake expansion than the middle turbine [25]. This expansion is explained by the channel blockage created by the side wakes, leading to a higher velocity deficit upstream of the middle turbine than if the middle turbine was placed in isolation. The side wakes only experience channel blockage from the middle wake making a wider wake expansion possible, which results in a lower velocity deficit, although higher than for an isolated turbine.
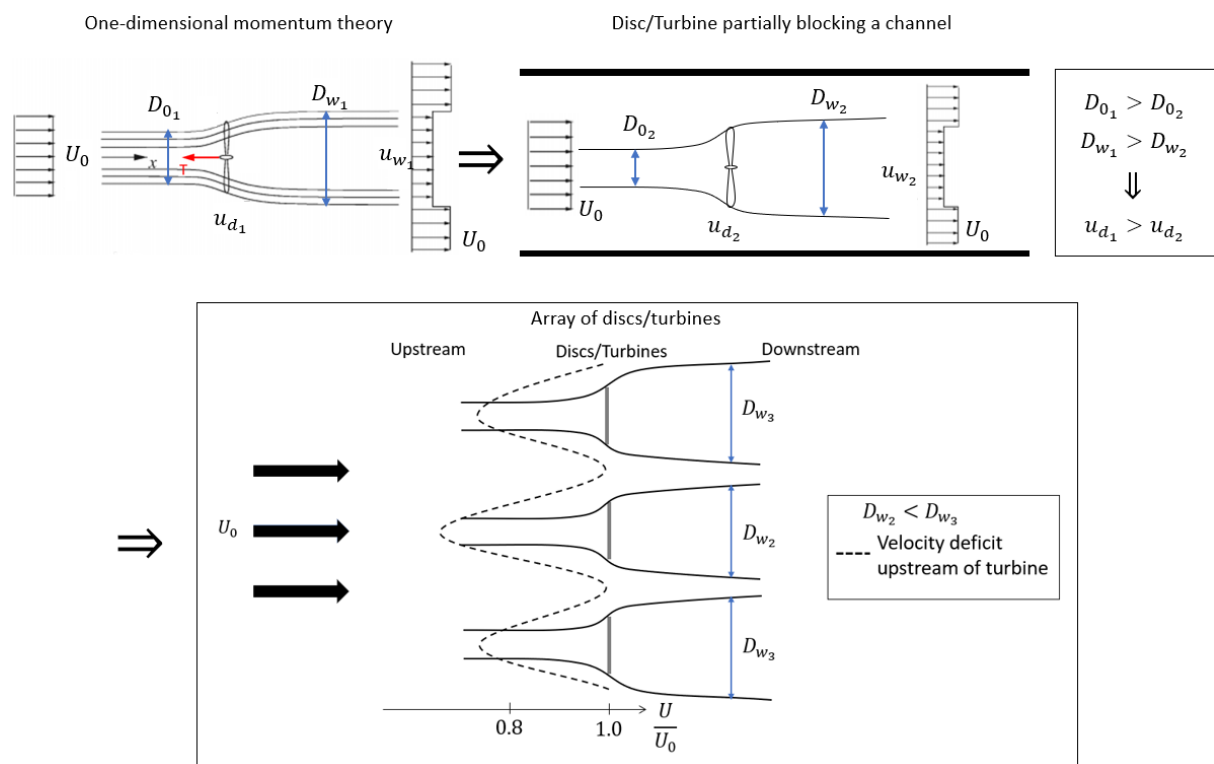
Figure 2.4: *Illustration of blockage effect in a array of discs/turbines linked to the one-dimensional momentum theory and channel blockage [12, 24, 25].*

Nishino and Willden [14] investigated an array of tidal turbines and discovered that theoretically could the local blockage effect increase the power coefficient for the array above the theoretical Betz limit with a new theoretical limiting power coefficient of 0.798. The local blockage is defined as the rptor area devided by the local square cross-sectional passage area surrounding the rotor. Further, they concluded that the power coefficient would solely depend on the local blockage for the rotors when placed in infinitely wide channel. Reducing the turbine spacing leads to a higher power coefficient up to a certain distance, where further

spacing reduction reduces the power coefficient. This concludes that optimal turbine spacing exists for achieving a higher power coefficient.

Bjørnsen [25] investigated these blockage effects on an array of three porous discs experimentally varying the disc center spacing *1d*, *2d* and *4d*, where *d* is the disc diameter. Velocity measurement of the upstream blockage at $x/d = -0.4$ and $x/d = -1.0$ for *1d* center spacing showed that the incoming flow experience the discs as one uniform blockage forming a Gaussian-shaped velocity profile at $x/d = -1.0$ but at $x/d = -0.4$ did the velocity profile have one global extreme point for the middle disc and two local extreme points for the side discs. For the downstream wake were three unique wakes observed in the near wake $x/d \leq 1.0$ and one single wake further downstream. These unique wakes show that high-velocity jets are present between the discs even with zero spacing between the edges. Increasing the disc separation led to more isolated blockage effects and wakes for each disc, faster wake recovery, and higher velocity jets between the discs.

Relating the findings of Bleeg et al. and Nishino and Willden to MR turbines suggests that an optimal rotor spacing exists to achieve the maximum power coefficient related to the local blockage. Bjørnsens results indicate that high velocity jets will be present in an MRS effecting the wake recovery positively.

2.2.5 Wake steering of multirotor wind turbines

Wake steering is a technique with SR wind turbines by controlling the yaw of the rotor, leading, or deflecting the wake away from downstream wind turbines. Yawing is also the mechanism for turning the turbine with the changing winds, and yawing of MR turbines is an issue of its own. Henceforth, yawing will be related to the wake steering of MR turbines. Yawing lead to a loss in the turbine's power output, but it can increase the overall annual production for a wind farm [26]. Howland et al. [26] explored the effectiveness of wake steering of an operational wind farm in Alberta, and wake steering was shown to increase production for a shorter period but was insignificant for the annual energy production for this specific farm. Results showed that the wake steering led to less variability in the wind farm's power production, and they concluded that wake steering could be beneficial for specific wind farm cases.

With an SR turbine, yawing will lead to a deflection of the wake, but MR turbines could potentially steer each rotor, which enables a possibility to affect the wake shape and recovery.

Yawing of each rotor can manipulate the wake to be expanded, channeled, or redirected, giving advantages for different cases. Speakman et al. [27] present five different yaw configurations; zero yaw, equal yaw, convergent yaw, divergent yaw, and equal crossed rotors, meaning the bottom two rotors are yawed to the left, and upper rotors are yawed to the right. Using LES, they investigate the effect these configurations have on the wake and wake recovery using a yaw angle of 30°. Yawing above 30° leads to no significant changes in wake deflection, and the momentum extraction is significantly reduced for an SR [28].

Results from Speakman et al. are presented by looking at a projection of the rotor area directly behind the rotor in the downstream wake. The LES results show that every yaw configuration leads to a lower normalized wake velocity deficit than the zero yaw configuration averaged over the rotor area. Also, the TI averaged over the rotor area is highest for the zero yaw configurations. The equal yaw configuration has the lowest velocity deficit and TI in the far wake since the wake is deflected away from the rotor area cross-section. However, the crossed rotor configuration has the lowest velocity deficit in the near wake. The divergent and crossed yaw configurations created a significantly wider wake expansion than zero yaw. As a result, the equal yaw deflected the wake like a yawed SR, and the convergent yaw channeled the wake towards the turbine center.

2.3   Multirotor parameters effect on the wake

Most studies of MRS have been conducted with CFD simulations, but data from the MR4 Vestas 4R-V29 also exist [9, 10, 11, 13]. With simulations and model experiments, MRS parameters can be changed to investigate the impact that different designs have on the wake development and blockage effects. This investigation is not suitable for full-scale MRSs. However, the available data indicate the relevance of simulations and model experiments. This section will present results from previous simulations on the influence of the parameters rotor spacing, rotor diameter, number of rotors, and rotor rotation on the wake.

2.3.1   Rotor spacing

For SR turbines in a wind farm is the spacing known to have a considerable impact on the wake development and is well-documented [9, 12, 18, 25], and a parallel can be drawn to MR rotor spacing. With an array of tidal turbines, Nishino and Willden showed that an optimal rotor spacing exists, achieving a maximum power coefficient [14], and this could be the case for MRs as well.

Ghaisas et al. [13] studied the rotor spacing effect on an MR4, and their findings showed no significant effect on the velocity deficit in the simulations. However, they studied a considerably large rotor spacing with tip clearance with factors of $1.0d$. For commercial and structural reasons, smaller tip clearances are expected. For example, the MR demonstrator 4R-V29 had a rotor spacing of $0.1d$. Bastankhah and Abkar [9] compared the velocity deficit for an SR turbine with MR4 turbines with three different rotor spacings with LES. The rotor spacings were 0.0, $0.1d$ and $0.25d$, where d is the diameter of one rotor. All three MR4 turbines showed lower velocity deficits at downstream distances 2-8D than the SR. An increase in rotor spacing led to a reduction in the velocity deficit and extended the distance for the formation of one single wake [9]. At a downstream distance of 12D, the velocity deficit for the SR and all rotor spacings converged towards the same value. The power production estimates showed no significant difference with a change in the rotor spacing.

2.3.2   Rotor diameter

The faster initial wake recovery of MR turbines is previously explained to be caused by the higher turbulence caused by higher mean flow shear [9]. The smaller the individual rotors

are, the shorter the length scale is to where the wake enters its far wake region. Therefore, will an MR7 with the same total area as an SR have individual wakes individually reaching their far wake earlier than the SR. Bastankhah and Abkar [9] studied wakes behind four SRs with different diameters. Their simulations showed that decreasing the rotor diameter led to faster recovery with the same downstream scale (x/D). To properly compare the different diameters, the velocity deficit was compared with a relative downstream scale (x/D_n), which resulted in almost identical velocity profiles for the four diameters. They concluded that the rotor diameter alone is not an essential factor. However, the rotor diameter is essential in comparing the effect of the number of rotors using different rotor diameters.

2.3.3   Number of rotors

Jameson et al. [8] suggests that the cost of an MRS will decrease with $\frac{1}{\sqrt{n}}$ with n representing the number of rotors. Based on this assumption, it should be desired to have an MRS with as many rotors as possible. How an increase in the number of rotors affects wake development has also been studied by Bastankhah and Abkar [9]. Using LES, the wake of an MR2, MR4, and MR7 with rotor spacing of $0.1d$ got compared with an SR. All the MRs have a swept area equal to the SR. The three MRs showed lower velocity deficits than the SR, and a higher number of rotors led to reduced velocity deficits in the near wake. The change of velocity deficit between the MRs reduced between each MR as the number of rotors increased. As mentioned in 2.3.2, a smaller rotor diameter leads to faster wake recovery in the near wake. Thus, for an MR, the smaller rotors will eventually form one uniform wake reducing the rate of wake recovery. The LES shows this as the wake recovery rate of the MR7 is reduced after $X \approx 2D$ and at $X \approx 3D$ has the velocity deficit of the MR4 reached the velocity deficit of the MR7, and then the two wake deficits follow each other. At $X \approx 5D$, the MR2 reached the same velocity deficit as the MR4 and MR7 and follows their velocity deficit curves. The SR reaches the velocity deficit as the MRs at $X \approx 10D$, and then all turbines have the same recovery and velocity deficits. The computational model estimated that an increase in the number of rotors also increased the power output. The power output of the MR2, MR4, and MR7 turbines were 1.5 %, 2 %, and 4 % higher, respectively, compared to the SR turbine [9].

2.3.4 Rotor rotation

With MRSs, an opportunity is to control the rotational direction of the individual rotors. One question is if this could positively affect wake recovery and power production.. Conservation of angular momentum says that a wake rotates in the opposite direction of the corresponding rotor. Therefore, if individual rotors in an MRS rotate in a different direction, the individual wakes created in the near wake will rotate in different directions.

Bastankhah and Abkar [9] suggested that rotor-induced swirl interaction could together transport outer wake flow into the wake resulting in faster wake recovery. This was investigated with the rotating porous disc model with six different rotation cases for an MR4 and concluded that rotation direction was almost negligible. The rotor spacing was $0.1d$ and the effect might be more significant for other rotor spacings. Rotor rotation is a possible advantage that MRS could utilize but is not regarded as a significant parameter for the wake development from an MRS at this stage.

2.4 Laws of scaling

Small-scale models are often used to study full-scale models in physical environments. The reason for doing small-scale experiments is to understand better the physical behavior of various systems in varying conditions. Advantages with small-scale models are that they are cheaper, easier to work with, easier to change the model, and enabling changing the environmental parameters. However, for a small-scale model to suitable represent the full-scale model in experiments, some scaling laws should be fulfilled to ensure similar behavior between the two models [29]:

- Geometrical similarity

- Kinematic similarity

- Dynamic similarity

Geometrical similarity means that two models have the same geometrical relations only with a different scale. The scaling factor, λ, are given by equation 2.25. By dividing the full-scale length with the equivalent length of a small-scale model, the geometrical ratio is defined. λ is used to define the rest of the model and surrounding environments. The rotor diameter of a full-scale turbine can be divided by the diameter of a porous disc, and a geometrical

relationship is obtained.

$$\lambda = \frac{L_{full-scale}}{L_{model-scale}} = \frac{L_F}{L_M}$$

(2.25)

The kinematic similarity will obtain velocities, so the full-scale and model-scale induce the same geometrical motion for both cases [29]. For example, the incoming wind velocity for a turbine and the incoming fluid velocity for a porous disc. The kinetic similarity ratio is given by:

$$\frac{u_F}{D_F} = \frac{u_M}{D_M}$$

(2.26)

where u is the incoming velocity and D is the diameter. The kinematic similarity is also related to angular speed, taking into account the rotation. However, this is not relevant for this thesis' experiments as no rotation is present.

To achieve dynamic similarity forces for full- and small-scale models, the different force contributions present must have the same ratio [29]. The forces of central importance are inertia forces, viscous forces, gravitational forces, pressure forces, elastic fluid forces, and surface forces. Important forces related to scaling in a porous disc are viscous and pressure forces. The similarity in the ratio of the viscous forces is obtained with an equal Reynolds number. The Reynolds number is given by:

$$Re = \frac{\rho u D}{\mu} = \frac{u D}{\nu}$$

(2.27)

ρ is the fluid density, μ is the fluid's dynamic viscosity, and ν is the fluid kinematic viscosity. However, a quick calculation of model velocity needed to achieve a similar Reynolds number between a full- and small-scale model show that the model velocities would be unrealistically high [25], and the similarities are not achieved. Piqué et al. [30] used The High Reynolds number Test Facility to pressurize a wind tunnel and achieve higher Reynolds numbers to investigate the effect of doing model-scale experiments with more similar Reynolds numbers. They saw no significant changes in the wake generation with increasing Reynolds numbers for the investigated Reynolds numbers.

For a circular object as a porous disc there should also be a Reynolds independence related to the objects thrust coefficient in experimental experiments, meaning that above a given Reynolds number the actuator disc should have the same thrust coefficient, making the disc Reynolds independent above this Reynolds number.

Chapter 3

Methodology

In this chapter, the experimental setup and equipment will be presented. Then, the measurement campaign and procedure will be explained, and the methods for data post-processing and presentation of the measurement data. Lastly, the measurement uncertainty and limitations will be presented and discussed.

3.1   Experimental setup

The experiments were conducted at HVL's MarinLab facility, a combined towing and wave generating tank (see Figure 3.1). The tank is filled with freshwater and has a length of 50 m, a width of 3 m, and a depth of 2.2 m [henceforth defined as the x-, y-, and z-direction, respectivley]. The wave generator is only used to mix seeding particles at the start of each day of testing. Two carriages are mounted to a wire moving in the x-direction. The travel length, velocity, and acceleration can be controlled with software. The disc setup is mounted to the main carriage and the measurement equipment on the second carriage, enabling changing the measurement distance from the discs. The water in the tank is not circulated or affected by any external forces. Therefore, it is considered stationary as long as sufficient time has passed since the last experimental run.
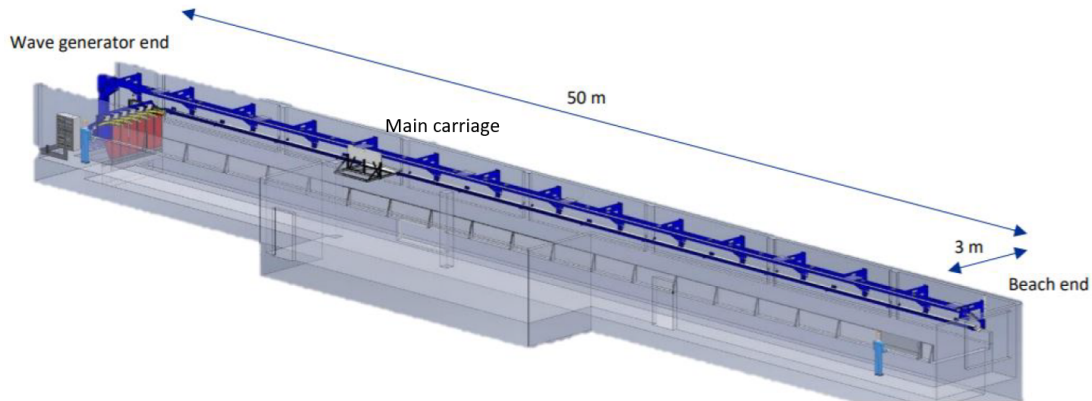
Figure 3.1: *Overview of the towing tank located in MarinLab at HVL, campus Bergen.*

3.1.1   The Carriage System

In conventional wake experiments with wind tunnels, the turbines, or discs, are stationary, and the fluid has a velocity running through the tunnel [21]. However, in a towing tank, the fluid is stationary, and the setup moves at a velocity. How both these methods can both investigate wakes will be presented in Sec. 3.1.3. The measurement equipment, an ADV, is mounted to the second carriage mounted to the same wire as the main carriage. An illustration of the setup of the carriage system is shown in Figure 3.2 and a photo from MarinLab in Figure 3.3. To change the measurement distance from the disc setup, *x/D*, the second carriage is moved manually.
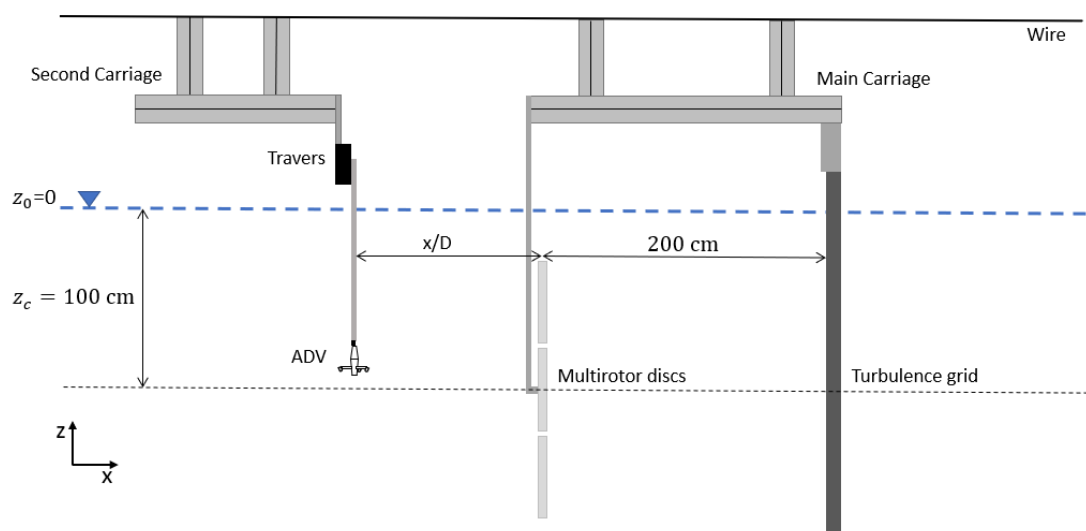
Figure 3.2: *Carriage system setup illustration.*
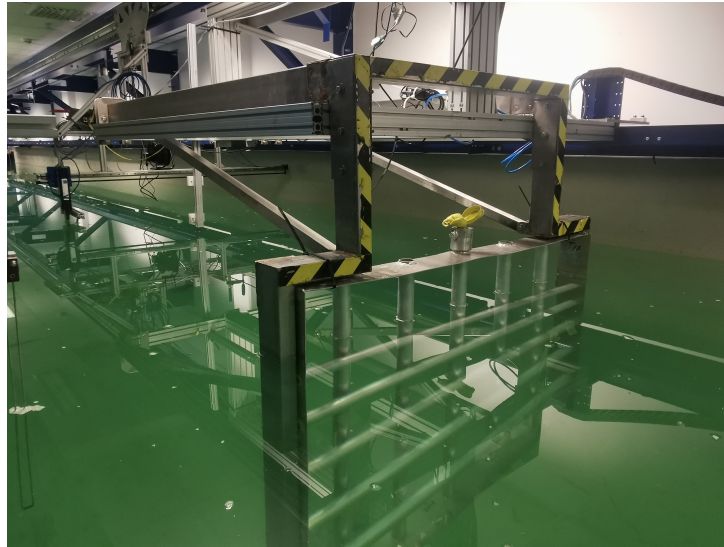
Figure 3.3: *The grid can be seen mounted to the front of the main carriage, and the disc setup at the end (with the white bricks). The grey horizontal bar in the background is the traverse with the ADV (black feature) mounted to it.*

3.1.2 Model scale porous disc

Model scale porous discs represent turbine rotors in this thesis, also called an actuator or permeable discs. It is essential to distinguish the model scale disc from the idealized actuator disc presented in Sec. 2.1.1 as the idealized assumption such as frictionless is not valid. The disc is illustrated in Figure 3.4 and has a solidity of 57 %. Leikvoll et al. [31] showed that this porous disc fulfil the requirement of Reynolds independence, obtaining a constant thrust coefficient for different velocities. The geometry with its trapezoidal holes let fluid pass through achieving a similar thrust coefficient as a rotating turbine and mirroring the flow of a rotating turbine in a simplified manner [21]. Using actuator discs instead of rotating horizontal-axis rotors makes simulations easier and less computational intensive [21] and physical experiments simpler and cheaper, especially when conducted in water.

There are no blades and no rotation, which means helical tip vortices will not be present in the wake induced by the actuator discs, only swirls and vortices from the edges. Helvig et al. [21] investigated different disc designs, uniform, and trapezoidal holed discs, to evaluate which model had the best wake characteristic fit of a rotating two-bladed turbine in a wind tunnel for up to a downstream distance of three diameters. They concluded that a 35% solidity actuator disc (NHD35) had the most similar characteristic, with a velocity deficit almost similar to the rotating turbine. Their results showed that instantaneous tip vortices behind the
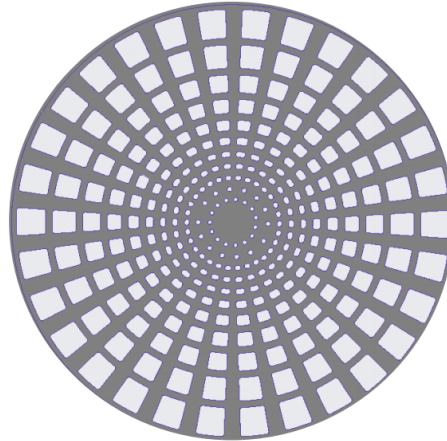
Figure 3.4: *Actuator disc with solidity 57 % which is used in physical experiments.*

two-bladed turbine were not present behind the best fitting actuator disc but concluded that the actuator disc is a reasonably good simplification of a two-bladed turbine across several mean parameters in the flow. For the near wake of the actuator disc, the instantaneous flow phenomena are not representative of the turbine. They observed a high turbulent flow in the upper edge of the blades due to the tip vortices. The tip vortices dissolve as the flow moves downstream and the turbulence diffuses. Behind the actuator disc, a highly turbulent field indicated that small-length scale vortices are created through the many holes in the actuator disc, but these quickly dissolve.

The two-bladed turbine Helvig et al. used was freely rotating and thus had a low thrust coefficient. For a three-bladed full-size turbine, the thrust coefficient is often 0.8 or higher [9] and a solidity around 60 % better represents the thrust coefficient of a three-bladed turbine. Behind the uniform holed 60 % solidity disc, Helvig et al. found that the disc produced a field wherein the wake velocity was negative, moving in the reversed direction. In contrast, behind the 60 % trapezoidal, this effect does not occur. Negative velocities can occur in the near wake for the actuator disc measurements. Using an actuator disc instead of a rotating turbine gives a good picture of velocity deficits, turbulence, and the behavior of the far wake. However, in the near wake ($x/D < 2$), the effect from the tip vortices is too different from the stationary actuator disc to give an accurate comparison.

3.1.3   Wake measurements in a towing tank

Wake measurements can be performed in both air and water. The aerodynamic similarities in air and water can be explained as both are Newtonian fluids [32], and both fluids follow the Reynolds scaling for incompressible flow at low velocities. Traditionally, turbine wakes are investigated using wind tunnel experiments [21, 33] but wakes investigations have also been investigated using water flumes [34, 35]. Kress et al. [36] investigated load fluctuations on a three-bladed turbine model in a towing tank. The difference between the wake generated by an actuator disc in a wind tunnel at NTNU and in MarinLab towing tank was investigated by an HVL bachelor group in 2020 [37]. They concluded that the wake velocity deficit and turbulent kinetic energy from the towing tank experiments were generally slightly higher than in the wind tunnel. One difference between the two compared experiments is that the wind tunnel's incoming velocity has some turbulence while the measurements in the towing tank had laminar incoming flow.

3.1.4   The Traverse

Mounted to the second carriage is a motorized traverse that enables moving the measurement equipment across the tank width and, thereby, the measurement position in the y-direction remotely with a LabView script. The traverse has a length of 1980 mm and is moved by a stepper motor with millimeter precision. First, calibration is done by resetting the traverse to its starting point. The reset was done each time the second carriage was adjusted. Next, a relative zero position at the centerline of the MR setup needs to be defined manually. This position is defined by taking several measurements around the disc setup center and seeing where the wake has the highest velocity deficit or symmetry around zero in the post-processing at $x/D = 2$.

3.1.5   Acoustic Doppler Velocimeter

The measurements of the wake velocity components u_x, u_y, and u_z are done with an Acoustic Doppler Velocimeter (ADV). An ADV measures the velocity components using the Doppler Shift principle. The ADV sends out an acoustic wave with a given frequency from a transmitter, hitting seeding particles in the tank and reflecting the acoustic waves. Four receiving probes pick up the changes in the frequency of the waves and can thereby decide the particle's velocity

vectors. The formula for this principle is:

$$f_{doppler} = -f_{transmitter} \cdot \frac{u}{c} \tag{3.1}$$

where $f_{doppler}$ is the receiving wave frequency, $f_{transmitter}$ is the transmitted wave frequency, and c is the speed of sound. With Eq. 3.1 can the velocity of the particles, u, for the three directions be calculated. In Figure 3.5 a schematic illustration of an ADV module is presented.
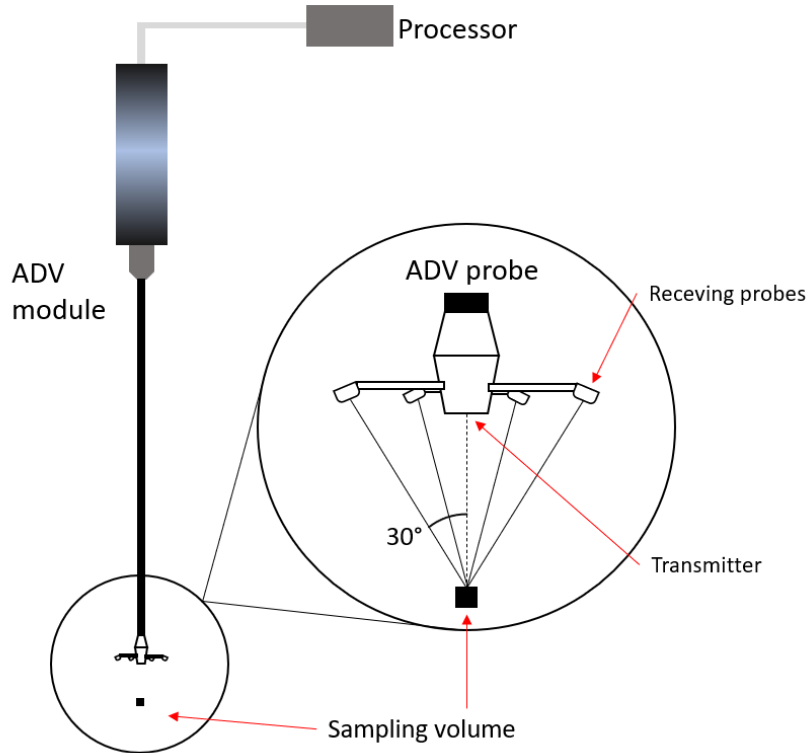
Figure 3.5: *Schematic illustration of the ADV module with four receiving probes.*

The ADV used in this thesis is the Vectrino velocimeter from NORTEK. This ADV has four receiving probes, meaning it measures the velocity in the x-, y-, z_1- and z_2-direction, i.e., two vertical components that should give similar velocities. The ADV measures with a sampling frequency of up to 200 Hz. In table 3.1 the technical specifications for the ADV are given.

Table 3.1: *Data for the Vectrino Velocimeter from NORTEK [38].*

Vectrino Velocimeter	
Samping distance from probe	50 mm
Sampling volume diameter	6 mm
Sampling volume height (user-selectable)	3-15 mm
Velocity range	±0.03, 0.1, 0.3, 1, 2.5, 4 m/s (software-selectable)
Accuracy	±0.5% of measured value ±1 mm/s

The acoustic beams transmitted by ADV are reflected due to seeding particles added in the tank over the whole length. These seeding particles are neutrally-buoyant glass spheres with a diameter of around 10 μm, and are made of a glass material [39]. The particles should enable the ADV to measure a clean signal by reflecting each acoustic beam. However, when the tank is not in use, the seeding particles sink or pack together, and during small wave experiments, the seeding particles are slowly pushed to the end of the tank. Therefore, sufficient mixing and adding new seeding particles was necessary during the measurement campaign. At the start of each measurement session, regular sinus waves were generated with the wave generator and run for 6 minutes or until a clean signal was achieved. At the same time, the carriages were run back and forward with the measurement setup mounted for additional mixing with the waves. The turbulence grid and larger disc configurations led to better mixing, shown by fewer outliers in the signal. In Sec. 3.2.2, the post-processing of the collected data and how outliers were handled are explained. In Sec. 3.4, the effect of the mixing quality is discussed.

3.1.6   Multirotor configurations

At MarinLab, several porous discs in aluminum with different diameters were available; one 70 cm, seven 20 cm, and thirteen 10 cm, all with a thickness of 5 mm. In addition, six identical porous discs with a 10 cm diameter were 3D printed in thermoplastic (PLA).

Multirotor

Different multirotor setup parameters have been investigated; the number of discs, inter-disc spacing, and yaw angle. The effects from the number of discs are compared between three configurations, MR4, MR7, and MR19, seen in Figure 3.6. For disc spacing the MR7 was investigated with three different disc spacings; 0.0d, 0.1d and 0.4d, where d is the diameter of the single discs, in this case 20 cm. Figure 3.6 show the spacing directions. The total diameter, D_{tot}, is the total diameter horizontally over the disc center, and D is defined as $D = d \cdot n$, where n is the number of discs along the horizontal center. An overview of the MR setups is given in Table 3.2.

The frame structures are created with 3D printed joints and stainless steel or aluminum (MR19) rods. In Figure 3.7, the frame is illustrated for the MR7. All setups are mounted to a 12 mm stainless steel rod in their center. The rod is mounted to the carriage. The MR4 and MR7 use discs with a 20 cm diameter, while the MR19 use 10 cm discs. The MR19 frame structure

is therefore scaled-down 1:2 from the MR7. The stainless steel rods have a diameter of 10 mm, while the aluminum rods for the MR19 have a diameter of 6 mm.
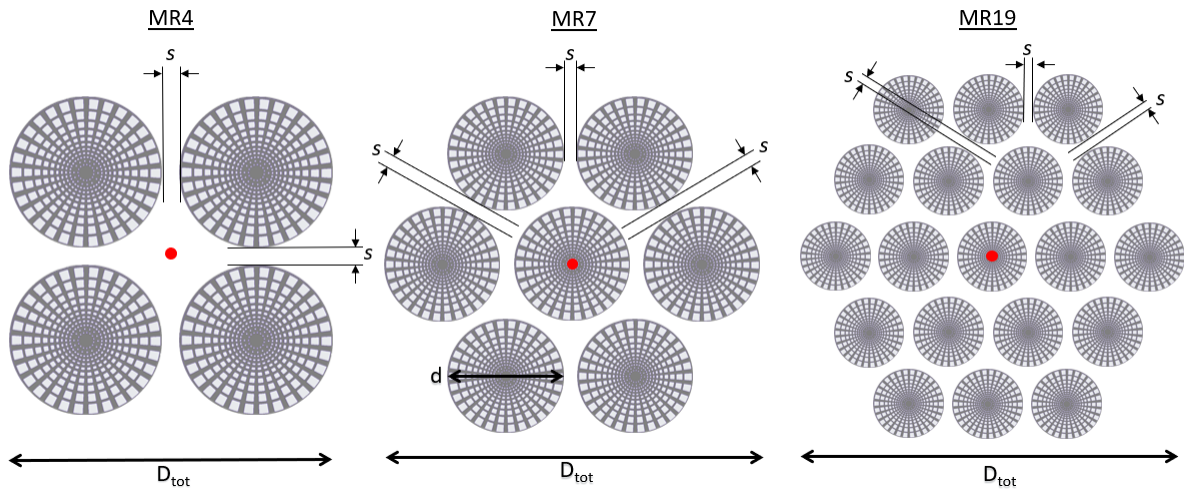
Figure 3.6: *The disc setups for MR4, MR7, and MR19. The disc spacing, s, indicates the spacing between the disc edges horizontally and vertically for MR4 and horizontally and at an angle for MR7 and MR14. D_{tot} is the total diameter, and d is the disc diameter. The red dots define the disc centers for each setup.*

Table 3.2: *Overview of MR setups.*

MR setup	d [cm]	s [cm]	D [cm]	D_{tot} [cm]
MR4	20	$0.1d$	40	42
		$0.0d$		60
MR7	20	$0.1d$	60	64
		$0.4d$		76
MR19	10	$0.1d$	50	54
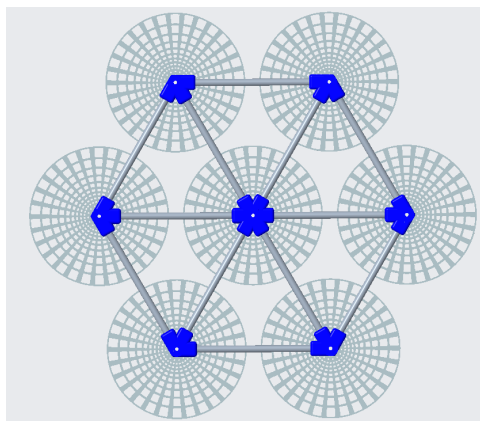
Figure 3.7: *The back of the MR7 showing the frame structure.*

The yaw, the angle between the incoming flow direction and MR setup, is adjusted by adding a 10° angle to each joint and rotating the tower with 10°. Three yaw configurations have been

investigated; 10° individual disc yaw, 10° tower yaw, and combined yaw with 10° disc yaw with -10° tower yaw (see Figure 3.8).
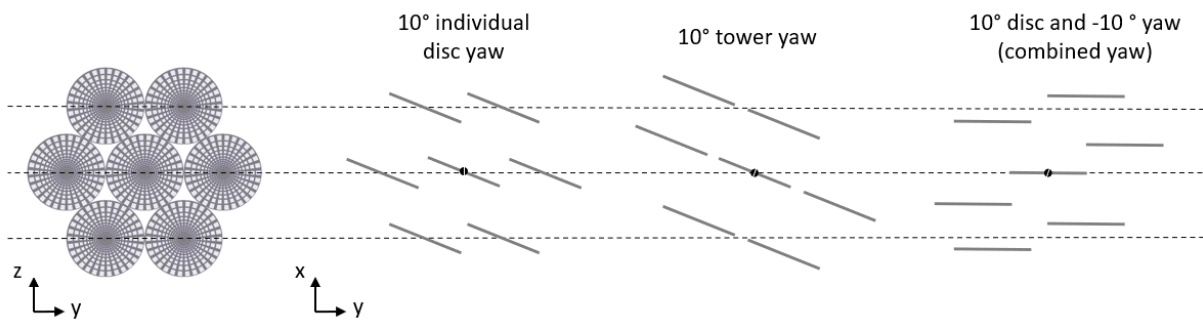
Figure 3.8: *Sectional top view of the three yaw configurations.*

Multirotor Windcatching Systems Frame Structure

The last MR setup is an MR7 with $0.1d$ spacing with an additional frame in the streamwise direction illustrated in Figure 3.9 and forward referred to as the WC7. This setup is investigated due to talks with Wind Catching Systems, who informed us that they plan to build an MR7 with a frame similar to the one planned for their 25 GW MR turbine. The frame for the WC7 is inspired by the Wind Catching frame and might give insight into how a frame like this will affect wake development.
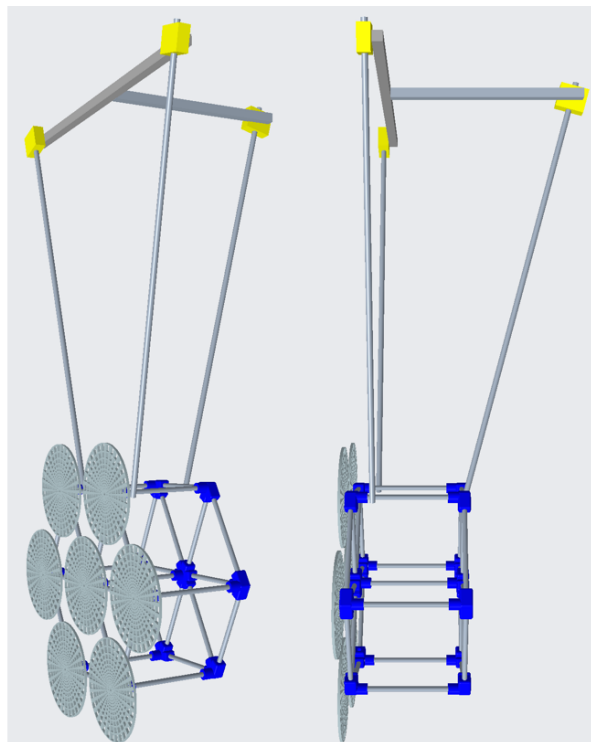
Figure 3.9: *3D model of the WC7 structure.*

Single rotor

Wake measurements are also completed on SR discs to compare with the MRs. Two SR discs
are used; a 20 cm diameter disc similar to the one used in the MR4 and MR7, called SR_{20}, and
a 70 cm diameter disc, the SR_{70}. The SR_{20} disc is mounted to the same tower as the MRs, but
the SR_{70} is mounted to a different tower. Another tower needed to be used due to increased
drag forces which induced bending and oscillation when mounted to the tower used for the
MRs. The SR_{70} is presented in Figure 3.10 and is part of a parallel ongoing master thesis by
Sindre Øye, where further information regarding its setup can be found [40]. This tower led to
some differences in the test parameters compared to the smaller tower. In addition, the SR_{70}
has an offset in the streamwise direction from the tower due to a nacelle. This offset led to the
disc being closer to the turbulence grid than the MRs. The nacelle also has a tail that blocks
space for the wake to expand into, which might affect the wake.
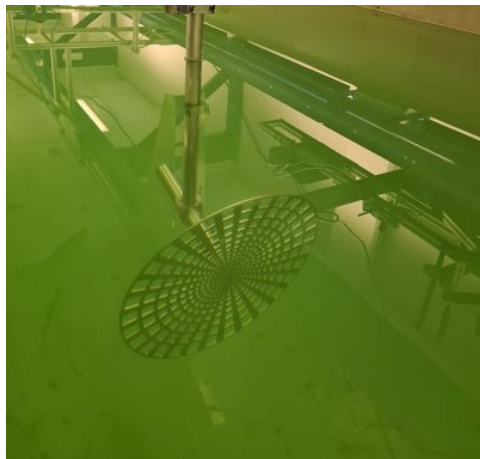
Figure 3.10: *SR_{70} submerged in the tank with its tower and nacelle.*

3.1.7   Turbulence grid

Turbulent incoming velocity in the towing tank is generated with a turbulence grid mounted
to the front of the main carriage as shown in Figure 3.2. The grid parameters are given in Table
3.3 and Figure 3.11. As seen in Figure 3.11 the discs will be placed close to the lowest part
of the grid. The grid is 1.45 m wide and goes to a depth of 1.35 m. As the tank is 3.0 m wide
and 2.2 m deep, the grid does not cover the cross-section completely. The distance from the
center of the grid and discs to the edge of the grid is 725 mm, which means that laminar and
higher velocity flow will be present at the sides of the wakes and might influence the wake
recovery. At downstream distances ≤7D, the wake might expand outside the grid and into the

surrounding flow.

Table 3.3: *Turbulence grid properties.*

b [cm]	M [cm]	M/b	Solidity
5	25	5	0.36

The characteristics of the flow and turbulence created by the turbulence grid have been investigated and presented in Sec 4.1.1 to indicate how the turbulent and laminar flow behave and interact using the grid. Wake profiles were measured at 0.6 m, 1.2 m, 2.0, 2.5 m, 5.0 m, and 10.0 m downstream from the turbulence grid. Centerline measurements were also measured at 3.0 m, 4.0 m, 6.4 m, and 8.4 m. The measurement depth was 50 cm. The MR setups were mounted 2.0 m downstream from the grid.
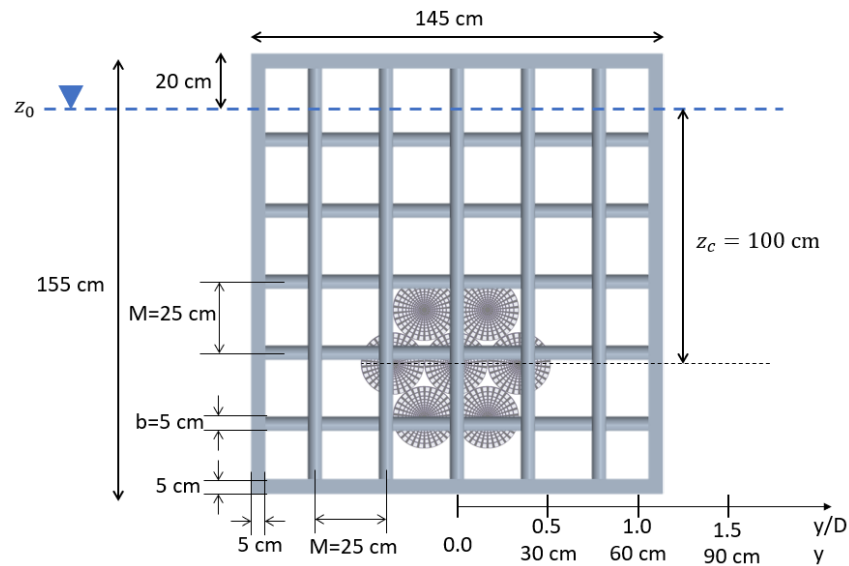
Figure 3.11: *Illustration of the MR7 with no disc spacing behind the turbulence grid. y/D is shown for D = 60 cm.*

3.2   Measurement procedure & Data Post-Processing

3.2.1   Wake Measurements

In Figure 3.12 the locations of the lateral wake profiles and centerline are illustrated for an MR7. All wakes are measured at a depth of 100 cm for all setups. The wake profiles are measured at downstream distances of 2D, 4D, 7D and 10D. Due to symmetry, the wake profiles are measured in detail at one-half of the disc setup and mirrored over the disc center. However, some measurements are measured at the opposite side to detect if the wake was not symmetrical due to an angle offset or wrongly defined disc center. Around the disc center at 2D several measurements are conducted to find the position of $y = 0$ with the ADV. The highest velocity deficit and symmetry define the disc center.
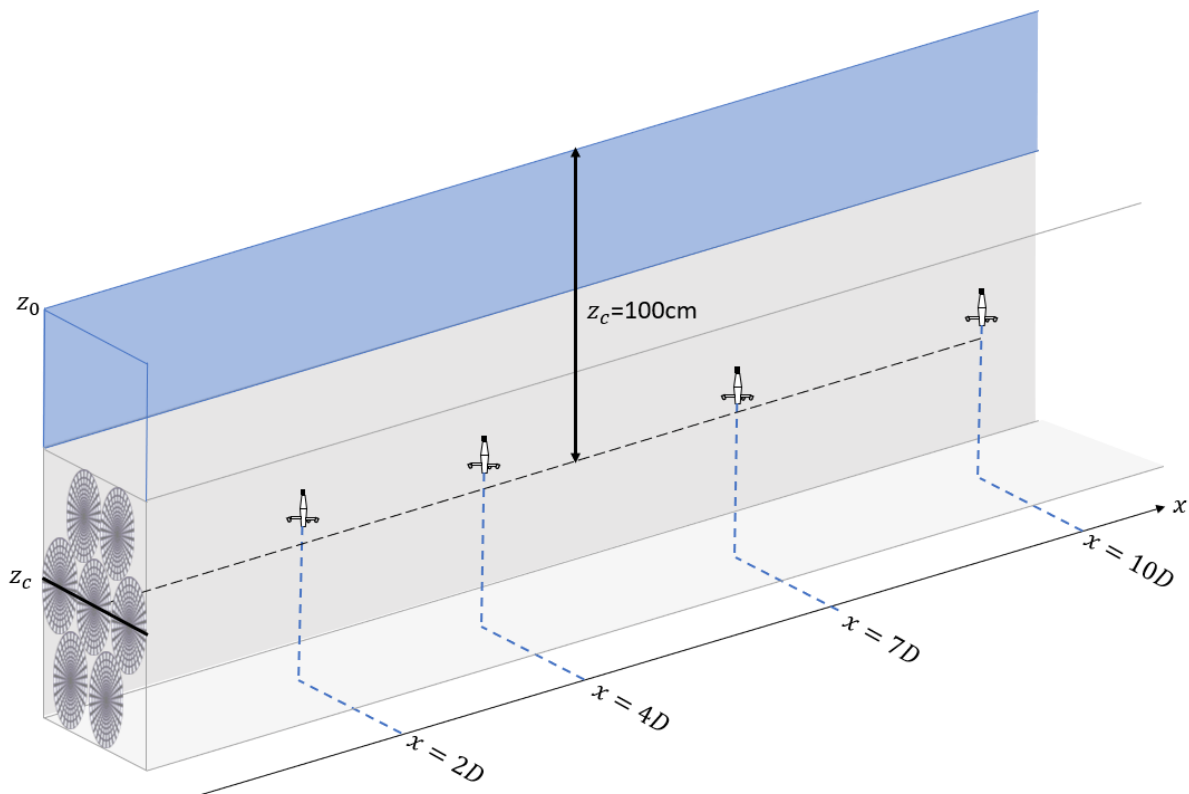
Figure 3.12: *The measurement campaign showing location of the downstream distances for the lateral wake profiles and the centerline at disc center.*

Using just one ADV to measure lateral wake profiles and centerline measurements is time-consuming. Before a measurement can start, the water should be relatively still, and it takes 3 minutes for the ADV to read ≈ 0.0 cm/s after a measurement has been run. One measurement run takes approximately 1.5 minutes, and it takes 1 minute to rewind the carriage to the starting position. Together it takes approximately 5.5 minutes to obtain one measurement

point, and therefore only one-half of the wake is investigated. Also, fewer measurements are measured at *7D* and *10D* since the importance of many measurements is lower as the wakes are more mixed and with fewer variations across the wakes. After analyzing the first obtained data, a decision was made to exclude the 4*D* wake measurements for the next wakes measured as this region was less important at this early stage of wake investigation. The wake profiles were measured with 15 - 30 measurement points with an interval of 10 to 40 mm, depending on disc setup and downstream distance. Table 3.4 gives an overview of all wake measurements presented in this thesis, excluding the measurements on the turbulence grid. Two incoming velocities, U_0, have been used; 0.4 m/s for the laminar incoming flow and 0.337 m/s for the turbulent flow. The turbulent incoming flow velocity generated by the grid has been found experimentally in Sec. 4.1.1.

Table 3.4: *Overview of wake measurements for this thesis.*

Turbine type/ Number of rotors	Inflow	Spacing	Number of wake profiles	Number of measurements at centerline
SR	Laminar (SR_{20})	-	4	19
	Turbulence (SR_{70})	-	4	10
MR4	Laminar	$0.1d$	4*	32*
MR7	Laminar	$0.0d$	3* + 6**	-
		$0.1d$	3 + 4* + 6**	-
		$0.4d$	3* + 6**	-
	Turbulence	$0.0d$	4	-
		$0.1d$	4	19
		$0.4d$	4	-
MR19	Laminar	$0.1d$	3	19
WC7	Laminar	$0.1d$	3	-

Turbine type/ Number of rotors	Spacing	Disc yaw [degree]	Tower Yaw [degree]
MR7	$0.1d$	10	0
		0	10
		10	-10
One wake profile at x/D = 2 with laminar inflow			

*Measured by Jørs and Mjåtveit [41].

**Measured in collaboration with Koi [42].

3.2.2   Data Post-Processing

All data are collected with the ADV and processed in MATLAB. For efficient post-processing, the ADV sample recordings were started simultaneously as the carriages and stopped when the carriages had stopped.

Figure 3.13 show a sample recording of the x-velocity component measured by the ADV in a wake. The blue line shows the acceleration and deceleration and where the turbulence has affected the wake around sample number 2000. The red line is the measurement of the fully developed wake. These samples are used for further post-processing.
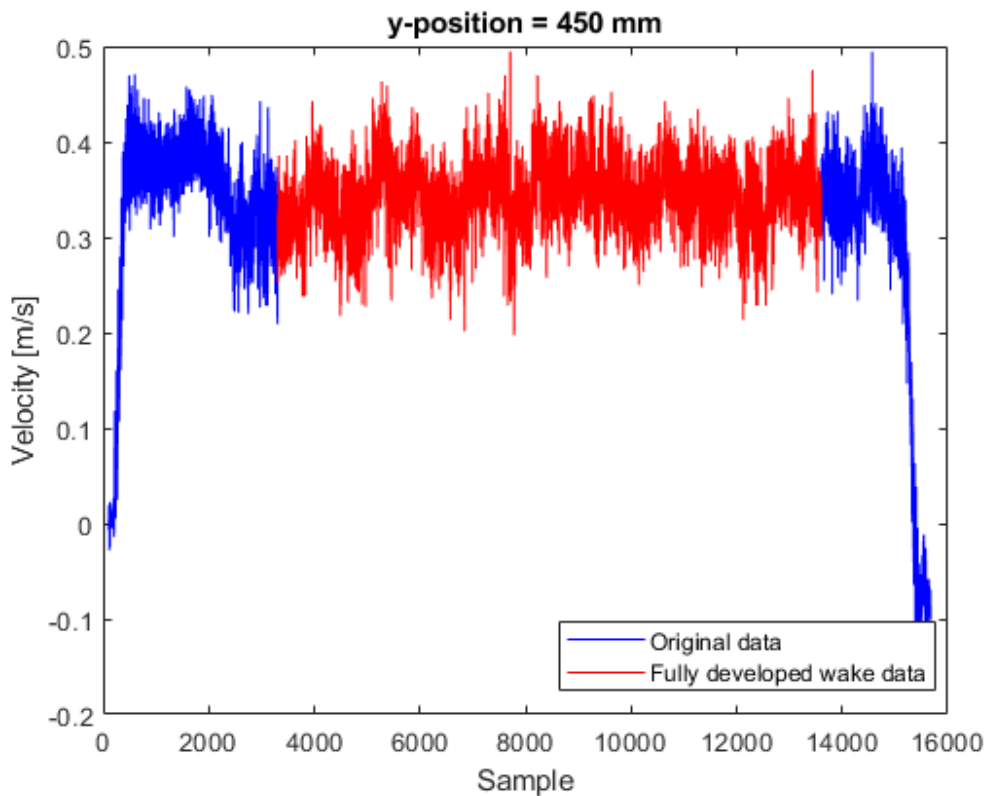
Figure 3.13: *Sample recording for MR7 in turbulence at 2D downstream distance at y-position 450 mm showing the original (blue) and cut (red) data samples.*

Due to different downstream distances and limitations of the tank length, fewer samples are included for further downstream wake profile measurements as the starting point of the fully developed wake changes. Therefore, different lengths of a measurement series were investigated to understand how the number of data samples included influenced the accuracy of the results. The starting sample of the measurements is kept constant, but the length of the developed wake data included is changed and set to 10300, 8300, 6300, 4300,

and 2300 samples. Figure 3.14 shows the standard deviation for the average velocities in the streamwise direction for each measurement point for the different measurement series lengths in percentage relative to the averaged velocity of the 10300 sample length. The lines indicate the absolute average deviations from the 10300 sample length in percentage and calculated with equation 3.2.

$$\sigma_{\text{length}} = \sum_{i=1}^{n} \frac{\sqrt{\left(\overline{x_{\text{length}_i}} - \overline{x_{10300_i}}\right)^2}}{\overline{x_{10300_i}}} \cdot \frac{100}{n} \quad [\%] \tag{3.2}$$

Figure 3.14 shows that the average velocity varies more towards the middle of the wake for all sample lengths and approaches the average velocity of the 10300 sample length towards the outside of the wake. Lengths of 4300 and 2300 samples give values that differ significantly from those with 10300 samples. Lengths of 8300 and 6300 give better corresponding values. However, 6300 could give a deviation over 5 %. The dotted lines show the average deviation of the whole wake. They clearly show how more samples better comply with the 10300 sample length. The shortest measurement length conducted in this thesis is 6300 samples for the measurement of SR_{70} at a downstream distance of $10D$. Figure 3.14 indicate an average deviation of ≈ 1.5 % for these measurements. However, these deviations depend on the stability velocity measurement, and at a downstream distance of $10D$, the velocities are steadier than at $2D$, leading to lower deviations. The measurements also vary more behind the disc from 0 to 0.5 y/D than outside.

Although the measurement quality was good and mostly without noise, some outliers did occur with the ADV measurements. Outliers occur either due to bad particle mixing or an error in the measurement signal and are shown in Figure 3.15. To filter out these outliers a Hampel filter was used. The Hampel filter was set to evaluate 200 neighboring samples and check if the evaluated sample's standard deviation is four times greater than the median absolute deviation of the neighboring samples. If the evaluated sample fulfilled this condition, the filter replaces the outlier sample with the mean of the 200 neighboring samples. A hypothesis was that the filtering might affect the results due to the several outliers present in previous work [25, 41] due to this filter method. In Sec. 3.4 data with bad signal quality from previous experiments and new measurements with good quality will be compared to investigate the influence the Hampel filter could have on the wake results.
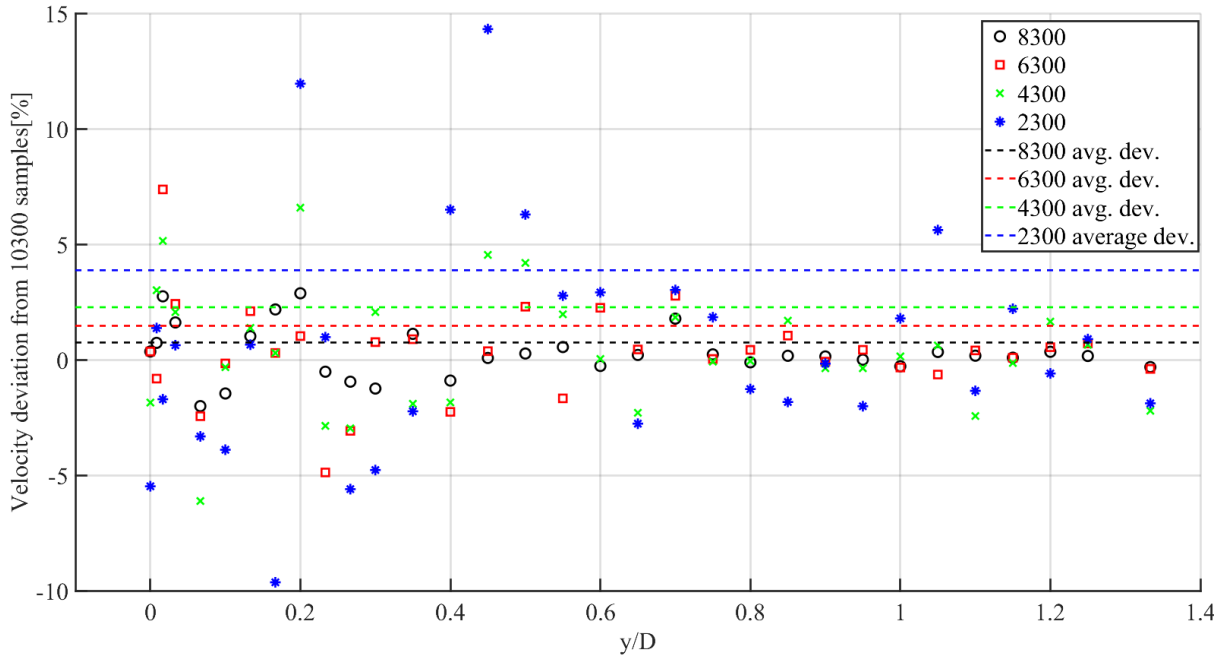
Figure 3.14: *Four measurement lengths, 8300, 6300, 4300 and 2300 samples, are compared to data for 10300 data samples lengths. The plotted points show the percentage deviation from the corresponding velocity in the x-direction in the measurement with 10300 data samples. The lines is the average absolute deviation from 10300 for each of the 4 measurements lengths.*
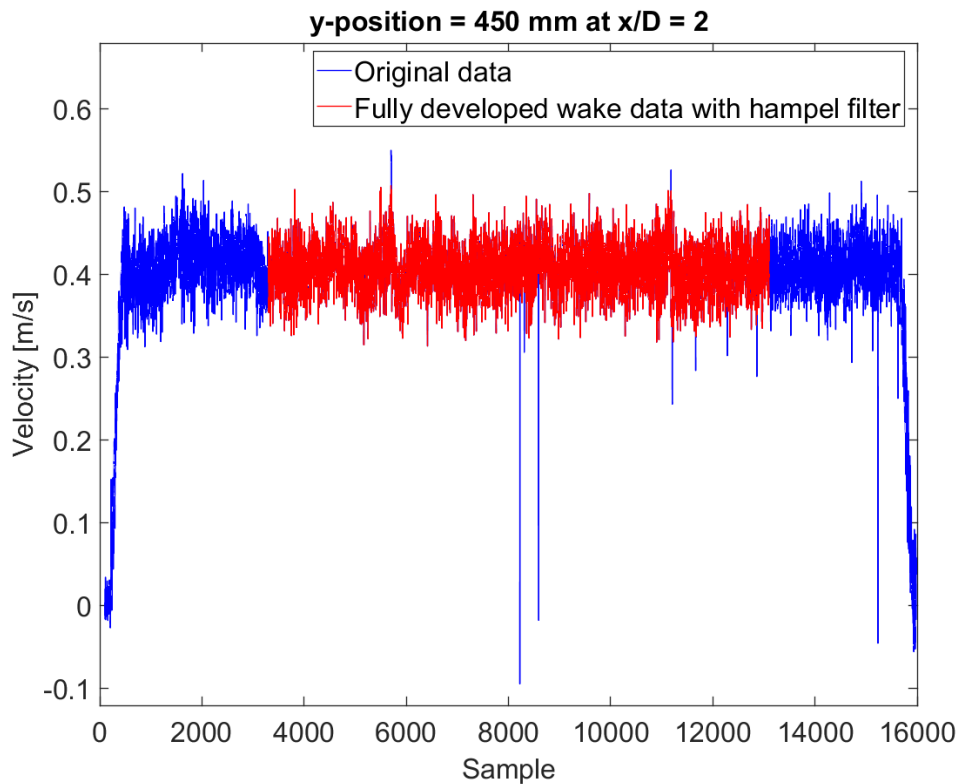
Figure 3.15: *Sample recording for MR7 in laminar flow at 2D downstream distance at y-position 450 mm. The red data samples are the data contained for further post-processing, showing how outliers are filtered with the Hampel filter.*

The measurements are mainly presented with lateral wake profiles. First, the profiles are plotted with measurements from the positive y/D y-axis, and then the plot is mirrored over the x-axis. The measurement points are then indicated with points on the graph on the positive side. The wake velocity is presented with a normalized velocity deficit. The term normalized velocity deficit is chosen as it gives no denomination and can be compared with other wake measurements. The equation for normalized velocity deficit is:

$$U_{vd} = \frac{U_0 - U_{mean}}{U_0} \quad [-] \tag{3.3}$$

where U_0 is the incoming velocity and U_{mean} is the mean velocity for each measurement point. A $U_{vd} = 0$ shows no velocity deficit, $U_{vd} = 1$ means no velocity, and above one indicates particles having a negative velocity moving opposite of the incoming flow. For some velocity presentations, just normalized velocity is used, which is defined by:

$$U_v = \frac{U_{mean}}{U_0} \quad [-] \tag{3.4}$$

A polynomial fit has been applied to the measured lateral wake profile to achieve comparable values for maximum velocity deficits and the wake widths of different wakes. A 10th-degree polynomial has been used as it best fitted the wake measurements and is illustrated in Figure 3.16. $U_{vd,max}$ is the maximum velocity deficit, and the wake widths are defined as the width where the wake velocity is half of the maximum, $\frac{U_{vd,max}}{2}$. The wake width is further divided by the disc configuration diameter D_{tot}. The results are presented in Sec. 4.1 in Table 4.1 and 4.2.
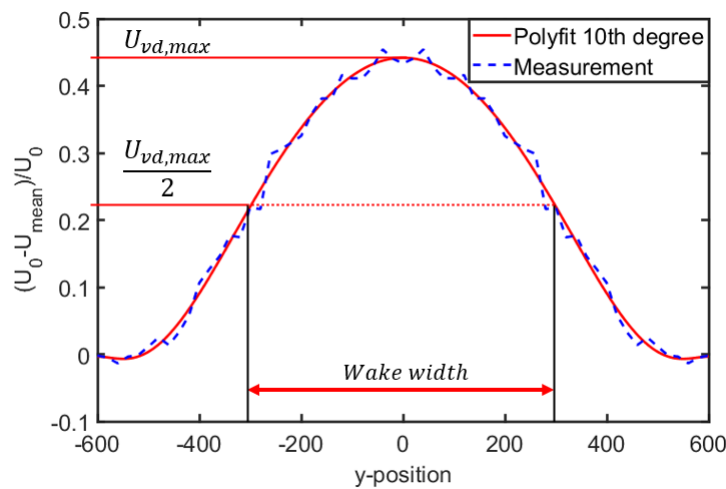
Figure 3.16: *Use of 10th degree polynomial fit to define a maximum velocity deficit, $U_{vd,max}$, and a wake width.*

3.3   Measurement uncertainty & Experimental limitations

In an experiment, several sources of error and uncertainty exist. The uncertainty of the measurements can be divided into two categories; systematic and random error. Systematic errors generally occur in every measurement series, usually related to the measurement equipment. Examples could be instrument damage, wrong calibration, or interference from external sources, typically influencing the equipment's accuracy. Other systematic errors can also be related to the setup methods. Random error is due to factors that vary with each measurement and can not be controlled. There are often many limitations to the repeatability of the measurements and limitations related to the facilities and equipment for physical experiments. Various uncertainty and limitations of the measurement campaign and the associated results will be presented in this section.

3.3.1   Systematic error

The systematic error in the experiments is linked to the ADV and the manual mounting and adjusting of equipment. The signal from the ADV depends on three things; particle mixing, positioning, and cable interference. Regarding particle mixing, a higher amount of seeding will lead to better signal and measurement accuracy. Sufficient mixing is necessary to reduce this error. To accurately quantify this systematic error was not possible further than comparing the difference between good and bad mixing from previous measurements (See Sec. 3.4). A diagnosis check integrated into the ADV software was run to investigate if the ADV had any damage. It showed that no damage had occurred to the device. The ADV measurement in the three directions is dependent on the correct rotational position of the ADV, which means if the x-direction were not parallel to the actual x-direction, a lower streamwise velocity would be measured. To avoid cable interference, the signal cable was placed with a sufficient distance to the 230 V power supply cable, which was was identified as a source of interference before the measurement campaign begun.

Human errors have most likely led to systematic errors due to manual adjustments. For example, the measurement depth of the ADV and the disc setup depth were found by manually measuring 100 cm from the sample location and disc center, respectively, and indicated on the mounting rods with a marker line for the water surface. This was only done once and used for the whole campaign and could have led to a systematic error measuring at the wrong

location for all measurements. A spirit level was utilized to ensure that the dist and ADV were mounted with no angel. However, the human eye reading from the spirit level decides if it is correct in the end and could have led to a systematic error for the different setups. The distance between the ADV and disc setup is also set manually with a measuring tape hanging over the water surface, leading to systematic error. Although many human errors are present, they are not believed to impact the uncertainties of the results related to them significantly.

A few measurements have defined the incoming velocity and turbulence level behind the turbulence grid at a 2-meter downstream distance. An implication could be that the defined incoming velocity is inaccurate, and several results are normalized with the wrong incoming velocity.

3.3.2 Random error

The primary source of random error is believed to be caused by the difference in the tank between each measurement. The particles move around, and sometimes the ADV might measure in an area where the mixing is not similar to the rest of the tank. The movement from the previous run might also be present and give random errors in the measurements. However, as Sec. 3.4 will show, these errors might not have a significant effect on the results presented. Interference on electrical equipment could also be presented as a random error. However, this is not changed throughout the measurements and is mainly believed to be a systematic error. It was observed in the data reading from the ADV that the wire and carriages might induce vibrations from the wire and rail into the experimental setup affecting the ADV measurement. However, as a measurement series consists of several thousand samples, these random errors will even out. Random human errors could be starting a measurement too early, but none has been identified.

3.3.3 Limitations

Turbulence grid

The turbulence grid was built for another experiment comparing two different measurement equipment in turbulent flow and not for the generation of a turbulent incoming flow for wake investigations [43]. Therefore, the grid is not suited for this type of experiment as the grid only covers 30 % of the cross-section of the towing tank, leading to unwanted higher velocity

laminar flow surrounding the turbulent flow and the disc wakes. A grid covering the whole cross-section would be most suitable and desired. The discs, as mentioned, were also located almost outside the bottom of the grid, which is not ideal but will most likely not have made the results unusable.

The turbulent eddies created by the turbulence grid could not be scaled with the diameter of the disc setup, and the SR_{70} disc was used to obtain a comparable length-scale for the eddies between the two disc setups. The SR_{70} tower that had to be used led to the SR_{70} disc being located 25 cm closer to the grid and thereby located with an unknown incoming velocity and turbulence.

Equipment and setup

With just one ADV available, it can take up to 3 hours to get one wake profile, limiting how many measurements and setups can be investigated. The desired procedure would be to have each measurement point closer to the next one and measure a higher number of wake profiles to get a full understanding of the wake development but this was not possible due to the time limitation.

The SR and MR setups would be best suited for comparison if each setup's disc area was equal. This similarity would ensure an accurate comparison between the rotor size and swept area of the setups, and the same measurement points for the lateral wake profiles could be used. However, to achieve this would require many different discs with specific diameters and an additional cost to have the discs ordered. However, as the results are presented in relative terms when comparing different setups, this difference is believed insignificant, but this is not investigated. The towers which the disc setups are mounted to are not scaled relative to the disc setup, however, this would probably lead to insignificant differences.

3.4   Previous experimental results at MarinLab

Several experimental investigations of wakes behind actuator discs have been conducted in MarinLab [25, 37, 41, 44]; single rotor wake, wind farm wakes, and multirotor wakes. Bjørnsen [25] investigated what depth the center of a disc no longer was influenced by the free-water surface. With a 20 cm disc, did the results show that the deeper the disc center was positioned, the lower was the z-velocity component. Higher incoming velocity led to a higher z-velocity in the wake. With the center at a depth 1.5 times the diameter of the disc, 30 cm, the z-velocity was negligible at an incoming velocity of 0.5 m/s.

Bjørnsen [25] also completed repeated measurements at three lateral positions in the wake behind one disc with the ADV. The objective was to estimate the ADV's precision when measuring the wake velocity. The measurements were conducted in the wake at disc center $y/D = 0$ with six measurements, and two positions close to the disc edge, $y/D = 0.4$ and $y/D = 0.45$ with four measurements. The repeated measurements showed a higher standard deviation for the center measurements and the closest to the edge. However, the accuracy of the ADV is given in Sec. 3.1.5, and what he explored was the uncertainty or precision in the wake representation. Generally, these measurements show that the results show some uncertainty which could be larger in at the disc edge where the turbulence is highest but the uncertainty is regarded as low, especially as the new measurements have a better signal as well.

Aasnæs had a similar approach investigating the velocity measurement deviation at different downstream distances behind two arrays of discs [44]. The measurements were done at downstream distances of 2.5, 3.5, and 6.0. The first was measured four times, and the others three times. These measurements were not conducted at the exact lateral location and give no direct correlation. However, they gave a general indication that the deviation for the measurements is lower the further downstream the wake measurement is conducted.

In the spring of 2021, Jørs and Mjåtveit [41] completed initial investigations of multirotor wakes in their bachelor thesis. Their data have been provided for further use to compare different multirotor wakes and further evaluate the quality of this experimental procedure in MarinLab. One MR4 and three MR7s with the laminar flow were investigated. After a new evaluation of their results, it is evident that a higher signal quality was possible to archive. The effect of this has been further investigated to understand the implication of

the different signal qualities. In Figure 3.17, two measurement series of an MR7 in laminar flow at the MR's center are presented. The plot showing the previous measurement with *bad mixing* is the measurement conducted by Jørs and Mjåtveit, and the *good mixing* is a new measurement measured after the turbulence grid was used for mixing. The signal quality is significantly better for the new measurement leading to less filtering of the signal. The previous measurement was begun with the carriage in motion and ended before it stopped, affecting which measurements are included in the series. The measurements conducted in this thesis are started together with the carriage, then the start of the start of the sample series are cut and including a fixed number of samples number cutting out the end.
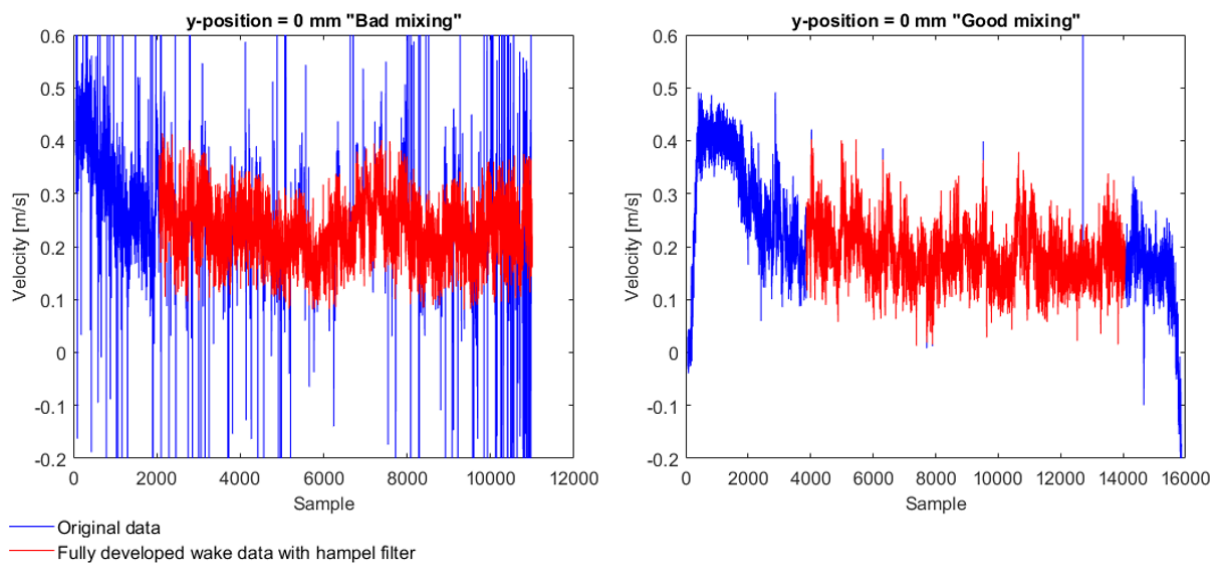
Figure 3.17: Comparison of two data series of the streamwise velocity measurements at MR7 y/D=0 with laminar incoming velocity with "bad" (previous measurement) and "good" (new measurement) particle mixing.

Figure 3.18 and 3.19 compare the wake velocity deficit and tke from the previous and new measurements at downstream distances 2D, 7D, and 10D. The lateral profiles for the normalized velocity deficit in Figure 3.18 shows similar wakes at $x = 2D$. For $X = 7D$ and $10D$, the new measurements show higher velocity deficits than the previous measurements. At $\approx y/D_{tot} = 1$, outside the created wake, the two measurements should both measure approximately zero velocity deficit, but a small offset between the two measurements is observed. The lower velocity deficit could be caused by unknown differences between the setups or other systematic or random errors.

A theory for the bad signal turbulence results was that heavy filtering would filter out turbulence data and affect the results. In Figure 3.19 the normalized tke for the wakes are presented.

Keeping the differences from Figure 3.18 in mind, only a general comparison of the tke results is possible. The tke levels at $X = 2D$ follow each other well and have the same maximum tke level. At $X = 7D$, the average level for the previous measurements is a bit higher. However, the new measurements coincide with previous measurements at three locations. At $X = 10D$, both measurements show similar results.
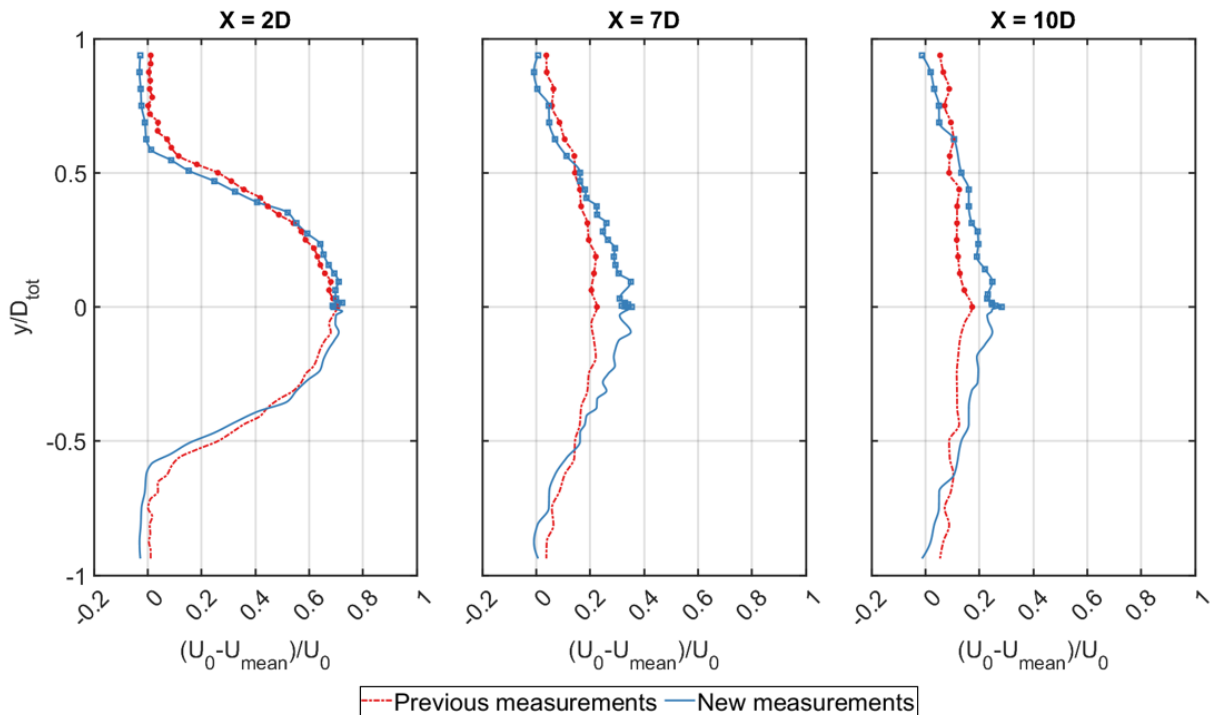
Figure 3.18: *Normalized velocity deficit wake profiles for MR7 0.1d in laminar flow for the downstream distances 2D, 7D ,and 10D for the previous and new measurements.*

Comparing the measurements conducted by Jørs and Mjåtveit [41] with the new measurements, which have a higher signal quality with less filtering, indicates that their measurements are usable and give a good representation of the wake phenomena. However, the new obtained signal quality is favored.
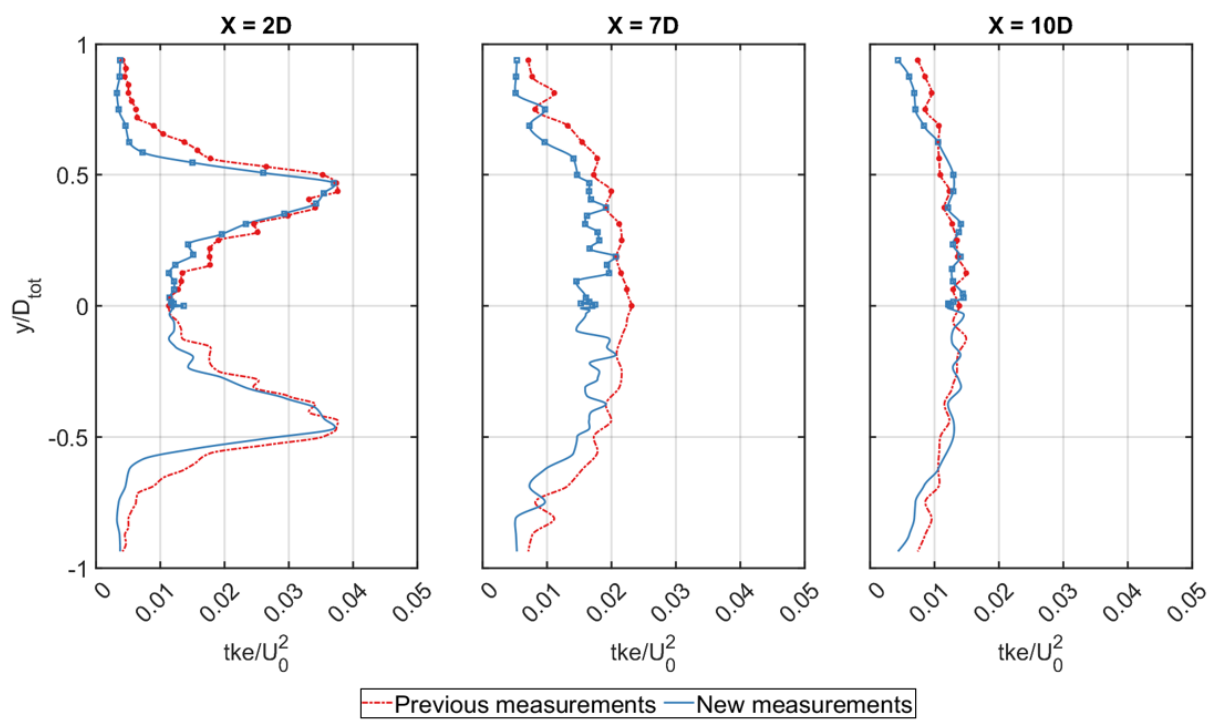
Figure 3.19: *Normalized turbulence kinetic energy wake profiles for MR7 0.1d in laminar flow for the downstream distances 2D, 7D, and 10D for the previous and new measurements.*

Chapter 4

Results and Discussion

The obtained results from the measurement campaign will in this chapter be presented in Sec. 4.1. First, the results are presented with graphs, scatter plots, and tables with the respective measurements to compare the effects different setup parameters have on the wake development for an MRS. Then, in Sec. 4.2, the presented results will be further discussed and put in context with previous measurements and published computational results.

4.1 Results

4.1.1 Characterization of the turbulence grid

Six lateral wake profiles and four centerline measurements have been conducted to characterize the wake generated by the turbulence grid. The mean velocity, tke, and TI of the wake behind the grid have been quantified to understand the turbulence grid's abilities for turbulence generation. This characterization is essential to understand what effects can influence the wake generated by the disc setup operating in the grid-generated turbulence.

The turbulence grid is dragged at a speed of 0.4 m/s, and the mean normalized velocities across the turbulence grid at the downstream distance of 2.0 m are presented in Figure 4.1. The disc setups will be placed at a 2.0 m distance from the grid. The average velocity in the streamwise direction, u_{mean}, behind the grid area is calculated to be 0.337 m/s and will later be used as the initial velocity for the disc setups placed in the turbulent flow. Henceforth is the grid area defined as the area covered by the grid, meaning between ± 0.725 m. The velocity outside of the grid area is significantly higher than the incoming velocity and is believed to be

due to the blockage effect caused by the grid. The grid covers 49 % of the tank's width, and multiplying this with the solidity gives a blockage of 17.64 % of the tank's width by the grid. This lead to an increase in velocity as the flow has limited space for expansion.
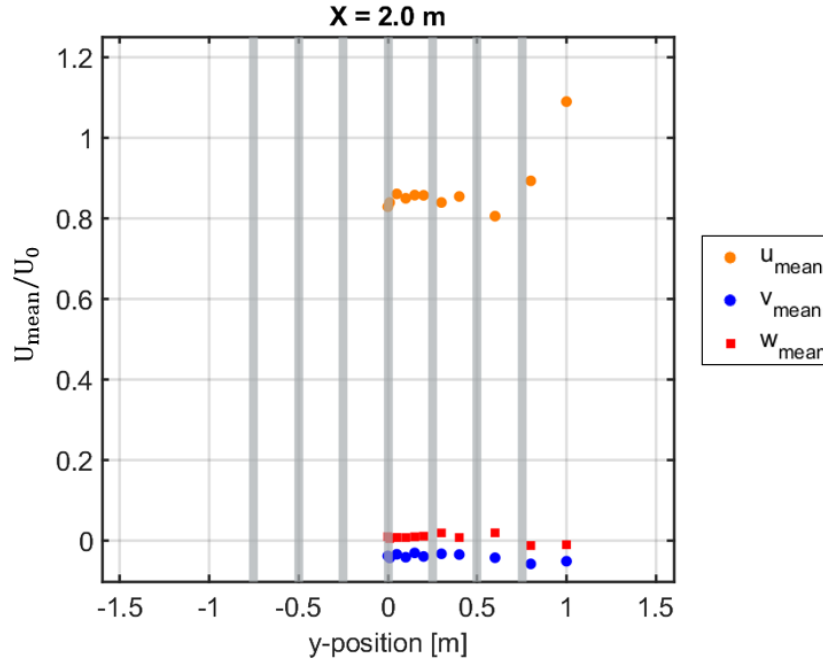
Figure 4.1: *Normalized mean velocities across the wake at a downstream distance of 2.0 m at a water depth of 50 cm. All three velocity components, u, v, and w are presented. The vertical grid bars are illustrated in grey.*

The higher velocity flow outside of the grid area is also evident in Figure 4.2 which presents the velocities in the streamwise direction at each measurement point. At 0.6 m, higher velocity jets passing through the grid mesh are evident. These high-velocity jets eventually blend to form an almost uniform flow at 2.0 m.

From Figure 4.1 and 4.2 only small varieties in velocity between the bars are evident at $x = 2.0$ m and 2.5 m. It can also be observed that the velocity is at its lowest at $y \approx 0.625$ for both x = 2.0 m and 2.5 m, indicated with a darker blue color in Figure 4.2. Outside of the grid area are the velocities significantly higher than the initial velocity of 0.4 m/s for all lateral wake measurements, even at downstream distances of 5.0 m and 10.0 m, but weaker than at 2.5 m. This higher velocity around the grid seems to mix with the turbulent flow slowly, and at 10 m, the velocities behind the grid area have increased. In contrast, the velocities outside have decreased from above 0.46 m/s to $\approx$0.42 m/s.

From 2.0 m and further downstream, a constant velocity is desired as the wake recovery of the grid will not significantly interfere with the wake recovery of the disc setups. Figure
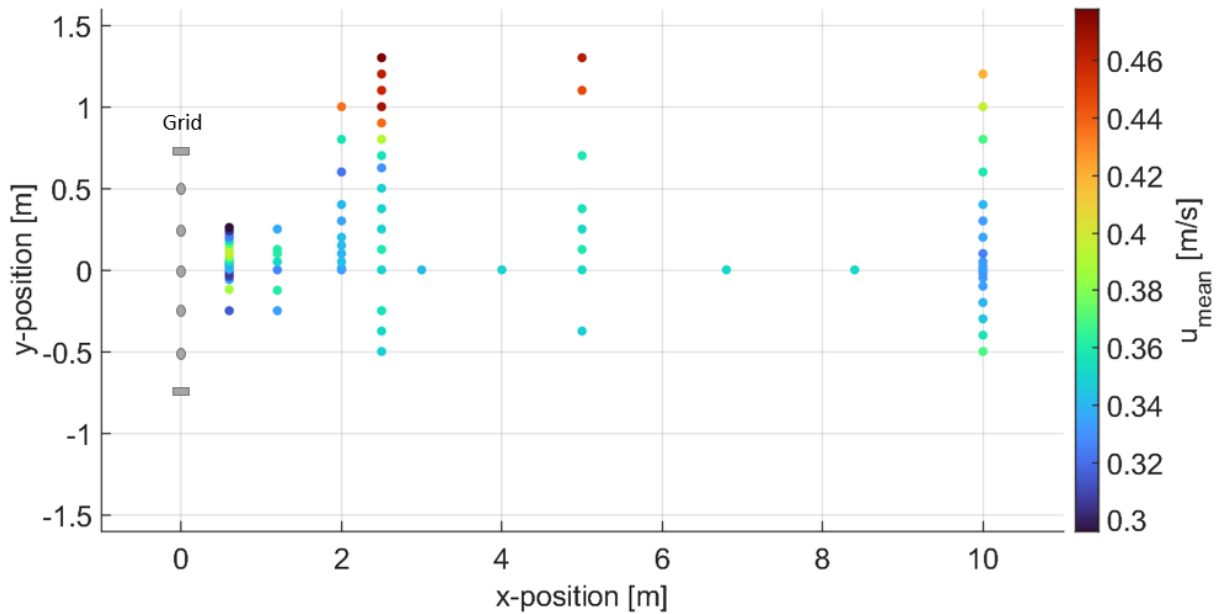
Figure 4.2: *Contour scatter plot of the normalized velocity deficit for each measurement point.*

4.3 presents the average of the velocities and tke measured behind the grid area for the downstream distances. Several of the averaged values are around 0.35 m/s, except 2.0 m and 10.0 m, where the averaged velocities are 0.337 m/s and 0.340 m/s. The velocity increased 5.07 % from 2.0 m to 5.0 m. However, the difference from 2.0 m to 10.0 m is just a 0.89 % increase in velocity.

It should be noted that the distances 3.0, 4.0, 6.8, and 8.4 are just single measurement points at the centerline, while 0.6, 1.2, 2.0, 2.5, 5.0, and 10.0 are the average of the lateral measurements points behind the grid area.
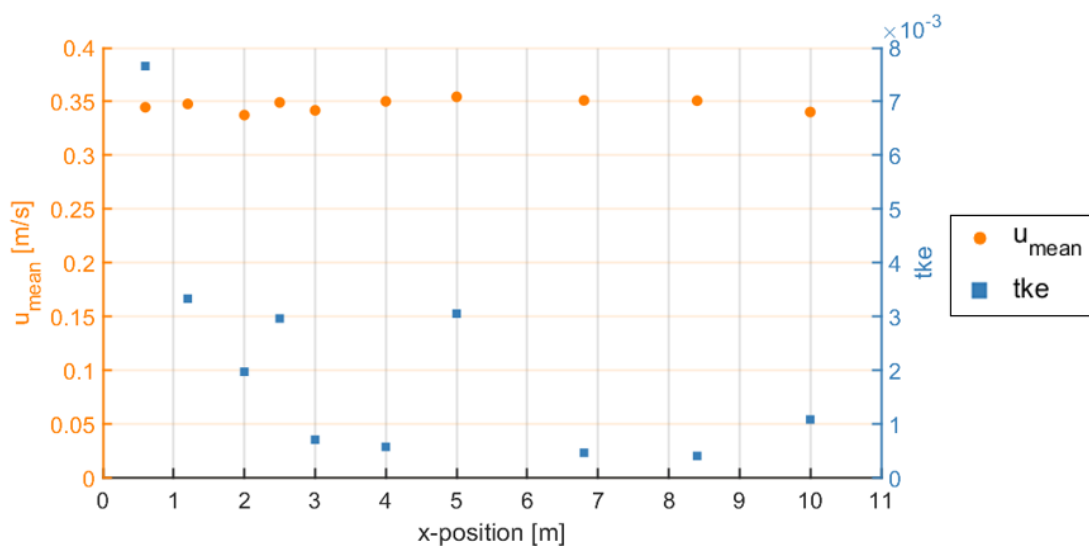
Figure 4.3: *Normalized mean velocities in the streamwise direction (orange dots) and mean normalized tke (blue squares) for downstream distances behind the grid area.*

Figure 4.3 also show the average tke for the same measurements. For the single centerline measurements, the tke are almost constant around $0.3 \cdot 10^{-3}$ while the average lateral measurements show higher tke levels. At 2.0 m the tke is $\approx 2 \cdot 10^{-3}$ and the tke has reduced to $\approx 1 \cdot 10^{-3}$ at 10.0 m downstream.

Further are the tke levels for each measurement point presented in Figure 4.4. The lateral measurements at downstream distances of 2.0 m, 2.5 m, and 5.0 m show that higher turbulence is generated by the grid's outer edge, caused by the square geometry of the grid frame. At 2.0 m and 2.5 m, lower tke levels are observed outside of the grid in the higher velocity flow shown in Figure 4.2, indicating that a more laminar-like flow is surrounding the turbulent flow. The mean TI at 2.0 m is calculated with equation 2.22 for the measurement behind the grid area and gives a TI of 10.7 %, and is defined as the TI of the incoming flow experienced by the disc setups in the turbulent flow.
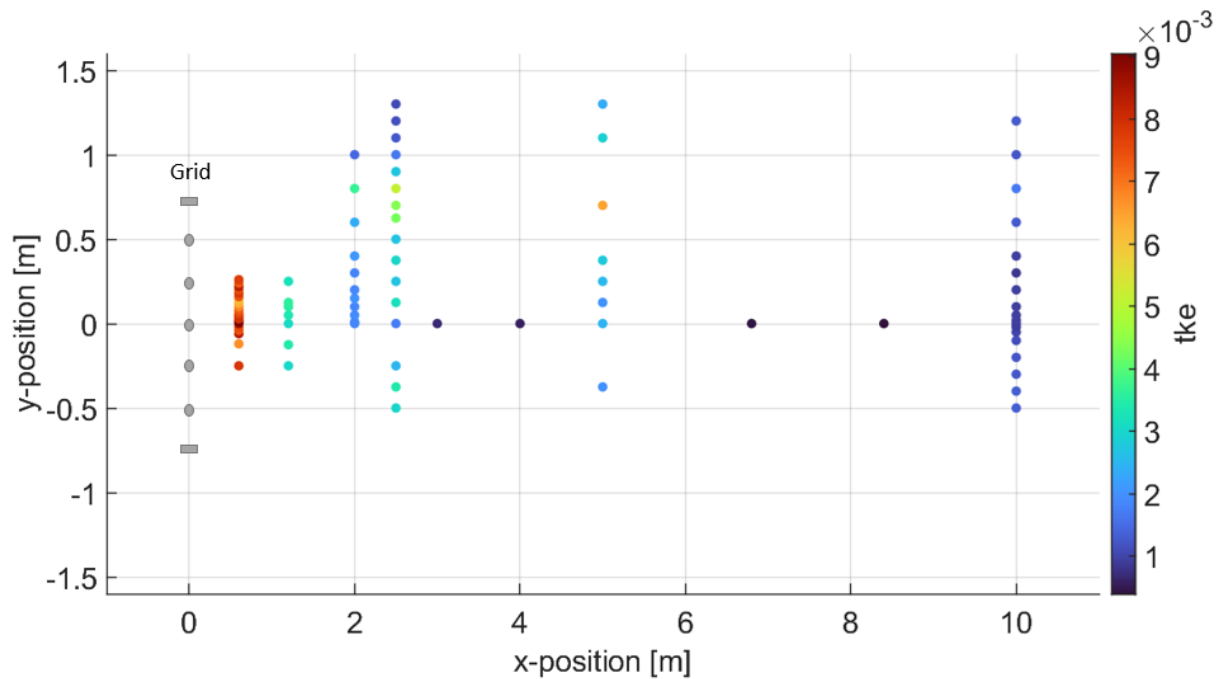
Figure 4.4: *Contour scatter plot of the tke for each measurement point.*

4.1.2 Laminar and turbulent flow

A wind turbine will operate in the ABL, where turbulence is present. However, for experimental investigations of disc wakes, laminar incoming flow is sometimes used due to equipment, simplicity, or facility limitations. Therefore, to understand the effect of turbulence on the wakes generated by SR and MR setups, turbulent inflow is investigated and compared with laminar inflow to see if similar results are obtained and that laminar inflow can be used for future experiments.

Single rotor

Although the primary objective of this thesis is to investigate MR wakes, first, an understanding of the wake of an SR in the same conditions will be investigated. In Figure 4.5 and 4.6 are the normalized velocity deficits and normalized tke of the two SR wakes in turbulent and laminar flow presented. In laminar flow is the SR_{20} used, and the SR_{70} is used in the turbulent. Henceforth will the two cases be referred to as the laminar and turbulent wake. In the near wake, at $X = 2D$, the normalized velocity deficit in the laminar wake is higher than for the turbulent wake, and it expands more than the turbulent wake. The laminar wake appear as a smooth Gaussian shape, while the turbulent wake follow a similar Gaussian curve but deviates around it. The deviations for the turbulent wake could be caused by wake effects from the nacelle of the tower described in Sec 3.1.6 but also be a cause of the turbulent flow. At $X = 4D$, the turbulent and laminar wakes' maximum normalized velocity deficits have halved from $2D$, and the turbulent wake still has a lower normalized deficit. However, in the far wake at 7D and 10D, the maximum normalized velocity deficit of the two inflow conditions is more or less similar. The effect of the laminar high-velocity flow outside the turbulence grid discussed in Sec. 4.1.1 can be observed at $7D$ and $10D$ for the turbulent wake as the normalized velocity deficit in the outer wake are negative.

The tke levels of the two wakes are presented in Figure 4.6. The laminar wake at $2D$ shows lower normalized tke levels than the turbulent wake in the near wake. The highest turbulence level in the laminar wake appears around the edge of the disc, $y/D = \pm 0.5$, which is also observed for the turbulent wake but with three additional peaks around the center. These additional peaks are believed to be caused by the nacelle. At $4D$, the normalized tke levels for both cases are alike. The laminar wake has a smoother tke curve with uniform turbulence behind the disc area and lower outside. The tke curve of the turbulent wake follows the same
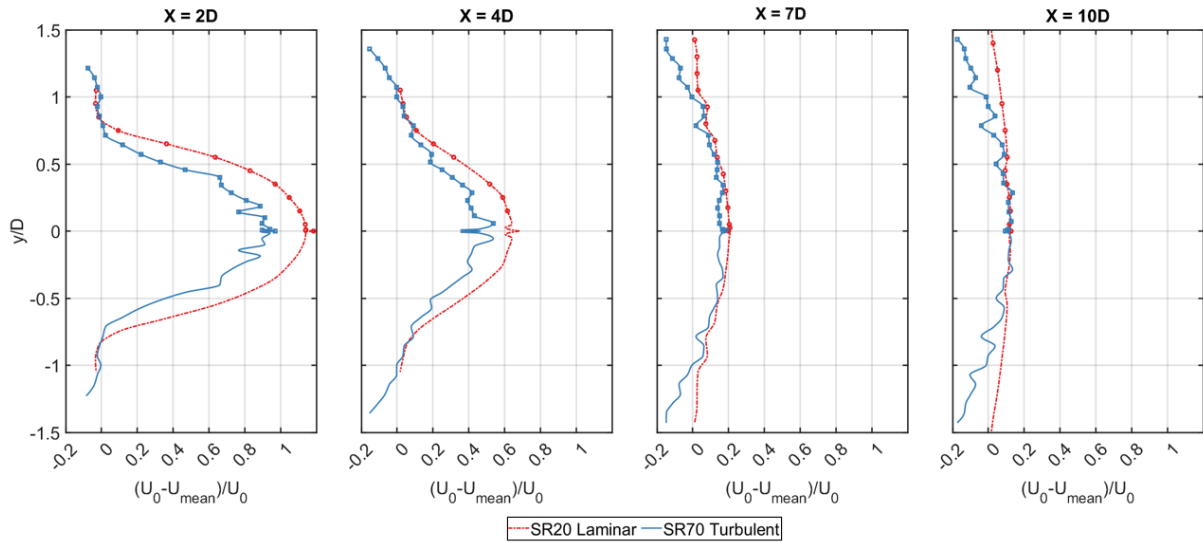
Figure 4.5: *Lateral wake profiles of the normalized velocity deficits for SR_{20} in laminar flow and SR_{70} in turbulent inflow.*

path as the laminar, but it is not as smooth and with some deviations along the path. Also, at $4D$, the tke peaks occur close to the center of the turbulent wake. Further downstream, at $7D$ and $10D$, the normalized tke levels for each inflow condition are similar but turbulent wake is a bit higher.
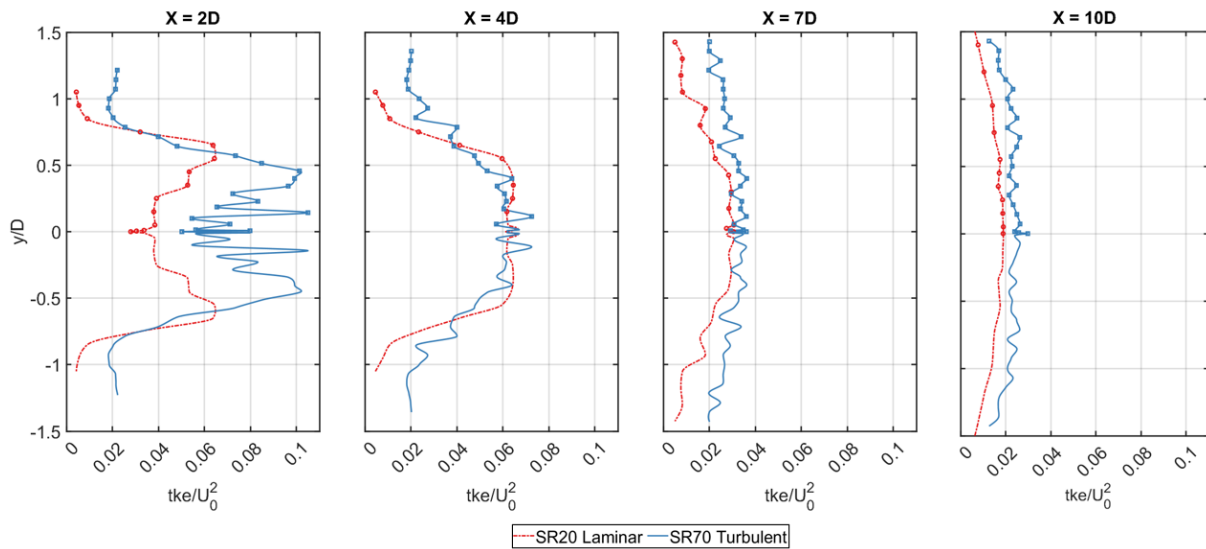
Figure 4.6: *Lateral wake profiles of the normalized turbulent kinetic energy for SR_{20} in laminar incoming flow and SR_{70} in turbulent inflow.*

Multirotor

The wake of the MR7 with $0.1d$ inter-disc spacing in turbulent and laminar incoming flow are presented in Figure 4.7 and 4.8. The normalized velocity deficits in Figure 4.7 show similarities between the two wakes. At $X = 2D$, the two conditions give a similar maximum velocity deficit at the wake center, and a wider wake expansion for the laminar wake is observed. At $X = 4D$ and $X = 7D$, the wake's expansion is more similar, but the velocity deficit of the laminar wake is lower, at least behind the MR. Also, at $X = 10D$, the laminar wake has a lower velocity deficit behind the MR and is almost fully recovered. The negative velocity deficit in the outer area of the far wake for the turbulent SR wake observed previously is also evident in the turbulent MR wake.
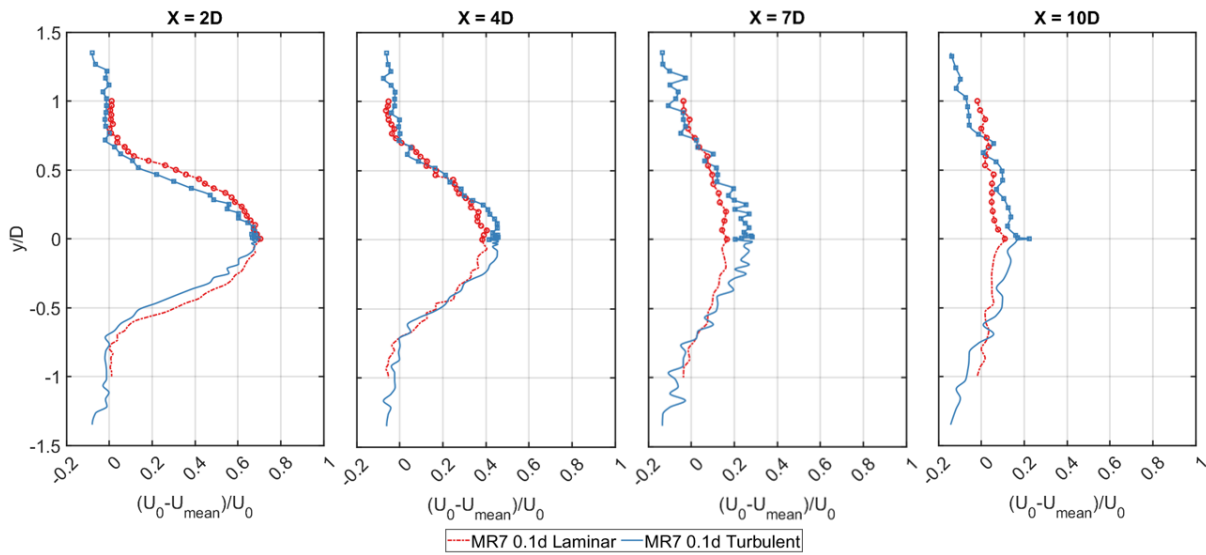
Figure 4.7: *Lateral wake profiles of the normalized velocity deficits for the MR7 in laminar and turbulent inflow.*

Comparing the normalized turbulent kinetic energy for the two conditions in Figure 4.8 at $X = 2D$, the turbulent condition has the highest turbulence. The two wake representations show similarities in the turbulence levels across the wakes, but the turbulent condition gives slightly higher values. At $10D$, at lateral position $y/D = \pm 0.8$, higher tke levels are observed caused by the grid, similar to the SR turbulent wake.

At $x = 4D$, the laminar wake measures the highest turbulence, which occurs in the middle of the wake, but the maximum tke level is the same as at $X = 2D$. The highest turbulence still occurs at the MR edge for the turbulent condition, but the turbulence level has reduced. From $y/D \approx 0.4$ and outwards, the turbulence level is almost identical between the two conditions. A lower turbulence level for the turbulent condition can also be observed at $X = 7D$. At

$X = 10D$, the turbulence level is approaching a consistent level across the wake. For the turbulent condition, the effect from the turbulence grid can be observed around $y/D = 0.7$ with a increase in the tke.
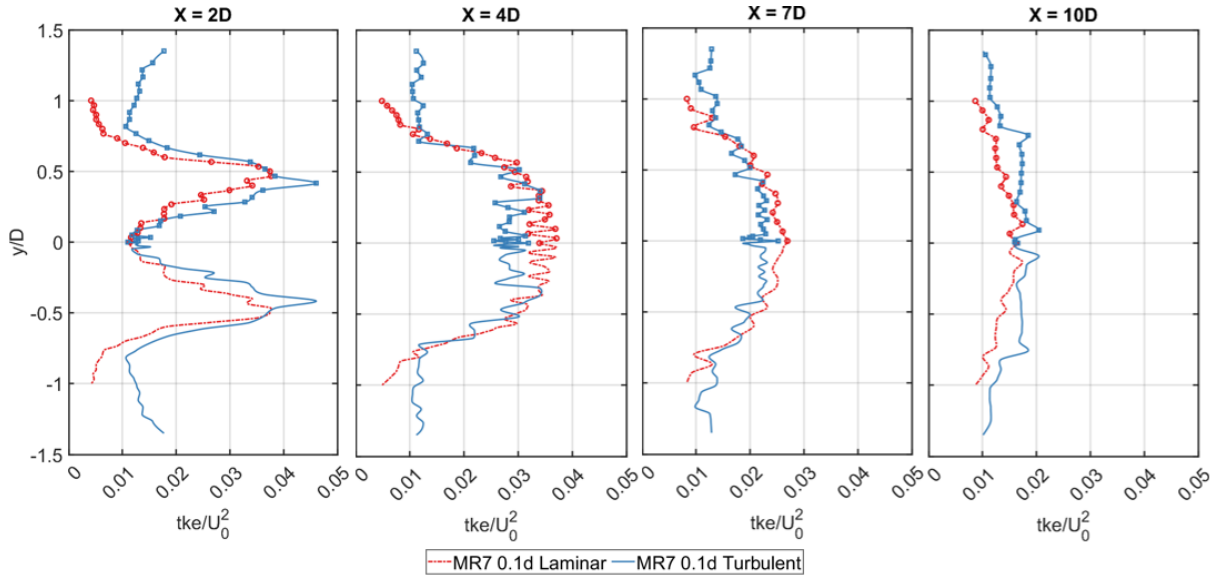
Figure 4.8: *Lateral wake profiles of the normalized turbulent kinetic energy for the MR7 in laminar and turbulent inflow.*

Centerline

In Figure 4.9, centerline measurements of the normalized velocity deficit and normalized tke are presented for the MR and SR in the two types of flow. Figure 4.9a) show that the velocity deficit for the laminar wakes is higher than the turbulent wakes for the whole range measured and that the two wake types follow the same pattern downstream. For the normalized tke in Figure 4.9b) the laminar and turbulent wakes also follow similar paths, but the initial turbulence generated in the SR wakes differs. The initial turbulence level is significantly higher for the turbulent wake than the laminar, which starts low and increases rapidly. Both SR wakes reach the maximum turbulence level around $x/D_{tot} \approx 4$. The turbulence of the MR7 wakes is similar, with the turbulent wake having a bit higher levels. The turbulence is at its highest initially and reduces to a minimum around $x/D_{tot} \approx 2.5$ before increasing to a level where it stabilizes.
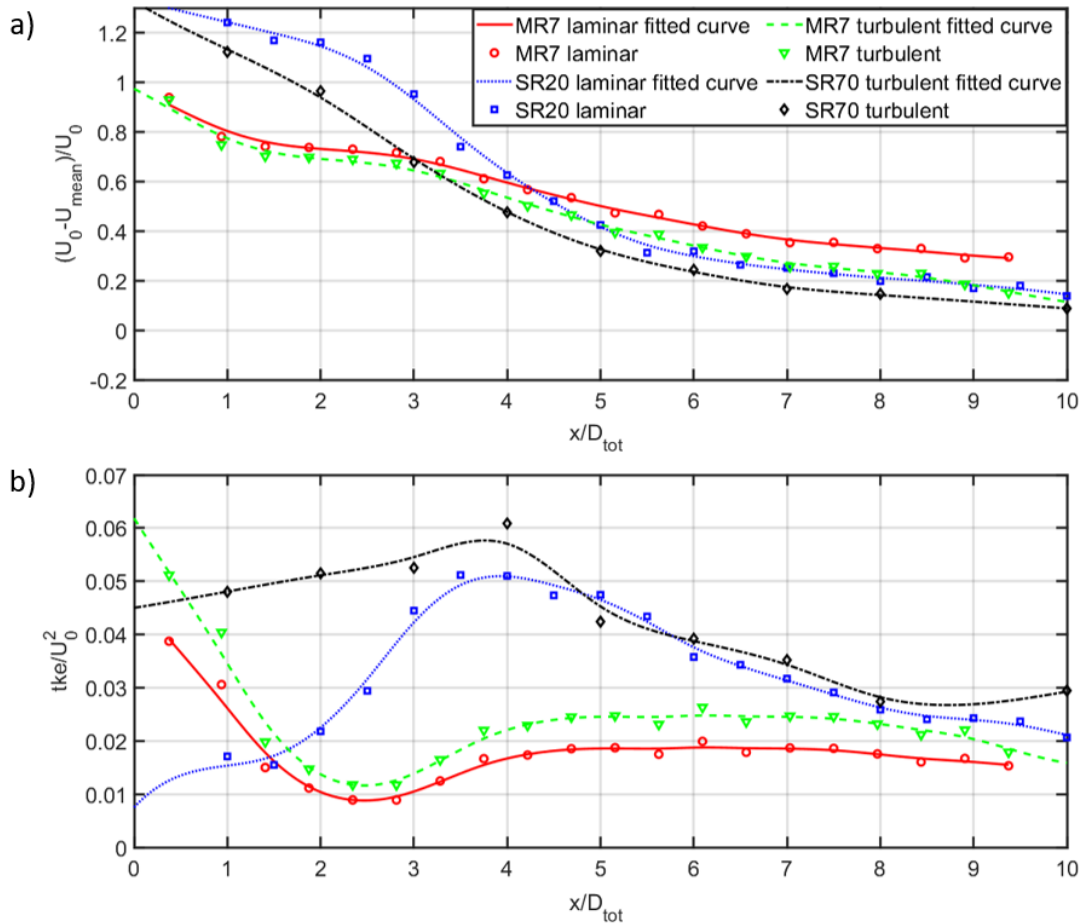
Figure 4.9: *Centerline measurements of a) normalized velocity deficit and b) normalized turbulence kinetic energy of the MR7 0.1d, SR_{20}, and SR_{70} in laminar and turbulent incoming flow.*

4.1.3   Effect of spacing in turbulent flow

In this section, lateral wake profiles of the MR7 with three different disc spacings in a turbulent incoming flow will be presented, as well as the SR_{70} for comparison. In wind farm situations, the spacing between SR turbines is known to have an impact on the downstream wakes [12, 18, 25], therefore is it believed that this effect from the spacing between the discs in MRS also affects the MR's wake development. The effect of rotor spacing is investigated with rotor spacings; $0.0d$, $0.1d$, and $0.4d$. Lateral wake profiles of the normalized velocity deficits are presented in Figure 4.10 and the normalized tke in Figure 4.11.

The normalized velocity deficit in Figure 4.10 show clear differences between the configurations at $X = 2D$. Firstly, it can be observed that an increase in spacing leads to a lower velocity deficit and a narrower wake in the near wake. With no spacing, $0.0d$, the maximum velocity deficit for MR7 and SR_{70} are approximately equal but the SR_{70} wake is a bit wider. In the

downstream range $2D - 10D$ no significant differences between the SR_{70} and MR7 $0.0d$ are observed.
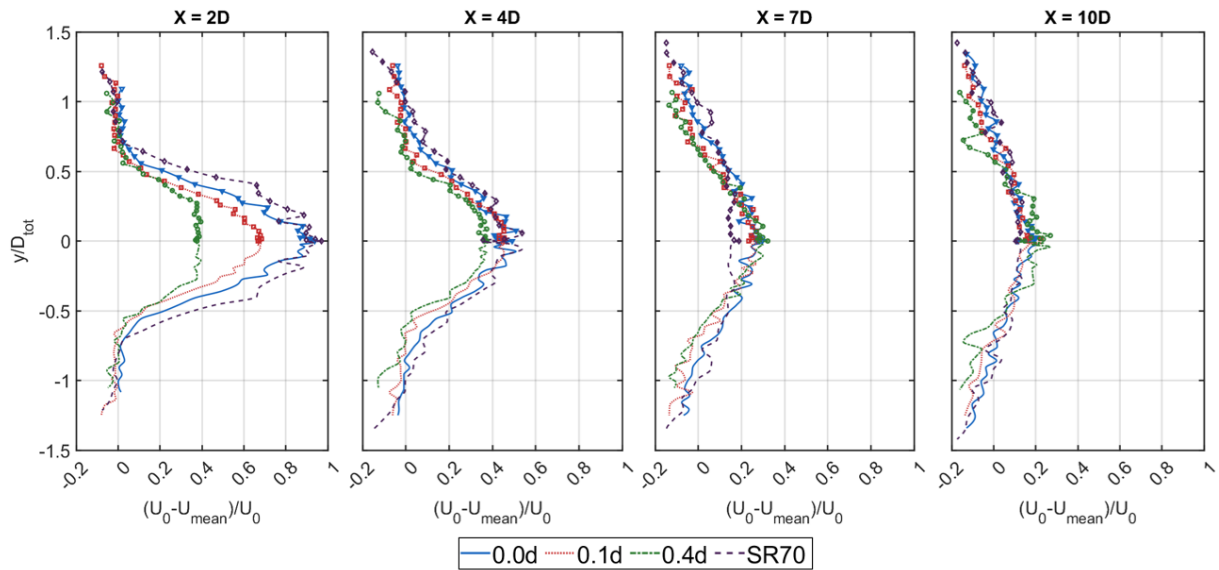
Figure 4.10: *Lateral wake profiles of the normalized velocity deficit of the MR7 with three different rotor spacing; 0.0d, 0.1d, and 0.4d, and the SR_{70}.*

At the downstream distance of $4D$, the differences in velocity deficit between the three MR7s have reduced. The mean velocity deficit of the wake with $0.1d$ spacing is slightly lower than with $0.0d$ spacing and the $0.4d$ spacing has the lowest deficit. This changes in the far wake region $7D$ and $10D$. At $7D$, all three MR7s have velocity deficits around the same level. At *10D* the velocity deficit around the center of the $0.4d$ wake is slightly higher than the $0.0d$ and $0.1d$. The MR7s with $0.0d$ and $0.1d$ spacing has the same velocity deficit levels as the SR_{70} at these downstream distances.

Table 4.1 show values for the four lateral profiles fitted with the polynomial curve fitting. At $X/D = 2$ the maximum velocity deficit is easily seen to decrease with increased disc spacing. At $X/D = 4$ and $X/D = 7$ the maximum velocity deficits of the $0.0d$ and $0.1d$ are similar, while the MR7 $0.4d$ still has a bit lower deficit. At $X/D = 10$ the wakes of the $0.0d$ and $0.1d$ has recovered more than the $0.4d$. The SR do have the highest wake recovery in the measured range from 8.85 % at $2D$ to 88.25 % at $10D$.

Table 4.1: *Data for the lateral wake profiles based on a 10th-degree polynomial fit for the MR7 with the three different spacing configurations and the SR$_{70}$ in a turbulent flow.*

Disc Config.	X/D	Max. normalized velocity deficit [-]	Wake recovery percentage	Wake width $\frac{}{D_{tot}}$
MR7 0.0d	2	0.89	11.05 %	0.72
	4	0.45	54.81 %	0.90
	7	0.26	74.36 %	1.10
	10	0.17	82.59 %	0.78
MR7 0.1d	2	0.68	31.91 %	0.69
	4	0.46	54.25 %	0.76
	7	0.26	73.96 %	0.85
	10	0.16	83.78 %	0.85
MR7 0.4d	2	0.39	61.28 %	0.86
	4	0.37	63.27 %	0.77
	7	0.29	71.49 %	0.75
	10	0.21	79.37 %	0.78
SR$_{70}$	2	0.91	8.85 %	0.93
	4	0.45	54.51 %	1.02
	7	0.16	83.74 %	1.44
	10	0.12	88.25 %	1.21

The normalized tke for the wakes, presented in Figure 4.11, gives another aspect of the rotor spacing's effect on the wake. Firstly, comparing the SR$_{70}$ with the MR7 0.0d indicates that an MR creates less turbulence in the wake in the measured streamwise range, $2D - 10D$. At $2D$, the turbulence level for the SR$_{70}$ is substantially higher than the MR7 0.0d but at $10D$ the tke is almost reduced to MR levels.
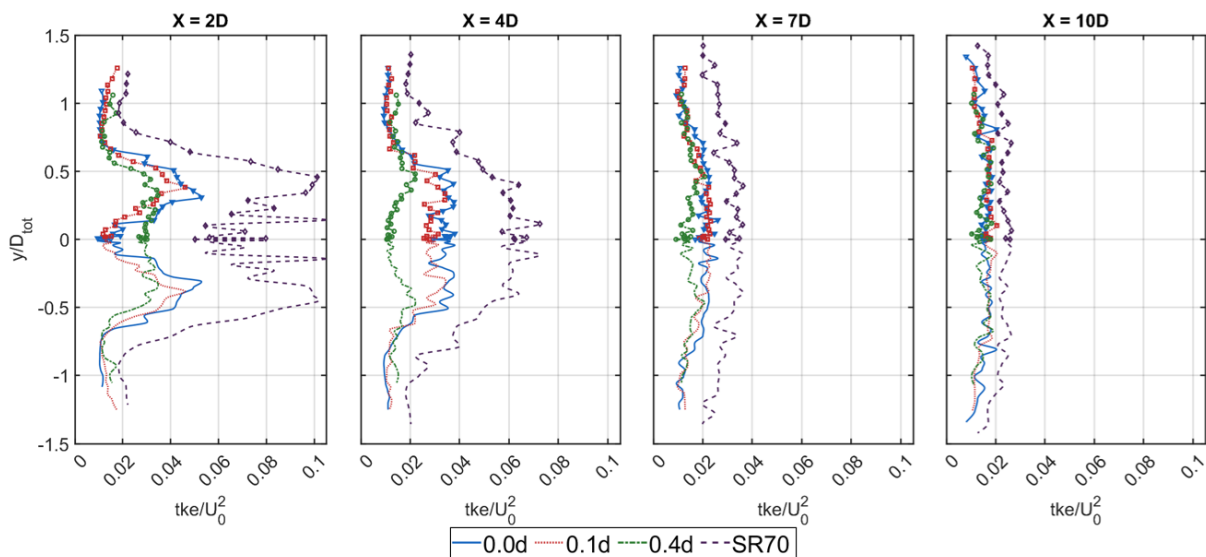

Figure 4.11: *Lateral wake profiles of the normalized turbulent kinetic energy for the MR7 with three different rotor spacing; 0.0d, 0.1d, and 0.4d, and the SR$_{70}$.*

At $X = 2D$, MR7 $0.0d$ and $0.1d$ has their highest tke levels behind the side-discs and low turbulence level behind the center disc. The $0.0d$ has the highest turbulence peaks. The MR7 $0.4d$ has uniform turbulence level behind the MR area. Downstream at $X = 4D$ the $0.0d$ and $0.1d$ configurations have archived uniform tke levels behind the MR area, where the $0.0d$ have slightly higher values. The $0.4d$ configuration has a tke level below 0.02, and is almost uniformly distributed, only with a slight increase at $y/D_{tot} = \pm0.5$. The $0.0d$ and $0.1d$ MRs' tke levels are further reduced at $X = 7D$ but the $0.4d$ MR's tke level is still lower. At $X = 10$ all three MR spacing are measured to have similar and uniform turbulence levels.

4.1.4   Number of discs

This section investigates the effect the number of rotors in an MRS has on wake development. Three MR wakes have been measured with a laminar incoming flow; MR4, MR7, and MR19, all with disc spacing $0.1d$. The normalized velocity deficit at streamwise distances of 2D, 4D, 7D, and 10D plotted in Figure 4.12 and data from the polynomial fits of the plotted measurements are given in Table 4.2 for the cases. The wakes are compared with the wake of the SR_{20}. At 2D, the velocity deficit of all MRs is significantly lower than the SR. The velocity deficits for the MRs are almost similar, but the MR19 shows the lowest deficit. At $X=4D$ the MR7 gives a lower deficit than the MR4, and the SR still shows the highest deficit. These wake profiles indicate that a higher number of rotors leads to less velocity deficit. However, at $X=7D$ the SR show the lowest velocity deficit, the MR4 the second-lowest, the MR7 the third lowest, and MR19 has the highest. Furthest downstream at $10D$, the MR4 and SR are almost similar, while the MR7 and MR19 continue to have a higher deficit.

Note that the MR4 wake is measured in the center in the gap between the discs where high-velocity jets are found. These high-velocity jets have most likely contributed to a lower velocity deficit and higher turbulence in the near wake. At $X=4D$ does it occur that one uniform wake has been formed, and this effect is no longer significant. For the MR4 and SR at $X=7D$ and $X=10D$, the wakes appear more mixed and evenly distributed than the MR7 and MR19, which still show a high deficit area between $y/D_{tot} = \pm0.5$. Another difference between the disc configurations is the wake widths. The width of the MR4 and SR are relatively similar and notably wider than the MR7 and MR19 wakes. The MR7 and MR19 have relatively similar wake widths.
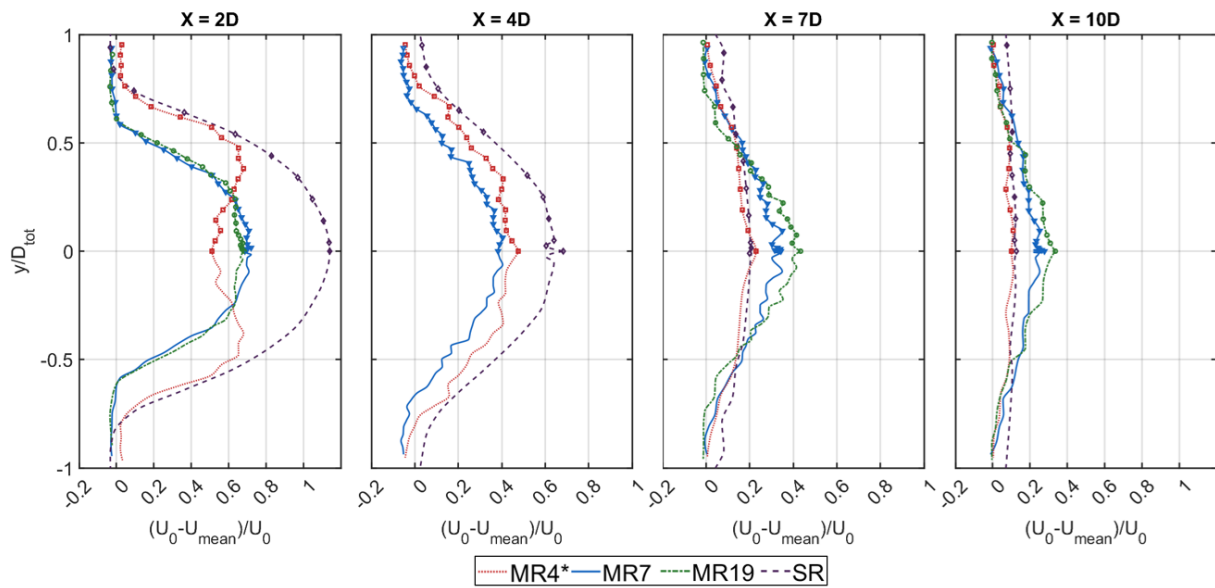
Figure 4.12: *Lateral profiles of the normalized velocity deficit for MR4, MR7, and MR19 with 0.1d spacing, and for the SR$_{20}$.*

Table 4.2 shows that the wake recovery at *X=10D* for the MR4 and SR are 89.29% and 87.79 %, respectively, and have almost fully recovered to the initial velocity. The MR7 has only recovered 75.19 %, and the MR19 has recovered as little as 69.22 %.

Table 4.2: *Data for the lateral wake profiles based on a 10th-degree polynomial fit for the four disc configurations MR4, MR7, MR19, and SR$_{20}$.*

Disc Config.	X/D	Max. normalized velocity deficit [-]	Wake recovery percentage	Wake width D_{tot}
MR4	2	0.67	32.73 %	1.25
	4	0.44	56.11 %	1.11
	7	0.26	74.39 %	1.34
	10	0.11	89.29 %	1.34
MR7	2	0.70	30.05 %	0.84
	4	0.44	55.83 %	0.94
	7	0.32	67.55 %	0.97
	10	0.25	75.19 %	1.13
MR19	2	0.66	34.28 %	0.86
	4	-	-	-
	7	0.41	58.77 %	0.78
	10	0.31	69.22 %	0.84
SR$_{20}$	2	1.14	-14.35 %	1.14
	4	0.64	36.42 %	1.10
	7	0.26	74.47 %	1.71
	10	0.12	87.79 %	2.24

In Figure 4.13 the lateral normalized tke profiles for the four wakes are presented. The turbulence level for the MR7 and MR19 are low compared to the MR4 and SR at *2D*. Comparing the MRs at *2D* show that an increase in the number of discs reduces the turbulence level. The MR4 measurements are likely affected by the space between the discs creating the highest tke level of the four wakes. The space creates higher turbulence due to the shear forces between the high-velocity flow and discs. At *X=4D* this effect has diminished due to the wake mixing. The MR4s tke level has reduced to the level of the MR7, while the SR has the highest turbulence levels, almost twice the level of the MRs. In the far wake at *X=7D* and *X=10D*, the MR7 and MR19 show similar turbulence levels, and the MR4 and SR show similar levels, which are a bit higher than the MR7 and MR19. The difference between them is reduced from *7D* to *10D* where all four wakes show similar tke levels.
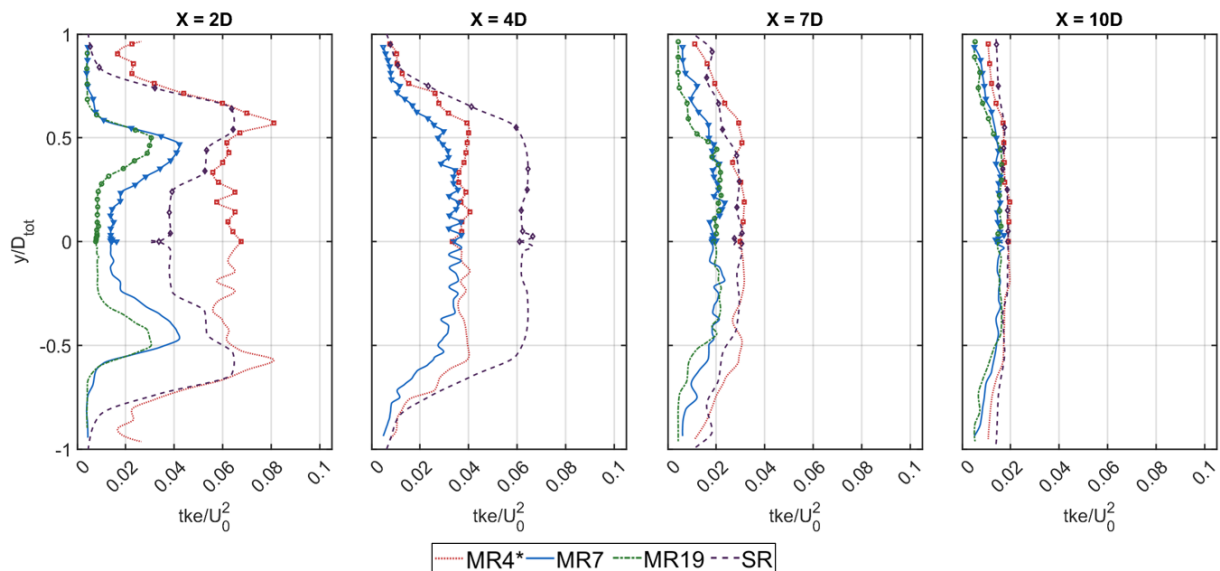
Figure 4.13: *Lateral profiles of the normalized turbulence kinetic energy for MR4, MR7, and MR19 with 0.1d spacing, and for the SR$_{20}$.*

Centerline measurements of the tke for the four configurations are shown in Figure 4.14. The centerline measurements show that the turbulence fluctuates for the MR4 at $x/D_{tot} \leq 3$ due to the mentioned shear forces before the wake mix and the tke level is reduced stably. For the SR is the turbulence level low at $x/D_{tot} = 1$ and gradually increasing in the near wake. This increase is due to the wake mixing and is clearly shown for the SR. The centerline measurements also show the same far wake picture as the lateral wake profiles regarding the tke level. The initial tke level of the MR7 and MR19 follow a similar path with the MR19 having a bit lower turbulence level than the MR7. For these two MR setups, the turbulence is high initially before rapidly decreasing to the lowest value, before the turbulence starts to increase

and stabilizes downstream.
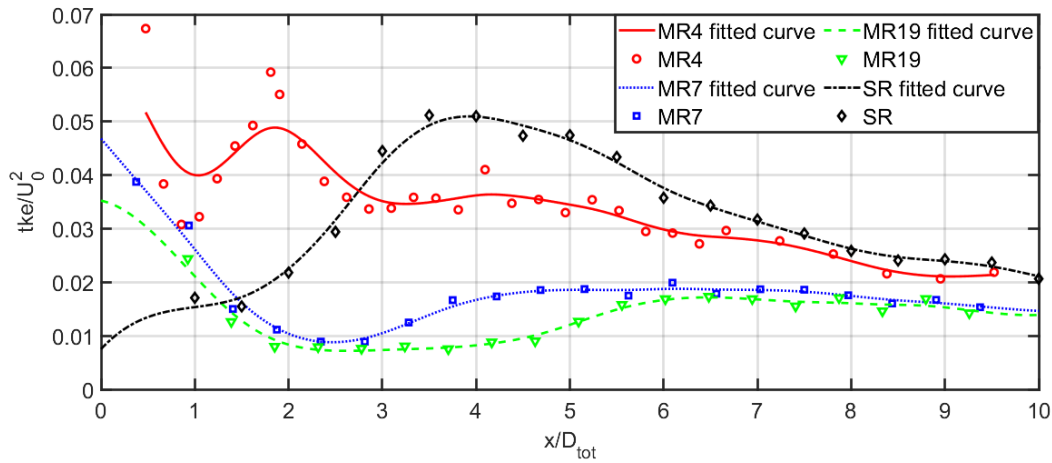
Figure 4.14: *Centerline measurements of normalized turbulence kinetic energy for the MR4, MR7, MR19, and SR$_{20}$.*

4.1.5 Wake steering

In this section, measurement results from three types of wake steering, or types of yaw configurations, of the MR7 with spacing $0.1d$ will be presented. The disc spacing is the spacing prior to the disc yaw being added. The three types of yaw are described in detail in Chapter 3: tower yaw, individual disc yaw, and combined yaw. In addition, the normal, zero yaw condition, is presented as a reference.

The normalized velocity deficits are presented in Figure 4.15. The maximum velocity deficits for all four configurations are approximately the same and located around $y/D = 0$. It is expected that the yaw will lead to a deflection of the wake, and this is observed for the individual disc yaw and tower yaw. These two yaw types result in the same deflection towards the positive side of the y-axis and a similar velocity deficit. However, no measurements of the tower yaw were measured further out than $y/D = +0.5$, so it is unclear how the wake developed in this region. However, as the wakes appear similar on the negative side of the y-axis, it can be assumed to be similar on the positive side as well. The wake of the zero yaw configuration is narrower than these two yawed configurations. The configuration with both the discs and tower yawed, making the discs perpendicular to the incoming flow, creates a wider wake than the zero yaw condition and can appear almost symmetrical over the positive and negative y-axis.
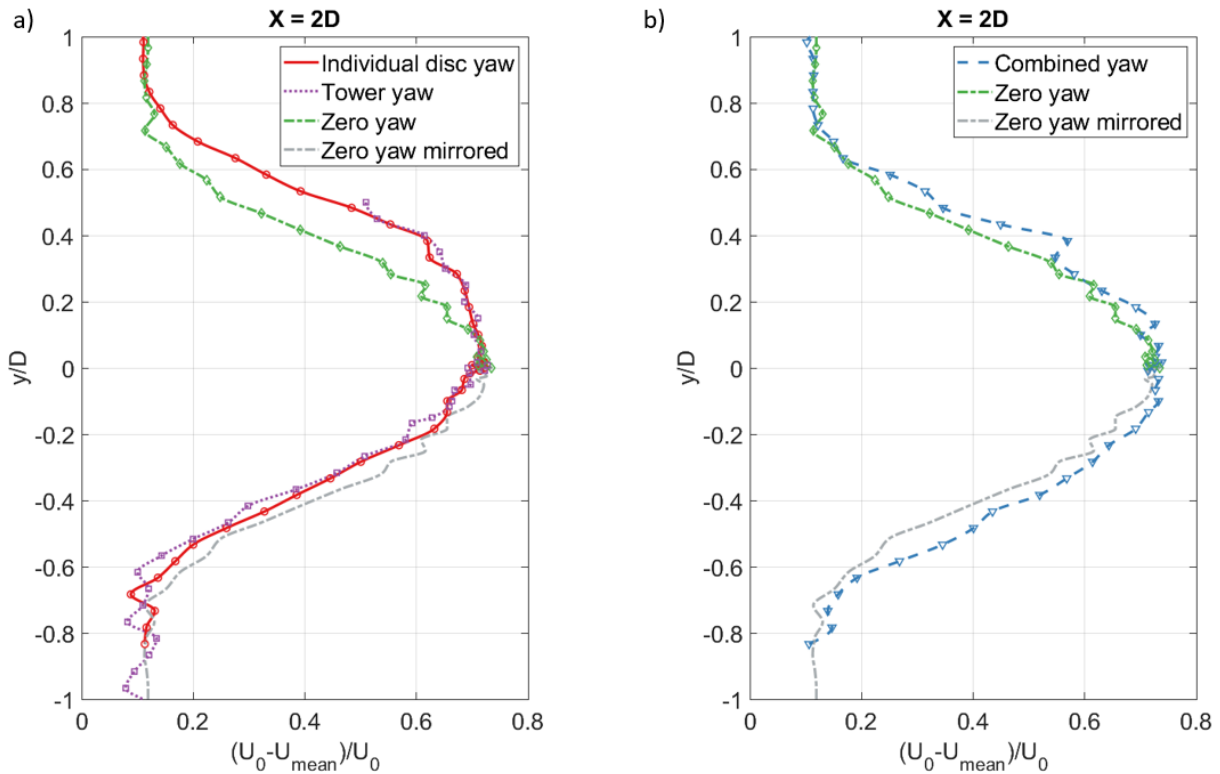
Figure 4.15: *Lateral profiles of normalized velocity deficit profiles of the MR7 at X = 2D with; a) individual disc yaw, tower yaw, and zero yaw, and; b) combined yaw and zero yaw.*

The lateral normalized tke profiles presented in Figure 4.16 show that the yaw leads to higher tke levels on one side and lower on the other. Firstly, regarding the tke levels, the individual disc yaw and the tower yaw configuration do not follow each other as for the velocity deficit in Figure 4.15. Most notably are the differences at the peaks. The turbulence level at the positive y-axis for the individual disc configuration is lower than at the negative and appears just above $y/D = 0.6$. On the negative side, the peak appears around $y/D = -0.3$. For the tower yaw configuration, the peaks appear at both sides around $y/D = \pm 0.4$, and the magnitude is not that different. Compared with the tke peaks for the zero yaw configuration, the tower yaw gives lower peak tke levels for both peaks. The individual disc and tower yaw configuration also give peaks around the same location $y/D = \pm 0.5$. However, the magnitude is quite different, with the positive side being around the magnitude of the individual yaw configuration and the negative side the highest peak of them all.
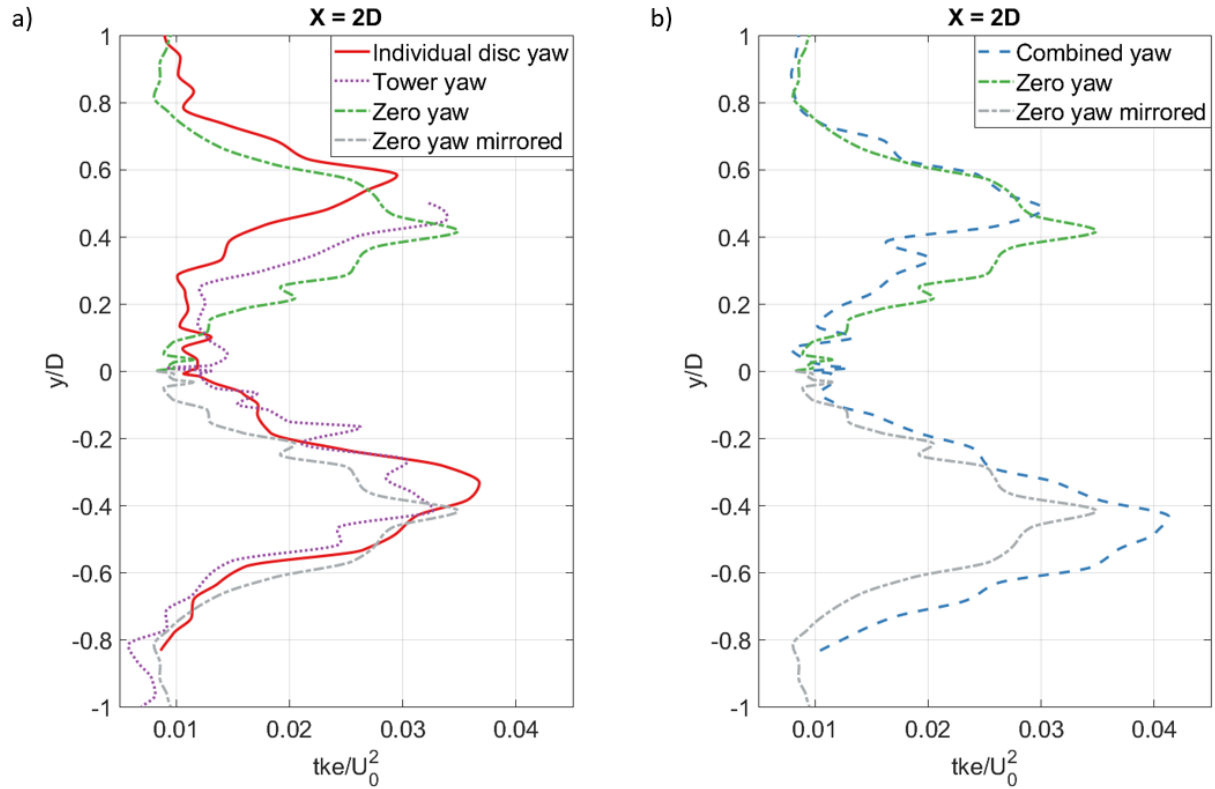
Figure 4.16: *Lateral profiles of normalized turbulence kinetic energy of the MR7 at X = 2D with; a) individual disc yaw, tower yaw, and zero yaw, and; b) combined yaw and zero yaw.*

4.1.6 Effect of Wind Catching Systems frame

To see how much a second frame structure would affect the wake behind a MR the MR7 has been compared with the WC7 in Figure 4.17 and 4.18, both with spacing 0.1d. At first glans the differences between the two are minuscule. However, the WC7 do have slightly higher velocity deficit at 2D and 4D around *y/D = 0*, observed in Figure 4.17. At 10D, no significant difference can be observed.

Also, for the tke level is the difference most notable in the near wake at *X=2D*. The MR7 has a higher maximum turbulence at $y/D = \pm0.5$, and also the lowest turbulence around $y/D = 0$. In the far wake at *X=7D* and *X=10D* no distinct difference are noted.
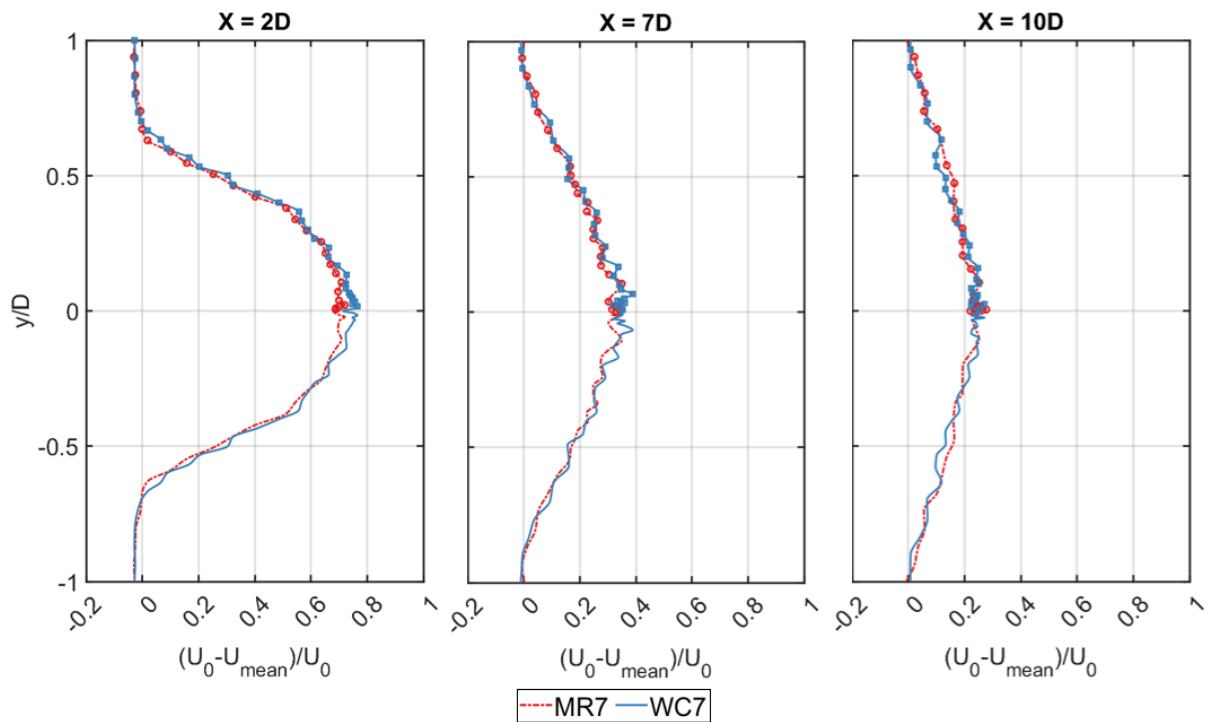
Figure 4.17: *Lateral profiles of the normalized velocity deficit for the MR7 and WC7 with 0.1d spacing.*
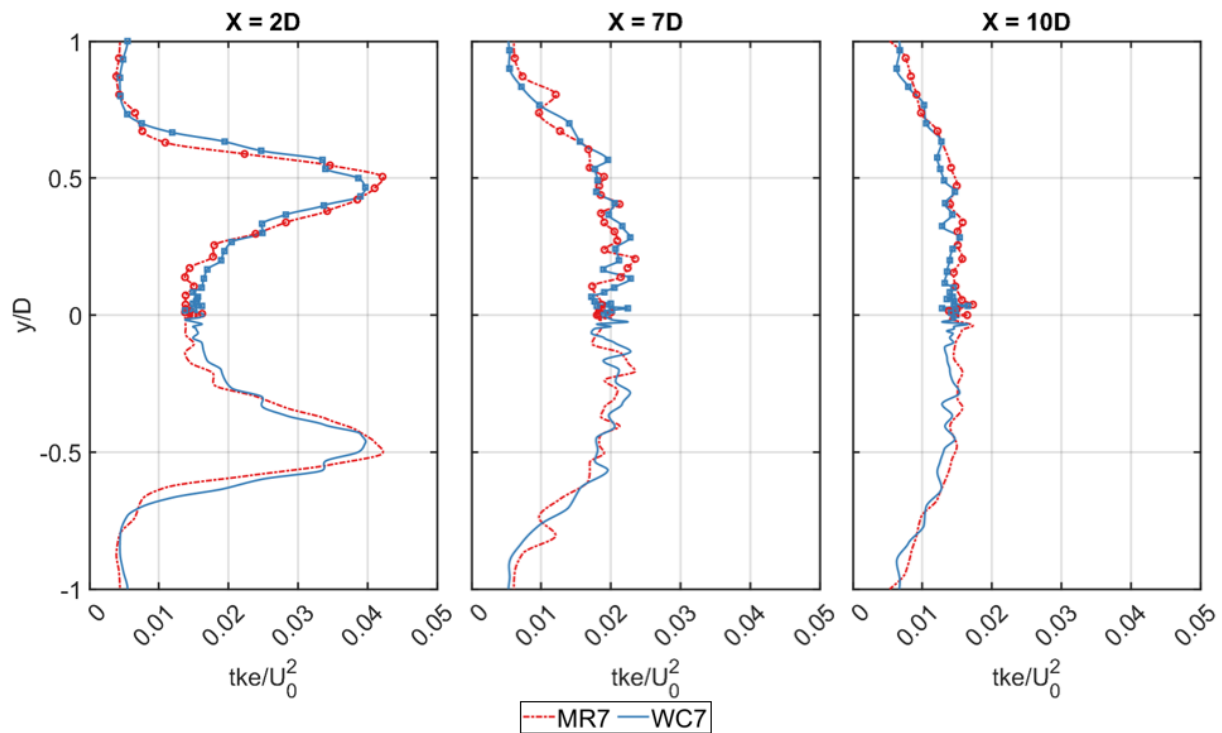
Figure 4.18: *Lateral profiles of the normalized turbulence kinetic energy for MR7 and WC7 with 0.1d spacing.*

4.2 Discussion

In Sec. 4.2 will the results presented in Sec 4.1 be further discussed and put into context with previous experimental and computational results. The results for the MR and SR wakes are presented with normalized values without denomination. The way wake measurements are best presented is a discussion on its own. Especially the definition of the downstream distances. The lateral wake profiles have been measured at downstream distances defined by D, the diameter of the discs, while the actual diameter of the MRs with different spacing are D_{tot}. The influence of this difference will be broth up later in this section to shed light on the difference that could lead to when comparing MR wakes.

4.2.1 Turbulence grid

The characterization of the wake generated by the turbulence grid gave an essential under-standing of the flow the disc setups experience. The results also showed key phenomenons related to wake development with wake mixing, recovery, and blockage effect. At 2.0 m, the visible jet streams behind the grid had dissolved, and the wake had a uniform velocity and turbulence level behind the grid area.

For the downstream location of 2.0 m two fundamental values were defined; the average velocity of 0.337 m/s and average TI of 10.7 %. Especially the definition of the velocity will affect later results when the disc setups in laminar and turbulent flow are compared, as this velocity normalizes the turbulent measurements. Interestingly the averaged values for the velocity and tke at 2.0 m are shown to vary from the measurements at 2.5 m which generally are more similar to the other measurements both up and downstream (see Figure 4.3). If the defined velocity from 2.0 m is correct is therefore uncertain. Generally, more time might have been used to investigate the downstream distance around 2.0 m.

A higher velocity, less turbulent flow is observed outside the grid area. This high velocity flow are highest at 2.0 m and have reduced at 10.0 m, while the velocity behind the grid area has increased during this distance, showing signs of the wake mix and recover. It is troublesome that the grid does not cover the whole width; however, the disc wake measurements show signs of this having a low effect on the disc setup wake developments. The wake created by the discs is stronger than the grid, and the recovery of the grid wake is almost insignificant. The SRs in laminar and turbulent flow are good examples (see Figure 4.5), where the two

wakes show similarities between $y/D = \pm1$ at $X = 7D$; however, further outwards, the effect of the higher velocity is evident as the velocity deficit is below zero for the turbulent wake. At $X = 10D$, the wakes deviate closer to the wake center at $y/D = \pm0.5$, indicating that the higher laminar flow most likely influences the far wake outside the disc setups edge with the higher velocity mixing further and further toward the wake center. The outside velocity are therefore believed to only affect the outer edge of the wake in the far wake. Figure 4.2 emphasizes this point as the center velocities at 10.0 m are similar to the velocities at 2.0 m for the grid measurements, while the outer measurements are not.

The grid characterization was conducted at 50 cm depth, while the center of the disc setups was located at 100 cm. This difference could lead to a higher velocity mixing for the wake due to high-velocity flow passing under the grid. The measurement depth of 50 cm was chosen at an early stage of this thesis and measurement campaign, and at that point, the ADV was not configured to measure any deeper. Løken et al. [43] did depth measurements of the streamwise velocity with an Acoustic Doppler Current Profiler (ADCP) at 2.5 m behind the grid at 0.4 m/s. These depth measurements did not show any signs of an increase in the velocity at a depth of 80 cm and that 50 cm was deep enough for the measurements not to be influenced by the free-water surface. However, there is reason to believe that in the far wake the high-velocity flow passing under the grid mix into the wake. For the grid geometry, there is no difference between 50 cm and 100 cm as the grid geometry are similar; however, how the high velocity from underneath the grid might affect the wake at these depths is uncertain and could play a significant role in the results.

With a TI of 10.7 %, the turbulence level is a bit higher than the turbulence level in the computational models by Ghaisas et al. [13], and Bastankhah and Abkar [9] of 8.0 % and 6.7 %, respectively. These are turbulence levels typical to find in the ABL.

4.2.2   Effect of turbulence

Looking at the SRs and MR7 in the two different inflow conditions, the first observation is the different reactions to the presence of turbulence. The normalized velocity deficit of the SR is significantly lower when turbulence is present in the incoming flow at $2D$ and $4D$ (see Figure 4.5). At the same time, the deficit of the MR7 is barely different. The lower velocity deficit is likely due to a faster initial wake recovery in a turbulent flow for the SR as a higher

turbulence level leads to higher mixing between the wake and the surrounding flow. In the laminar inflow, the vortices created by the disc needs time before they start to dissolve and transporting the surrounding flow into the wake. At $7D$ the vortices behind both SRs are more similar and contribute similarly to the wake recovery meaning the inflow turbulence has its biggest effect in the near wake. The tke levels (see Figure 4.6) show that the turbulence level for the turbulent wake is high both in the wake center and around the disc edge, while the laminar wake has a lower turbulence level at wake center than at the disc edge. In the far wake, the turbulence level for both wakes are evenly spread and with similar normalized tke levels supporting the statement that the wake thereby recovers similarly.

The different reactions the SRs and MR7 have regarding the velocity deficit is due to the disc spacing in the MR7, which enables the MR wake with more available high-velocity flow through the spacing. The only higher velocity can come from outside the wake for the SRs, while the MR7 has high-velocity jets passing through the space in-between the discs. Therefore, is the mixing effect caused by the turbulent inflow not that significant as it was for the SRs. The strongest vortices for the MR7 is generated at the MR edge, and the turbulence is lower towards the center, which is similar for both laminar and turbulent inflow. Downstream, the velocity deficit is a bit lower for the laminar wake than the turbulent wake, most likely caused by the normalized tke level being a bit higher, leading to better mixing.

The centerline measurements for normalized velocity deficit clearly show how the MR7s' velocity are closer to each other than the SR values in the near wake (see Figure 4.9a). The turbulent SR wake starts recovering rapidly already from $x/D_{tot} = 1$, while the laminar SR wake archive the same recovery rate after $x/D_{tot} = 2.5$. The MR7 wakes are closest initially in the wake and start separating from $x/D_{tot} = 4$. The SR centerline curves follow each other, and the MR7 centerline curves follow each other. The laminar wakes show the highest velocity deficit in the far wake for both the SR and MR7. The same can be seen for the normalized tke centerline curves (see Figure 4.9b). For the SR increases the tke until a downstream distance of $x/D_{tot} = 4$ before reducing. It is evident that at the centerline is the initially normalized tke significantly higher for the turbulent wake than the laminar, emphasizing the reason for the lower velocity deficit at $2D$. The MR7 wakes both start with a high turbulence level at the center, which reduces until reaching the downstream distance of $x/D_{tot} = 2.5$, where the turbulence slightly increases before stabilizing. The normalized tke levels for the turbulent wakes are a bit higher than the laminar counterpart.

The measured normalized velocity deficit profiles for the MR7 with different spacing in turbulent flow (see Figure 4.10) are compared with the same profiles measured by Jørs and Mjåtveit [41] in laminar flow. The comparison shows similar normalized velocity deficits for different disc spacings for all four downstream distances. For the normalized tke levels, the only difference is a slightly higher normalized tke at $X = 10D$. This comparison backs up the similarities between an MR in a laminar and turbulent flow and that it is independent of the spacing. Summarized, experimental wake investigations of MRS show that laminar incoming flow gives similar normalized velocity deficits as with turbulence present. In contrast, the incoming flow condition affects the SR wakes more.

4.2.3   Effect of multirotor disc spacing

In the design of an MR, the effect from rotor spacing is a parameter that might lead to positive MR effects for the energy production [9, 14]. Bastankhah et al. [9] investigated three spacings of $0.0d$, $0.1d$, and $0.25d$. Their computational model showed no difference in the far wake but indicated that the velocity recovered initially faster with larger spacing for the rotor-averaged velocity. The LES showed no difference in the MR4s power production for the different rotor spacings. The measurements conducted used the same spacing, but with $0.4d$ instead of $0.25d$, to investigate if this led more (see Figure 4.10). The turbulent incoming flow measurements gave similar results as the computational models [9]. Comparing the measurements with the same measurements in laminar flow conducted by Jørs and Mjåtveit [41] shows no significant difference.

The measurements (see Figure 4.10 and 4.11) show that an increasing disc spacing leads to lower velocity deficit and lower turbulence level in the near wake. The velocity deficit is higher as more high-velocity flow is present due to the gap between the discs. However, as the wakes move downstream, the wakes with less disc spacing recover faster, and at $10D$ downstream, the velocity deficit is similar for all cases, with the $0.4d$ being the highest.

The downstream distance of the lateral wake profiles is defined by D. As the spacing increase, so does the total diameter, D_{tot}. If the wakes are compared with the same downstream distance D or a downstream distance dependent on the setups D_{tot} creates two different pictures. The difference in downstream distance for these two methods for the MR7 $0.4d$ is very significantly affected by this. In Figure 4.19, 4.20, and 4.21, lateral wake measurements

at $4D$, $7D$, and $10D$ conducted by Jørs and Mjåtveit [41], and at -0.4D, 0.4D, 1D, 1.4D, 2D, and 3D measured together with Koi [42], are combined in an interpolated contour plot and the downstream distances are defined with D_{tot}. These results show that when comparing the disc setups concerning each setup's total diameter, the 0.4d spacing has the best wake recovery.

The higher velocity jets are present for all three distances, but with increased spacing, the jets last longer into the wake downstream before they dissolve. For the 0.0d wake (Figure 4.19), a higher velocity field is present between the three separated wakes, even though there is no spacing between the discs, and is most likely due to the triangular spaces in each quadrant corner for the center disc. High-velocity jets are formed through these spaces and expand downwards towards the horizontal center leading to the observed higher velocity field.

The 0.1d wake (Figure 4.20) has narrower, higher velocity jets than the 0.0d. In the far wake, the 0.1d shows lower velocity than the 0.0d, and the 0.0d appear more uniform and more recovered. With spacing 0.4d the higher velocity jet is wider and starts dissolving later. In the far wake the 0.4d has recovered the most around 7.9D_{tot} compared with the 0.0d and 0.1d. For all three spacings are the generation of three separate wakes observed, and these mixes and recover, forming one uniform wake, confirming previous findings [9, 11]. All MR7 setups form the uniform wake around 3D_{tot}. However, the results obtained from the measurements show that the wake velocity is affected by the disc spacing. A slight wake expansion is visible in the far wake and is more evident for the shorter disc spacing.
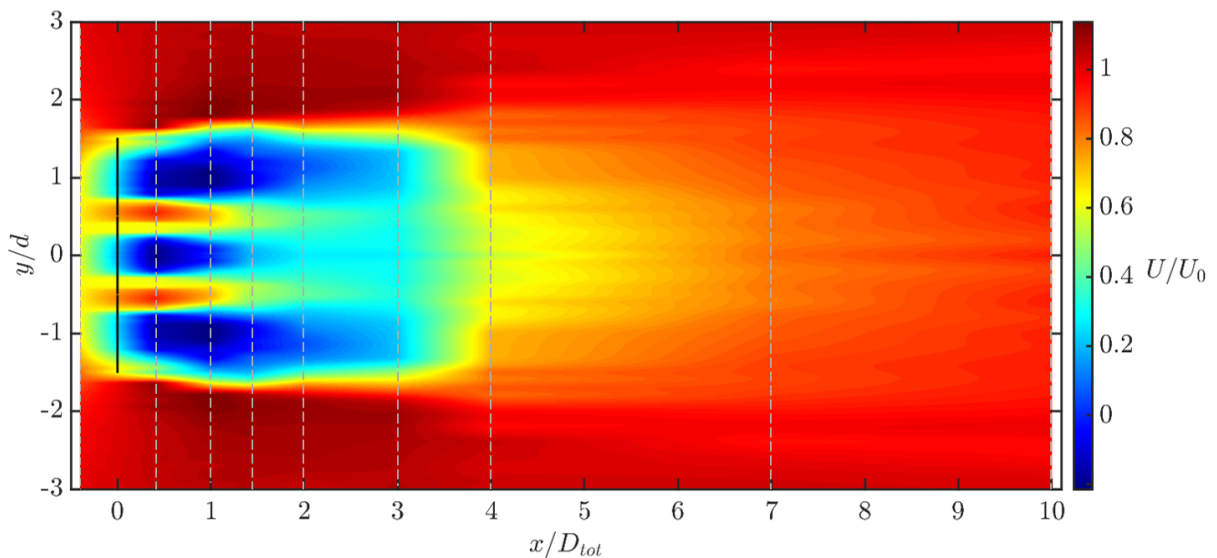
Figure 4.19: *Contour plot of normalized velocity in the wake of a MR7 with spacing 0.0d.*
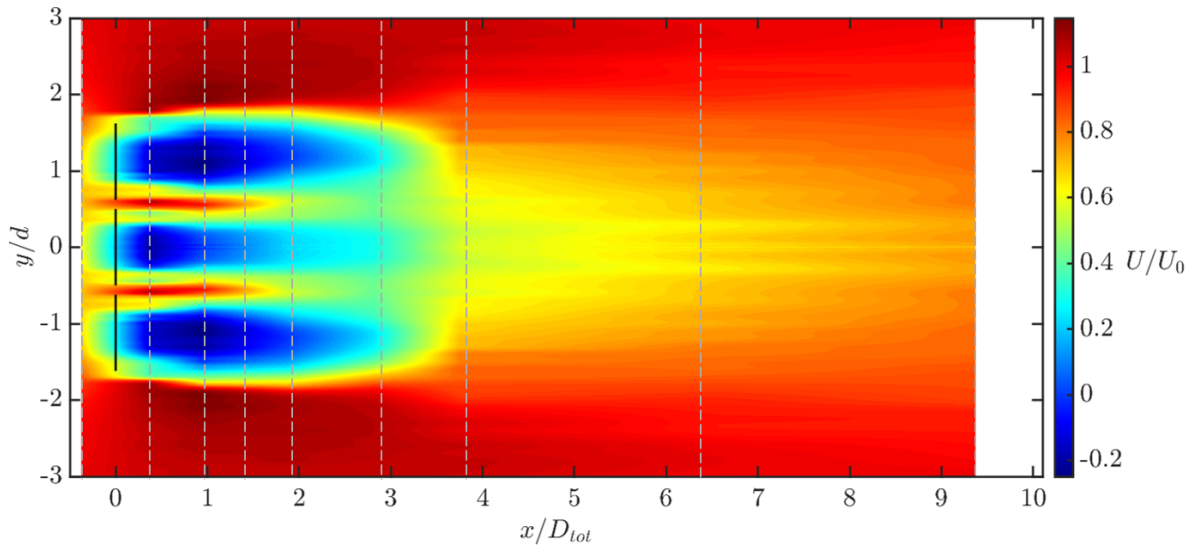
Figure 4.20: *Contour plot of normalized velocity in the wake of a MR7 with spacing 0.1d.*
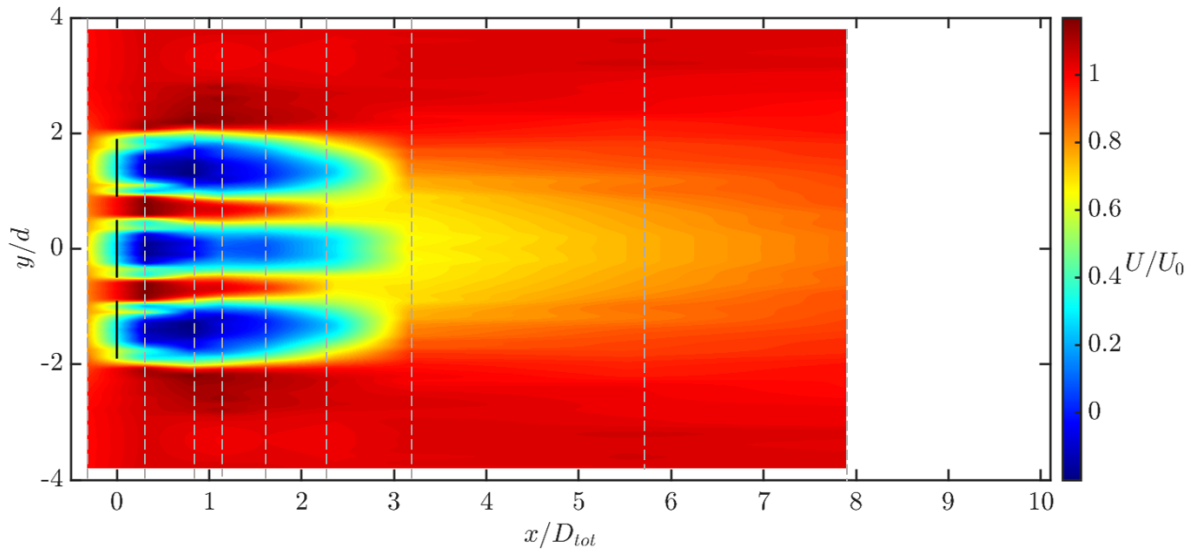
Figure 4.21: *Contour plot of normalized velocity in the wake of a MR7 with spacing 0.4d.*

An increase in disc spacing gives a lower velocity deficit and lower turbulence in the near wake. This initial low velocity deficit leads to a faster recovery, at least with the largest spacing, but the $0.1d$ showed a slower wake recovery than $0.0d$. Low turbulence in the flow and a fast wake recovery achieved with larger spacing is interesting as it is preferred with downstream turbines. However, a larger disc spacing has disadvantages as the total area taken up by the structure increases without increasing the swept area and without allegedly resulting in a power production increase. Thus, the choosing of disc spacing should be done in consideration when designing a wind farm to optimize the output of the combined wind farm.

4.2.4 Number of discs

The number of rotors in an MRS is a crucial parameter in the design and it is essential to investigate how an increase in the number of rotors affects wake development. Comparing the SR, MR4, MR7, and MR19, the velocity deficit in the near wake is not significantly affected by an increased number of rotors. All MRs show a significantly lower velocity deficit than the SR (see Figure 4.12). At $4D$, the velocity deficit is lower with a higher number of rotors, but this changes further downstream. At both $7D$ and $10D$, the SR and MR4 have a lower velocity deficit than the MR7 and MR19. A higher number of discs at these two downstream distances leads to a lower wake velocity. The recovery for a higher number of discs is therefore lower. As for the case of rotor spacing, the use of D to define the downstream distances is suspected to affect these results as well. To investigate the hypothesis centerline measurements for the normalized velocity deficit are presented in Figure 4.22 with a) the downstream distance dependent on D_{tot} and b) dependent on D. However, the difference in the 8-10 region on the x-axis for the two presentations is insignificant.
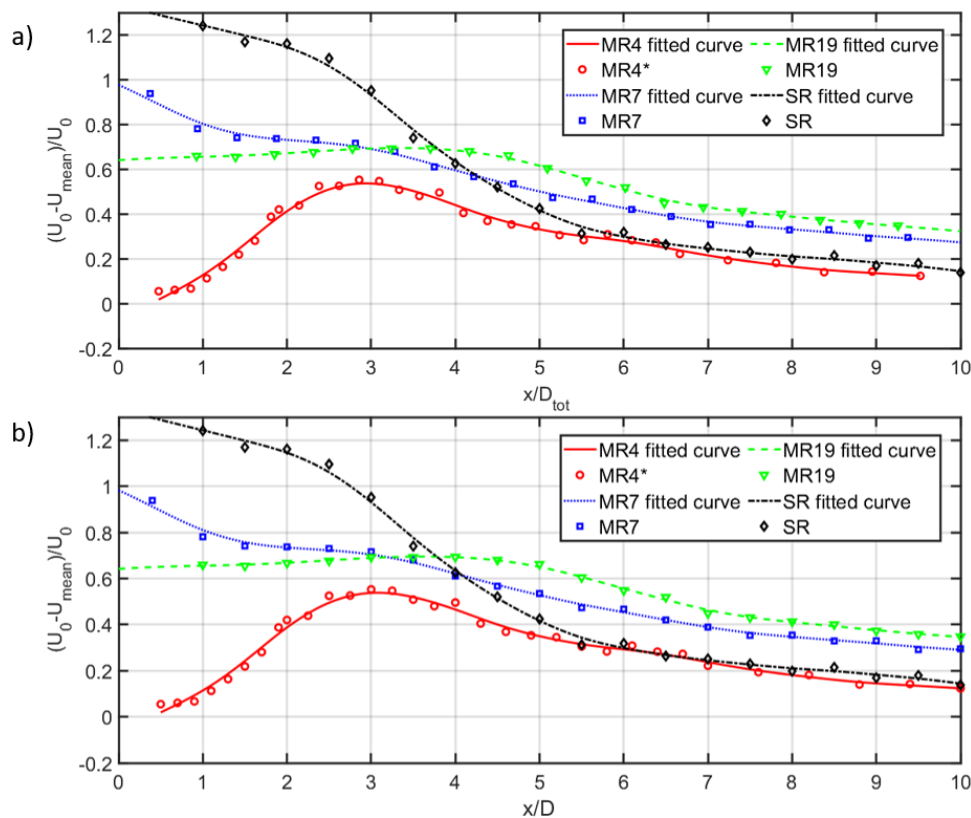
Figure 4.22: *Centerline measurements of the normalized velocity deficits of the SR, MR4, MR7, and MR19 with the x-axis dependent on a) x/D_{tot} and b) x/D.*

The lateral normalized tke profiles (see Figure 4.13) show that the SR and MR4 have signifi-

cantly higher tke levels than the MR7 and MR19. It is observed that a higher number of discs leads to lower turbulence at $2D$. The SR has the second-highest tke level and the MR4 the highest. The MR4 has been measured to the highest turbulence probably because the measurements are conducted in the space between the discs where the high-velocity jets induce high turbulence. At $4D$, the SR has the highest turbulence. The MR7 and MR19 continue to have the lowest turbulence level downstream, and at $10D$ all four setups have almost the same turbulence level.

As turbulence is an important reason for wake recovery, it can be argued that the lower wake turbulence generated by a higher number of discs makes the wake recover slowly. Even though the turbulence is similar at $10D$, the low initial turbulence seems to affect the whole wake downstream. In the space between the discs, smaller length-scale vortices, compared to the vortices created from the disc edge, are believed to be created, and for the increased number of discs, these eddies get relatively smaller.

One uncertainty is regarding using the 10 cm porous disc and whether it behaves similarly to the 20 cm disc. Øye [40] investigates the difference between the 20 cm and 70 cm porous disc and shows that these discs created similar relative wakes. Therefore, it is assumed that this would apply to the smaller 10 cm porous disc.

The defined wake widths (see Table 4.2) from the polynomial fitted curve show that the wake width of an MRS is narrower than an SR at all downstream distances. The number of rotors also seems to result in a lower wake expansion. However, the method for wake width definition might not be a suitable representation of this.

Bastankhah and Abkar [9] investigated the effect of a higher number of discs with LESs, comparing an SR, MR2, MR4, and MR7, with $0.1d$ disc spacing. The rotor-averaged velocity deficit converged to the same velocity around $10D$. The initial velocity deficit at $2D$ was found to reduce with an increased number of discs, confirming the findings from the measurements. At 5D, the MRs converged to the same velocity deficit while the SRs were still higher. Their lateral velocity deficit profiles showed that at $7D$ and $10D$ a higher number of discs led to a higher maximum velocity deficit, similarly to what was found in the measurements in the far wake.

Presented in Table 4.3 are the maximum normalized velocity deficits for the measurements from Table 4.2 and approximate values from the LES by Bastankhah and Abkar [9]. The results

are obtained with two completely different methods with different boundary conditions, and the experimental results were not meant to be used as a direct comparison. However, they could give insight into the overall patterns. At $X/D = 2$, the measurements and LES show that the SR's normalized velocity deficit is highest. The normalized velocity deficit reduces with an increasing number of rotors for the LES, while the measurements give a more similar velocity deficit for the different number of rotors. In the far wake, the two methods show the same pattern. The velocity deficit of the SR and MR4 are similar, while the velocity deficit of the MR7 and MR19 is the highest. At $x/D = 10$, the pattern is that a higher number of discs lead to a higher maximum normalized velocity deficit.

The statement that an MR wake recovers faster than an SR might not be completely accurate from the presented findings. The measurements suggest that initially, the MR wakes recover faster or at least have a lower velocity deficit with a higher number of discs. However, the wake recovery from $2D$ does not seem to improve with a higher number of discs, and the velocity deficit is higher with a higher number of discs at $7D$ and $10D$, which could be a disadvantage regarding downstream turbines. Regarding the turbulence in the wake, a higher number of rotors significantly reduced the initial turbulence, which is advantageous for downstream turbines as it reduces fatigue loads. However, the low turbulence is believed to cause the slow wake recovery. Furthermore, Bastankhah and Abkar [9] found that a higher number of rotors increased the power production, and Jameson et al. [8] stated that it would reduce the overall cost. Therefore, choosing the number of rotors should include the power production and cost for optimizing the MR turbine design and consider the wake effects in a wind farm situation.

Table 4.3: *Maximum normalized velocity deficit at the four downstream distances for the polynomial fitted measurement curves for laminar and turbulent flow and approximately maximum from the LES, and linear superposition, by Bastankhah and Abkar [9]. The linear superposition gave similar wakes as the LES for the other wakes, and is therefore also included.*

Disc con.fig.	Method	Max. normalized velocity deficit			
		X/D=2	X/D=4	X/D=7	X/D=10
SR	Polynomial fitted curve	1.14	0.64	0.26	0.12
	LES	0.65	0.55	0.30	0.20
MR4	Polynomial fitted curve	0.67	0.44	0.26	0.11
	LES	0.55	0.35	0.23	0.18
MR7	Polynomial fitted curve	0.70	0.44	0.32	0.25
	LES	0.46	0.39	0.30	0.21
MR19	Polynomial fitted curve	0.66	-	0.41	0.31
	Linear superposition	0.35	0.30	0.28	0.23

4.2.5   Wake steering

The wake measurement acquired for the yawed conditions indicates what can be expected by an MR. Firstly, yawing the individual discs or just the tower would deflect the wake similarly, at least in the measured near wake at the downstream distance $X = 2D$ (see Figure 4.15a). The maximum normalized velocity deficits between the two yaw configurations and the zero yaw configuration show no significant difference, and the yawed wakes are wider. For the normalized tke, the two yawed configurations result in different tke peak levels at different lateral locations (see Figure 4.16a). A difference between the two configurations is that the tower yaw moves the outer disc edges more away and closer on each side than the individual disc yaw. So between the velocity deficit and tke measurements, the turbulence is more evidently affected by this difference. Therefore, is the tke peak not occurring at the same location for the two configurations. The disc yaw creates a lower turbulence level at the side that the wake is deflected towards, while the opposite peak is higher. The tower yaw shows a turbulence peak closer to the wake center at the side the wake is deflected towards, and the opposite peak has a similar level. The tower yaw shows a similar turbulence level as the zero yaw, and the individual yaw has lower on one side and higher on the other.

With LES, Speakman et al. [27] investigated the wake behind an MR4 configuration with individual yaw of 30 degrees. The nearest wake cross-section presented was $X = 4D$. The LES showed a significant difference between the no yaw and individual yaw at $X = 4D$, where the former showed a maximum velocity deficit of ≈ 0.32 and the latter ≈ 0.22. The difference between these simulations and the measurements could be due to the different yaw angles, the number of discs, and downstream distance.

The third yaw configuration measured was the combined yaw. The combined yaw led to the discs being faced perpendicular to the flow with an offset between the discs' planes. The maximum normalized velocity deficit of the combined yaw is similar to the zero yaw (see Figure 4.15b), and the wake generated seems a bit wider but not deflected to either direction. For the normalized tke (see Figure 4.16b), the combined yaw creates two peaks located outside of the peaks of the zero yaw. Like the individual disc yaw, the combined yaw has one peak having a lower tke peak than the other.

A clear picture is hard to achieve with just one lateral wake profile of the yawed conditions. The lower normalized tke levels at one side for the individual disc yaw and combined yaw

are believed to be caused by the discs being closer to the measurement point than on the opposite side, resulting in lower turbulence. On the other hand, it could be caused by the angle the disc edge at each side is facing. For one side, the edge is sharply angled against the flow, or wake expansion direction, while the other side is angled with the flow's expansion direction. These angles might lead to different vortices being shed from the disc edges.

New possibilities for wake steering and altering the wakes' appearance could be something for MR turbines to take advantage of in wind farm situations [27]. An MR7 does not seem affected by the different yaw or angle of the incoming flow regarding the velocity deficit. The measurements do not indicate the effect the yaw configurations have on the turbine power. However, Speakman et al. [27] investigated the combined power output of two yawed MR4s aligned in the streamwise direction and concluded that in a wind farm situation, MR yaw configuration might lead to increased total power output for the combined wind farm.

4.2.6   Multirotor tower structure

For a potential commercialized MRS, the turbine structure will be an essential part with many challenges and unanswered questions. The design of the turbine structure is not a topic investigated in this thesis but is interesting. Essential factors in the design are structure design, yawing mechanism, rotor setup, and interaction between the structure's natural frequency and rotors. However, one aspect of an MR structure concerning the wake development has been explored with an additional support structure, added in the streamwise direction.

The results for the additional support structure (see Sec. 4.1.6) did not show any significant differences compared to one single frame. Only minor differences were present for the normalized velocity. The slight difference indicates that adding support structures in the streamwise direction should not significantly impact the wake development. The minor differences observed could be caused by random or systematic errors like the manual mounting, measurement distance, and the added support rods to the carriage for the WC7. The added support structure does not increase the blockage area on the flow as it is similar to the first frame structure. However, additional support in the plane area experienced by the flow could lead to more significant impacts on the downstream wake, increasing the blockage.

Chapter 5

Conclusion

In this thesis, several multirotor (*MR*) wakes induced by model scale porous discs have been experimentally measured in a towing tank. The effect of many MR design parameters has been explored with a particular focus on a setup of seven rotor discs (*MR7*).

Firstly, a turbulence grid's ability to generate a turbulent incoming flow for the MR setups was characterized. The results showed that at 2.0 meters downstream distance, the grid generated a turbulence intensity (*TI*) of 10.7 %. It was also observed that a high-velocity flow with low turbulence was present outside the grid area. Further downstream, a shear layer between the low turbulence and high turbulence flow was observed to mix the two flows.

Then, the difference in wake development between laminar and turbulent inflow for a single rotor (*SR*) and an MR7 was explored. For the MR wake, no significant difference was observed when exposed to different inflow conditions. However, the SR showed a lower normalized velocity deficit in the near wake with turbulent inflow, and in the far wake, both inflow conditions recovered to similar wake velocity. These results indicated that the rotor-added turbulence produced around the individual rotors in a MR setup dominates the incoming turbulence. This is not the case for SR, where the turbulence is mainly produced around the disc edges.

When comparing an SR wake with MR wakes, the MR wakes were shown to have a lower initial velocity deficit and lower turbulence level in the near wake. However, as the wake moves downstream, the SR wake recovers faster than the MR wakes and has a lower velocity deficit at $10D$ downstream.

Moreover, the effect of inter-rotor spacing on the wake was investigated. The three spacings of $s = 0.0d$, $0.1d$, and $0.4d$ were investigated. The definition of the downstream reference length with either D or D_{tot} was shown to have a significant impact when increasing the disc spacing, where $D = 3d$ and $D_{tot} = 3d + 2s$ for the MR7. For D, an increase in spacing led to a lower velocity deficit and a narrower wake in the near wake. At $4D$, the three wakes are already quite similar, and at $10D$, the largest disc spacing is showing the highest velocity deficit. When the wakes were compared with their relative downstream distance, D_{tot}, the results showed a different picture. The largest spacing led to a significantly faster wake recovery. In the far wake, it was more recovered than the two other wakes. For spacings of $0.0d$ and $0.1d$, the results show a slightly lower velocity deficit in the far wake for spacing of $0.0d$. The overall turbulence level was reduced with increased spacing.

Furthermore, the wake behind three MRs with a different number of discs, the MR4, MR7, and MR19, was compared. In general, the increase in the number of discs led to a lower velocity deficit and lower turbulence level in the near wake. However, the higher number of discs led to a higher velocity deficit in the far wake. This slow recovery was likely caused by the low initial turbulence and small vortices, which reduced the wake's ability to transport high-velocity flow into the wake. In contrast to that, larger turbulent vortices generated by an SR and MRs with fewer discs lead to a faster recovery. The higher velocity deficit in the far wake could potentially be a disadvantage for an increased number of rotors, and the low turbulence in the wake is an advantage.

Moreover, the near wake of an MR7 setup in different yaw configurations was investigated. The results indicated that the MR wakes were slightly altered in the different yaw configurations, but the maximum velocity deficit was similar for all cases. Additionally, the wake with an additional support structure was compared with a similar MR without the structure. The results did not show any significant effect on wake development.

Overall, the obtained results show interesting findings on the development of an MR wake and how the wake is affected by different design parameters. Multirotor system's wake can potentially have some advantages in tightly-spaced wind farm situations.

Chapter 6

Suggestions for Future Work

This thesis has investigated the wake effects for isolated multirotors, which leaves many unanswered questions regarding the MRs power production and the wake development in wind farm situations. More detailed investigations of the near and early far wake might give further insight to fully understand what wake effects are occurring and where they are located. In addition, using a particle image velocimetry could give a more detailed picture of the vortical structures present in the wake.

Prior studies have been done with an array of SR porous discs at MarinLab. Comparing these results with an array of MR units with varying spacing could be interesting to see if they behave differently than an array of SRs. However, there is a limit to the number of setups that can be investigated with physical investigations. Therefore, computational models are suggested to investigate the best MR design regarding power production and wake development for future work.

Eventually, how the turbine power is affected by different MR designs must be investigated on a model featuring rotating blades. This investigation could be done by using computational models based on the physical measurements obtained at MarinLab with the porous discs and obtaining data on energy production. For physical measurements, wind tunnel experiments are recommended over experiments in water due to the lower requirements required for the turbine equipment.

References

[1] IPCC, V. Masson-Delmotte, P. Zhai, A. Pirani, S. L. Connors, C. Péan, S. Berger, N. Chen, L. Goldfarb, M. I. Gomis, M. Huang, K. Leizell, E. Lonney, J. B. R. Matthews, T. K. Maycock, T. Waterfield, O. Yelekçi, R. Yu, and B Zhou. Summary for Policymakers. In: Climate Change 2021: The Physical Science Basis. Contribution of Working Group I to the Sixth Assessment Report of the Intergovernmental Panel on Climate Change [Internet]. Cambridge: Cambridge University Press; 2021 Jan [cited 2021 September]. Available from: `https://www.ipcc.ch/report/ar6/wg1/`.

[2] H. Ritchie, M. Roser, and P. Rosado. Co and greenhouse gas emissions. *Our World in Data*, 2020. https://ourworldindata.org/co2-and-other-greenhouse-gas-emissions.

[3] H. Ritchie, M. Roser, and P. Rosado. Energy. *Our World in Data*, 2020. https://ourworldindata.org/energy.

[4] A. Kahan and EIA. Eia projects nearly 50% increase in world energy usage by 2050, led by growth in asia, 2019. URL `https://www.eia.gov/todayinenergy/detail.php?id=41433`.

[5] IRENA. WIND ENERGY, 2020. URL `https://www.irena.org/wind`.

[6] IRENA. Future of wind: Deployment, investment, technology, grid integration and socio-economic aspects (A Global Energy Transformation paper). 2019.

[7] P. Jamieson, M. Branney, P. Chaviaropoulos, G. Sieros, S. Voutsinas, and P. Chasapogiannis. The Structural Design and Preliminary Aerodynamic Evaluation of a Multi-rotor System as a Solution for Offshore Systems of 20 MW or More Unit Capacity. *J. Phys. Conf. Ser.*, (1), 2014.

[8] P. Jamieson and M. Branney. Multi-Rotors; A Solution to 20 MW and Beyond? *Energy Procedia*, 24:52–59, 2012. doi: 10.1016/j.egypro.2012.06.086.

[9] M. Bastankhah and M. Abkar. Multirotor wind turbine wakes. *Phys. Fluids*, 31(8):085106, Aug 2019. doi: 10.1063/1.5097285.

[10] M. van der Laan and M. Abkar. Improved energy production of multi-rotor wind farms. *J. Phys. Conf. Ser.,* 1256(1), 2019. doi: 10.1088/1742-6596/1256/1/012011.

[11] M. P. van der Laan, S. J. Anderson, N. R. García, N. Angelou, G. R. Pirrung, S. Ott, M. Sjöholm, K. H. Sørensen, J. X. V. Neto, M. Kelly, T. K. Mikkelsen, and G. C. Larsen. Power curve and wake analyses of the Vestas multi-rotor demonstrator. *Wind Energy Sci. Discuss.*, (1932):1–30, 2019. doi: 10.5194/wes-2018-77.

[12] J. Bleeg, M. Purcell, R. Ruisi, and E. Traiger. Wind Farm Blockage and the Consequences of Neglecting Its Impact on Energy Production. *Energies*, 11(6):1609, jun 2018. doi: 10.3390/en11061609.

[13] N. Ghaisas, A. Ghate, and S. Lele. Large-eddy simulation study of multi-rotor wind turbines. *J. Phys. Conf. Ser.*, 1037(7):072021, jun 2018. doi: 10.1088/1742-6596/1037/7/072021.

[14] T. Nishino and R. Willden. The efficiency of an array of tidal turbines partially blocking a wide channel. *J. Fluid Mech.*, 708:596–606, Oct 2012. doi: 10.1017/jfm.2012.349.

[15] Wind catching. URL https://windcatching.com/.

[16] M. Hansen. *Aerodynamics of Wind Turbines.* Routledge, third edition, May 2015. doi: 10.4324/9781315769981.

[17] D. Zhao, N. Han, C. Goh, and J. Reinecke. *Wind Turbines and Aerodynamics Energy Harvesters.* San Diego: Elsevier Science & Technology, 2019.

[18] L. Vermeer, J. Sørensen, and A. Crespo. Wind turbine wake aerodynamics. *Prog. Aerosp. Sci.*, 39(6-7):467–510, aug 2003. doi: 10.1016/S0376-0421(03)00078-2.

[19] F. Porté-Agel, M. Bastankhah, and S. Shamsoddin. Wind-turbine and wind-farm flows: A review. *Boundary-layer meteorology*, 174(1):1—59, 2020. doi: 10.1007/

s10546-019-00473-0.

[20] B. Sanderse. Aerodynamics of wind turbine wakes-literature review. 2009.

[21] S. Helvig, M. Vinnes, A. Segalini, N. Worth, and J. Hearst. A comparison of lab-scale free rotating wind turbines and actuator disks. *J. Wind Eng. Ind. Aerodyn.*, 209:104485, feb 2021. doi: 10.1016/j.jweia.2020.104485.

[22] S. Pookpunt and W. Ongsakul. Optimal placement of wind turbines within wind farm using binary particle swarm optimization with time-varying acceleration coefficients. *Renew. Energy*, 55:266–276, jul 2013. doi: 10.1016/j.renene.2012.12.005.

[23] J. P. Bentley. *Principles of measurement systems.* Pearson, 4th edition, 2005.

[24] C. Garrett and P. Cummins. The efficiency of a turbine in a tidal channel. *J. Fluid Mech.*, 588:243–251, oct 2007. doi: 10.1017/S0022112007007781.

[25] J. R. Bjørnsen. Lab-scale measurements of blockage and wake flow on a setup of three laterally spaced wind turbine rotors. Master's thesis, University of Bergen, 2021.

[26] M. Howland, S. Lele, and J. Dabiri. Wind farm power optimization through wake steering. *Proc. Natl. Acad. Sci.*, 116(29):14495–14500, jul 2019. doi: 10.1073/pnas.1903680116.

[27] G. Speakman, M. Abkar, L. Martínez-Tossas, and M. Bastankhah. Wake steering of multirotor wind turbines. *Wind Energy*, (June 2020):we.2633, mar 2021. doi: 10.1002/we. 2633.

[28] Á. Jiménez, A. Crespo, and E. Migoya. Application of a LES technique to characterize the wake deflection of a wind turbine in yaw. *Wind Energy*, 13(6):559–572, dec 2009. doi: 10.1002/we.380.

[29] S. Steen. Lecture notes in Experimental Methods in Marine Hydrodynamics, 2014.

[30] A. Pique, M. A. Miller, and M. Hultmark. Characterization of the wake behind a horizontal-axis wind turbine (HAWT) at very high Reynolds numbers. *J. Phys. Conf. Ser.*, 1618(6): 062039, sep 2020. doi: 10.1088/1742-6596/1618/6/062039.

[31] C. Leikvoll, M. Hansen, and A. Rogne. Drag measurements on a multirotor disc setup.

B.S. Thesis, Western Norway University of Applied Sciences, 2021.

[32] R. L. Panton. *Incompressible Flow*. Wiley, 4th edition, 2013.

[33] J. Bartl. *Experimental testing of wind turbine wake control*. PhD thesis, NTNU, 2018.

[34] V. L. Okulov, R. F. Mikkelsen, I. V. Naumov, I. V. Litvinov, E. Gesheva, and J. N. Sørensen. Comparison of the far wake behind dual rotor and dual disk configurations. *J. Phys. Conf. Ser.*, 753(3):032060, sep 2016. doi: 10.1088/1742-6596/753/3/032060.

[35] V. L. Okulov, R. Mikkelsen, J. N. Sørensen, I. V. Naumov, and M. A. Tsoy. Power Properties of Two Interacting Wind Turbine Rotors. *J. Energy Resour. Technol.*, 139(5):1–6, sep 2017. doi: 10.1115/1.4036250.

[36] C. Kress, N. Chokani, and R.S. Abhari. Passive minimization of load fluctuations on downwind turbines. *Renew. Energy*, 89:543–551, apr 2016. doi: 10.1016/j.renene.2015.12. 009.

[37] R. Garnes, J. Jensen, and A. Rogne. *Upstream Blockage and Downstream Wake Flow of a Wind Turbine*. Bsc, Western Norway University of Applied Sciences, 2020.

[38] NORTEK. "Vectrino 3D water velocity sensor Lab Probe", 1, 2017.

[39] J. Bartl, C. H. Aasnæs, J. R. Bjørnsen, G. Stenfelt, and D. R. Lande-Sudall. Lab-scale measurements of wind farm blockage effects. *accepted for publication i Journal of Physics: Conference Series*, 2022.

[40] S. Øye. Experimental Study of the Wake Flow and Thrust Coefficient of Porous Actuator Discs. Master's thesis, University of Bergen, Submitted June, 2022.

[41] A. G. Jørs and T. L. Mjåtveit. Wake flow lab measurements of multi-rotor wind turbines. B.S. Thesis, Western Norway University of Applied Sciences, 2021.

[42] I. Koi. Aerodynamic interaction effects on multi-rotor wind turbines. Master's thesis, University of Bergen, Submitted June, 2022.

[43] T. K. Løken, D. R. Lande-Sudall, A. Jensen, and J. Rabault. Grid turbulence measurements with an acoustic doppler current profiler. 2021. Preprint available at:. doi: 10.48550/

ARXIV.2111.10273.

[44] C. H. Aasnæs. Experimental investigation of wind farm flow effects . Master's thesis, University of Bergen, 2022.